Report No. KS-24-02 ▪ FINAL REPORT ▪ March 2024

Investigation of High Mast Illumination Pole Handhole Cracking

Tristan Yount
Danqing Yu
Caroline Bennett, Ph.D., P.E.
William Collins, Ph.D., P.E.
Jian Li, Ph.D., P.E.

The University of Kansas

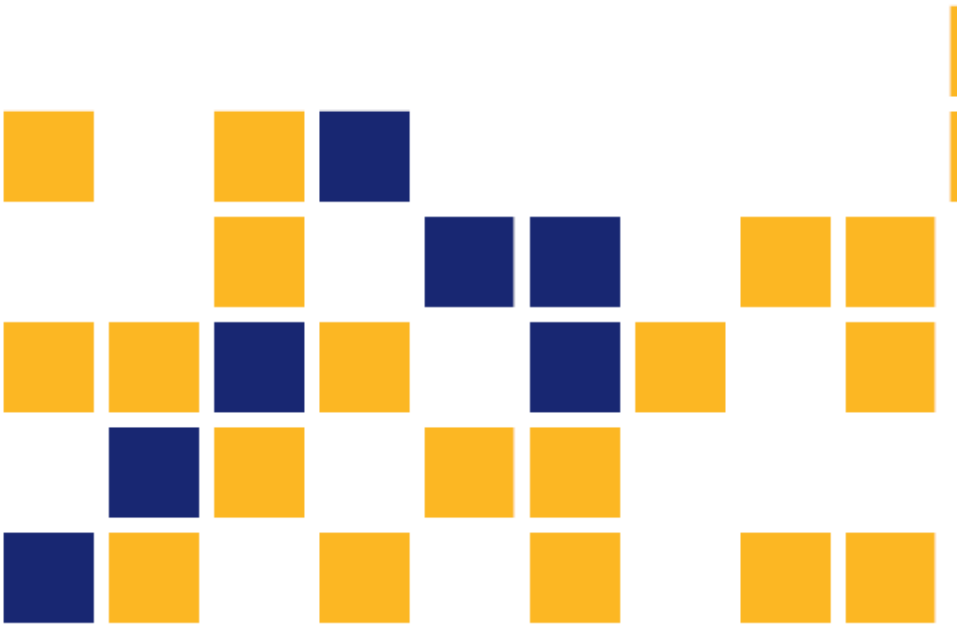

Kansas
Department of Transportation

1 Report No. KS-24-02	**2 Government Accession No.**	**3 Recipient Catalog No.**
4 Title and Subtitle Investigation of High Mast Illumination Pole Handhole Cracking		**5 Report Date** March 2024 **6 Performing Organization Code**
7 Author(s) Tristan Yount; Danqing Yu; Caroline Bennett, Ph.D., P.E.; William Collins, Ph.D., P.E.; Jian Li, Ph.D., P.E.		**8 Performing Organization Report No.**
9 Performing Organization Name and Address The University of Kansas Department of Civil, Environmental & Architectural Engineering 1530 West 15th St Lawrence, Kansas 66045-7609		**10 Work Unit No. (TRAIS)** **11 Contract or Grant No.** C2139
12 Sponsoring Agency Name and Address Kansas Department of Transportation Bureau of Research 2300 SW Van Buren Topeka, Kansas 66611-1195		**13 Type of Report and Period Covered** Final Report March 2019 – December 2020 **14 Sponsoring Agency Code** RE-0781-01
15 Supplementary Notes For more information write to address in block 9.		

16 Abstract

High mast illumination poles (HMIPs) experience cyclic loading from wind, which can cause large deflections at the top of the pole, amplified by the mass and geometry of the luminaire. As a result, large stresses can develop at the handhole and base plate connections. These details are especially susceptible to fatigue cracking due to the combination of welding, galvanizing, and geometry causing stress concentrations at the welds. After a "bomb cyclone" winter storm impacted the state of Kansas in February 2019, multiple HMIPs that had been recently erected were identified to have visible or potential cracking and subsequently removed from service.

Based on this experience, the University of Kansas (KU) worked with the Kansas Department of Transportation (KDOT) to explore the potential cause of the premature failures, and to provide input on design modifications to prevent future HMIPs from failing well before their expected lifespan.

This report describes an investigation in which four poles removed from service were studied to determine potential origins and driving factors of the handhole cracking. Each pole was cut and processed so that the crack surfaces could be examined. Sub-sized Charpy V-Notch (CVN) specimens were sampled from each pole and tested to estimate the toughness of base metal used.

Additionally, the effects of varying the design parameters of the pole, handhole, and base plate were explored in a parametric study using finite element modeling. The computational work performed included: varying pole, hand hole, and base plate geometries; performing a comparison between the original reinforcing rim handhole detail and a proposed doubler plate handhole detail; and an analysis of a new HMIP design proposed by KDOT. The finite element analyses were performed using both design-level fatigue loading and a loading estimated from the large-amplitude first mode displacement shown in the video during the "bomb cyclone" weather event.

Major findings from the study include: 1) the partial penetration weld connecting the reinforcing rim and the pole displayed a lack of fusion at the weld root that reduced the effective strength of the weld; 2) cracking around the handhole weld did not show clear fatigue growth, but the cracks that grew horizontally into the pole were due to fatigue; 3) use of a thicker pole, a thicker reinforcing rim, a narrower handhole, and full penetration welding can be expected to reduce the structural hot-spot stress at the handhole detail; and 4) use of a thicker pole, a thicker base plate, a thinner reinforcing rim, and a smaller base plate hole can be expected to reduce the structural hot-spot stress at the base plate detail.

17 Key Words High Mast Lighting, Fatigue Cracking, Repeated Loads, Service Life		**18 Distribution Statement** No restrictions. This document is available to the public through the National Technical Information Service www.ntis.gov.	
19 Security Classification (of this report) Unclassified	**20 Security Classification (of this page)** Unclassified	**21 No. of pages** 105	**22 Price**

Form DOT F 1700.7 (8-72)

This page intentionally left blank.

Investigation of High Mast Illumination Pole Handhole Cracking

Final Report

Prepared by

Tristan Yount
Danqing Yu
Caroline Bennett, Ph.D., P.E.
William Collins, Ph.D., P.E.
Jian Li, Ph.D., P.E.

The University of Kansas

A Report on Research Sponsored by

THE KANSAS DEPARTMENT OF TRANSPORTATION
TOPEKA, KANSAS

and

THE UNIVERSITY OF KANSAS
LAWRENCE, KANSAS

March 2024

NOTICE

The authors and the state of Kansas do not endorse products or manufacturers. Trade and manufacturers names appear herein solely because they are considered essential to the object of this report.

This information is available in alternative accessible formats. To obtain an alternative format, contact the Office of Public Affairs, Kansas Department of Transportation, 700 SW Harrison, 2nd Floor – West Wing, Topeka, Kansas 66603-3745 or phone (785) 296-3585 (Voice) (TDD).

DISCLAIMER

The contents of this report reflect the views of the authors who are responsible for the facts and accuracy of the data presented herein. The contents do not necessarily reflect the views or the policies of the state of Kansas. This report does not constitute a standard, specification or regulation.

Abstract

High mast illumination poles (HMIPs) experience cyclic loading from wind, which can cause large deflections at the top of the pole, amplified by the mass and geometry of the luminaire. As a result, large stresses can develop at the handhole and base plate connections. These details are especially susceptible to fatigue cracking due to the combination of welding, galvanizing, and geometry causing stress concentrations at the welds. After a "bomb cyclone" winter storm impacted the state of Kansas in February 2019, multiple HMIPs that had been recently erected were identified to have visible or potential cracking and subsequently removed from service.

Based on this experience, the University of Kansas (KU) worked with the Kansas Department of Transportation (KDOT) to explore the potential cause of the premature failures, and to provide input on design modifications to prevent future HMIPs from failing well before their expected lifespan.

This report describes an investigation in which four poles removed from service were studied to determine potential origins and driving factors of the handhole cracking. Each pole was cut and processed so that the crack surfaces could be examined. Sub-sized Charpy V-Notch (CVN) specimens were sampled from each pole and tested to estimate the toughness of base metal used.

Additionally, the effects of varying the design parameters of the pole, handhole, and base plate were explored in a parametric study using finite element modeling. The computational work performed included: varying pole, hand hole, and base plate geometries; performing a comparison between the original reinforcing rim handhole detail and a proposed doubler plate handhole detail; and an analysis of a new HMIP design proposed by KDOT. The finite element analyses were performed using both design-level fatigue loading and a loading estimated from the large-amplitude first mode displacement shown in the video during the "bomb cyclone" weather event.

Major findings from the study include: 1) the partial penetration weld connecting the reinforcing rim and the pole displayed a lack of fusion at the weld root that reduced the effective strength of the weld; 2) cracking around the handhole weld did not show clear fatigue growth, but the cracks that grew horizontally into the pole were due to fatigue; 3) use of a thicker pole, a thicker reinforcing rim, a narrower handhole, and full penetration welding can be expected to reduce the structural hot-spot stress at the handhole detail; and 4) use of a thicker pole, a thicker base plate, a thinner reinforcing rim, and a smaller base plate hole can be expected to reduce the structural hot-spot stress at the base plate detail.

Acknowledgements

The authors of this paper would like to gratefully acknowledge the Kansas DOT for their support of the work performed in this project. Mr. Kent Dye's and Mr. David Woody's generous help in the laboratory is also greatly appreciated.

Table of Contents

List of Tables

List of Figures

Chapter 1: Introduction and Background

1.1 Background

High mast illumination poles (HMIPs) are tall pole structures (at least 55 ft or taller) with luminaires attached to the top. They are widely used near highway interchanges to provide lighting for passing traffic and to improve safety. HMIPs are commonly made of steel components that are galvanized after fabrication. These structures have generally performed well in service; however, there have been numerous instances of HMIPs developing fatigue cracking at details near the base of the structure. Additionally, the flexibility of the structures has corresponded with development of locked-in resonant behavior that remains poorly understood, but that clearly results in high-amplitude displacements that can produce enormous stresses and strains near the base of the pole.

The primary loading acting on HMIP structures is due to wind; however, there is some disagreement as to their susceptibility to vortex shedding. Some researchers have suggested that HMIP structures are susceptible to vortex shedding (Connor et al., 2012), while others have upheld that because of the tapered pole design, vortex shedding is not a major concern (Foley et al., 2004). The American Association of State Highway and Transportation Officials (AASHTO) Standard Specifications for Structural Supports for Highway Signs, Luminaires, and Traffic Signals (the 'LTS Specification', AASHTO, 2013) provisions for HMIPs indicates that vortex shedding can lead to rapid accumulation of potential damage and as such is considered in the combined wind pressure for fatigue design.

The most fatigue-critical details in HMIP structures are considered to be the welded details at the handhole and base plate (BP). The handhole is an opening in the pole a few feet above the ground that allows access to the interior of the pole, primarily used for access to the raising and lowering mechanism for the luminaires. Foley et al. (2004) described the collapse of an HMIP due to loose anchor rod nuts. Connor et al. (2012) reported that cracking is generally found at the welded base plate-to-pole connection, the welded handhole connection, and in anchor rods, with the latter less prevalent than cracking at the two welded details.

Several other studies have indicated that the galvanizing process may contribute to cracking at welds in lighting, traffic, and sign structures (Kleineck, 2011; Ocel, 2014; Pool, 2010). Goyal et al. (2012) described internal toe cracking detected in some poles after galvanizing, and

Foley et al. (2004) discussed the failure of a bridge-type overhead sign structure, indicating that cracking was caused by liquid metal embrittlement during galvanizing. Bennett et al. (2021) studied this phenomenon in detail, conducting physical tests and computational simulations to assess the relative susceptibility of welded highway structures to cracking during galvanizing. They concluded that a number of material, fabrication, and galvanizing factors can interact to compound susceptibility to liquid embrittlement during galvanizing—including the presence of heat affected zones and stress concentrations. Nasouri et al. (2019a, 2019b) performed nonlinear coupled thermo-mechanical simulations to assess demands on HMIP structures during galvanizing. They concluded that the interactive effects between stress concentrations at the bends of multisided poles and differential thermal loading at the junction of the thick base plate and thinner pole played major roles in the susceptibility of HMIPs to cracking during galvanizing. Bennett et al. (2021) and Nasouri et al. (2019a, 2019b) concluded that it is important to minimize thickness mismatches between the pole and base plate, and to reduce the severity of stress concentrations at welded details, to reduce the likelihood of cracking during galvanizing.

Roy et al. (2011) performed multiple experimental tests and analytical studies on cantilevered sign/signals and HMIPs under NCHRP Project 10-70. A lack of fusion at the root of the handhole weld was found to be the cause of all handhole cracks observed during experimental testing. Due to limited access at the pole interior, the handhole detail has an increased likelihood for undetected lack of fusion at the weld root. However, no fatigue cracking was observed at the toe of the handhole reinforcing fillet welds during experimental tests. Because of this, Roy et al. concluded that the base plate detail was the most fatigue critical detail for cantilevered sign/signals and HMIPs.

The handhole detail used in Kansas Department of Transportation (KDOT) HMIPs consists of a rectangular opening with rounded corners and a 1-in.-thick reinforcing rim. The reinforcing rim and the pole are connected using a partial penetration weld with a reinforcing fillet weld. Handholes are a necessary feature of HMIPs to allow access to the electric controls near the base of the pole, and to enable access to the raising and lowering mechanisms for the light fixtures. As such, some stress concentrations from the fabrication and geometry at the handhole are unavoidable and must simply be mitigated as much as possible.

The base plate to pole (BP-Pole) connection utilizes a full penetration weld with a reinforcing fillet weld. A backing ring is welded at the inside of the pole and to the base plate (BP) to accommodate the full penetration weld at the BP-Pole connection. KDOT HMIP structures typically range from 80 to 120 ft tall, and are made of steel, galvanized in fabricated condition. The details of the handhole and base plate connections are shown in Figure 1.1.

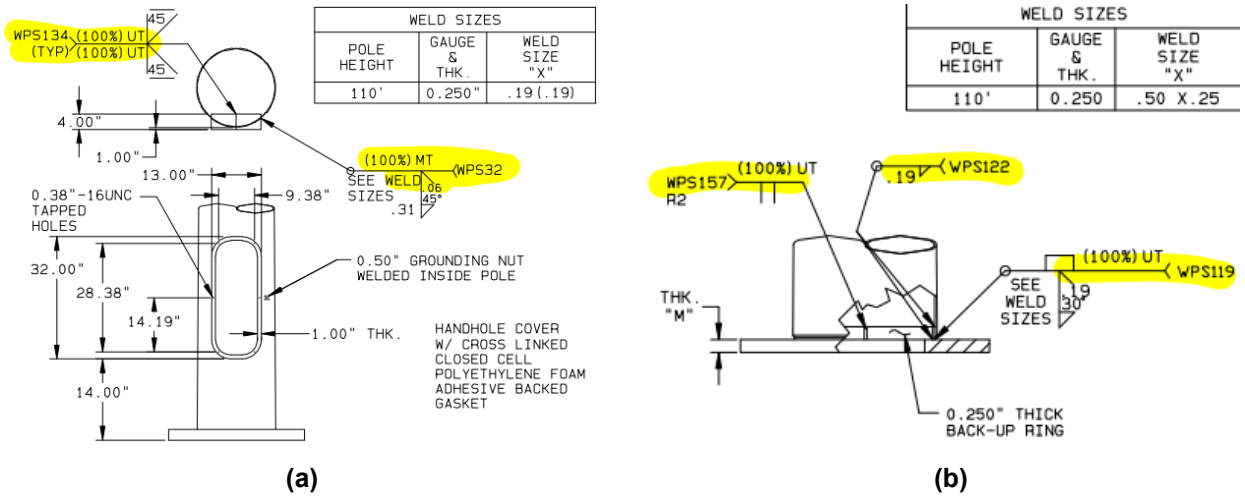

Figure 1.1: Details for KDOT HMIP pre-2019 Designs: (a) Handhole and (b) Base plate Connections

Although HMIPs are designed to resist wind-induced fatigue loading according to the AASHTO (2013) LTS Specification, KDOT recently discovered significant cracking at the handhole and base plate details of the poles after a severe winter storm, as shown in Figure 1.2. Many of the cracked poles had been very recently installed (within a year) and designed according to current specifications. The development of cracks, particularly in such a short period of time, was cause for significant concern since a pole failure would significantly endanger the safety of motorists and potentially cause substantial damage to infrastructure.

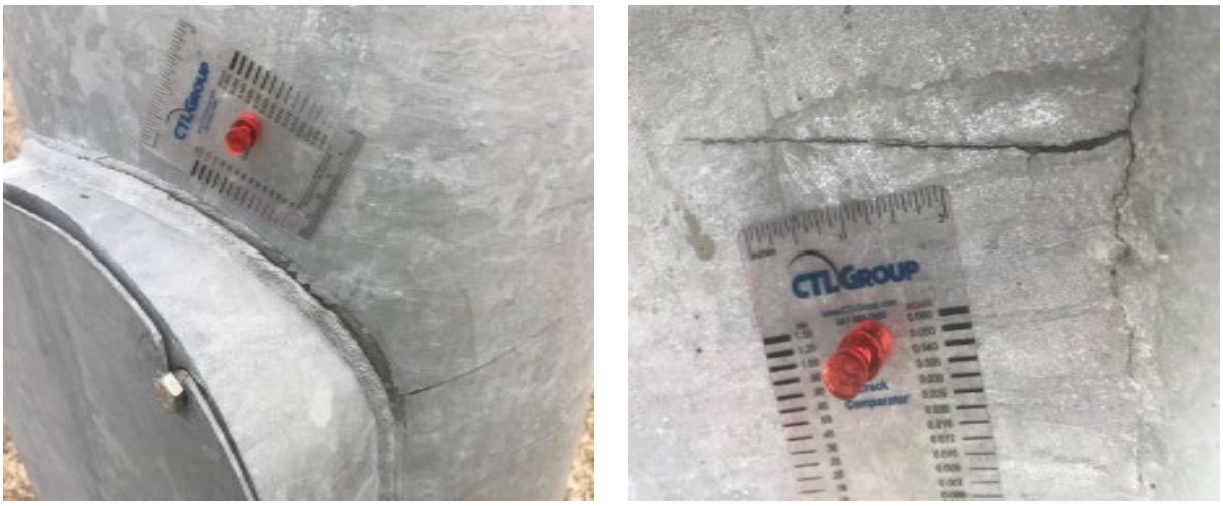

(a) (b)

Figure 1.2: Cracking (a) At the Handhole Weld, and (b) Growing into the Pole Base Metal

Videos recorded of HMIPs during the 2019 weather event indicated that the pole tips underwent very large-amplitude locked-in displacements in what appeared to be a first-mode response. Wind speeds were in the range of 30 mph during the weather event, which is not an unusual occurrence in Kansas. While KDOT immediately acted to remove and replace the cracked poles, research was needed to provide information for a better solution in future designs. It should be noted that, while Connor et al. (2012) described a similar event in which the pole was undergoing large-amplitude oscillations in first-mode as extremely rare, exceeding 1:10,000 probability, recent events have cast some doubt regarding the rarity of such occurrences.

1.2 Problem Statement

Multiple Kansas DOT HMIPs exhibited issues with cracking around the handhole weld after a winter weather event in February 2019. The cracking at the handhole connections resulted in the HMIPs being taken out of service long before their anticipated service life had been reached; had the failures gone undetected, they would have posed a serious threat to the public.

Several factors have the potential to increase or decrease the amount of stress that is concentrated at the handhole weld detail:

1. The geometry of the handhole (i.e., height, width, aspect ratio, and corner radius),

2. The thicknesses of the reinforcing rim and the pole, and
3. The welding procedures.

Galvanizing procedures may also influence the susceptibility of the welded detail to cracking. It is possible that relatively minor changes to the HMIP design could greatly improve the performance of the handhole connection.

1.3 Research Objectives

The aim of the research presented in this report was to determine the causes of handhole cracking in KDOT HMIPs, and to generate an understanding of the relative importance of various HMIP design parameters in terms of fatigue susceptibility. The scope of this project included both a physical forensic investigation and analytical modeling, specifically:

- ***Crack surface investigation*** – to extract information on the origin and propagation of the cracks and to allow for cross-sections of the welds to be inspected.
- ***Material testing*** – to consider the estimated toughness of the pole material.
- ***Parametric study*** – to identify factors with the largest impact on stresses at the handhole weld, to allow those factors to be controlled in future designs for improved performance.
- ***Performance evaluation*** – to quantify the lifespan of the prototype HMIP design in both design-level fatigue and observed "bomb cyclone" conditions.

Utilizing these methods, conclusions were drawn regarding the causes of the handhole cracking and recommendations were made to mitigate cracking in future HMIP designs.

1.4 Report Organization

Section 1.5 presents a literature review of pertinent studies and findings on current problems affecting HMIPs, and, also, provides background information on the basis of the methodology used in this research. Chapter 2 describes the research methodology, including forensic investigation methods and analytical modeling techniques. Chapter 3 outlines the results

of both the physical forensic investigation and analytical modeling. Chapter 4 summarizes the results, formulates conclusions, and provides recommendations for future work on the fatigue performance of HMIPs. The Appendix provides construction documentation and supporting information obtained from the forensic investigation and analytical modeling.

1.5 Literature Review

This section serves as background and context regarding performance problems that have been identified with HMIPs and outlines topics used as the foundation of the work summarized in Chapter 2.

1.5.1 Fatigue

Fatigue is the progressive deterioration of a material over time due to cyclical loading (Dowling, 1999). Typically, fatigue results in the formation of cracks at stress concentrations and can limit the service life of a structure. These cracks are more likely to form at connection features, such as welds, and drilled or punched holes. Both processes impart microscopic cracks into the material from rapid heating and cooling, scratching during machining, and material yielding. These microscopic cracks act as initiation sites for fatigue cracks. The combination of microscopic cracking and stress concentrations from geometric discontinuities makes fatigue a common issue for metallic structure connections.

The American Association of State Highway and Transportation Officials (AASHTO) LRFD Bridge Design Specification 8th Edition (AASHTO, 2017) provides guidance for fatigue design of welded and bolted connections. The cyclical stress range *S*, number of anticipated cycles *N*, and detail categories from A to E' are used in engineering designs of structures to estimate the fatigue life of the connection. This is done using S-N curves in which fatigue life increases with a decreasing stress range. Each detail is categorized based on empirical testing, with Category A having the best performance and Category E' having the worst performance. Horizontal lines indicate infinite fatigue life for stress ranges below horizontal line. Figure 1.3 shows the AASHTO S-N curves for all detail categories (AASHTO, 2017).

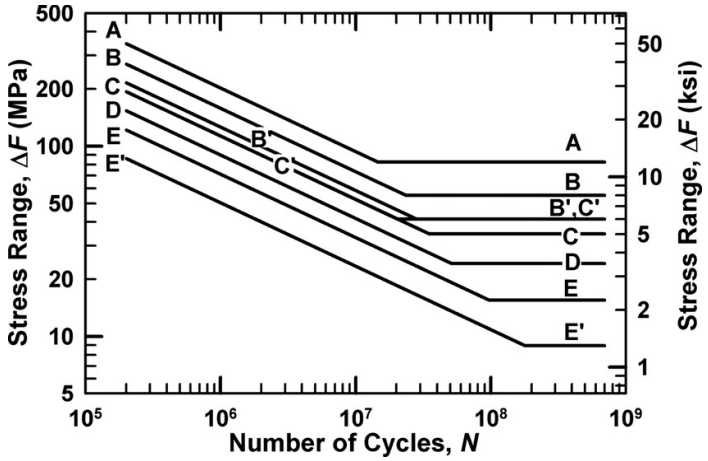

Figure 1.3: AASHTO S-N Curves for All Design Categories (AASHTO, 2017)

The AASHTO LTS Specifications (AASHTO, 2013) also provide detailed guidance regarding fatigue design for lighting, traffic, and sign structures. HMIPs are required to be designed for infinite fatigue life, due to the unpredictable nature of wind loading.

1.5.2 Galvanizing

1.5.2.1 Welding and Hot-Dip Galvanizing

Galvanizing is the process of coating steel structures with a protective zinc barrier to improve corrosion resistance. Welding can be performed before or after hot-dip galvanizing, but it is typically done before to avoid the release of toxic zinc fumes during welding. To ensure that the galvanized coating covers welds evenly, three important issues are considered:

1. Chemical makeup of the weld metal,
2. Cleanliness of the weld area, and
3. Continuity of a seal weld (American Galvanizers Association, 2009).

Regarding chemical makeup, higher silicon content accelerates the rate of galvanizing growth, leading to a thicker layer of zinc that increases the possibility of damage to the coating. Chemical cleaning agents used before hot dipping do not remove slag or flux. The zinc coating cannot adhere to these areas and, if they are not removed mechanically, will result in a bare spot in the coating, shown in Figure 1.4(a). Lastly, the viscosity of molten zinc prevents it from entering

any space with an opening smaller than 3/32 in. Cleaning solutions have a lower viscosity and can be retained in the tight spaces, leaving salts behind that can later cause iron-oxide weeping. If the weld has small discontinuities, these areas can be left uncoated and weep rust over the covered areas, shown in Figure 1.4(b).

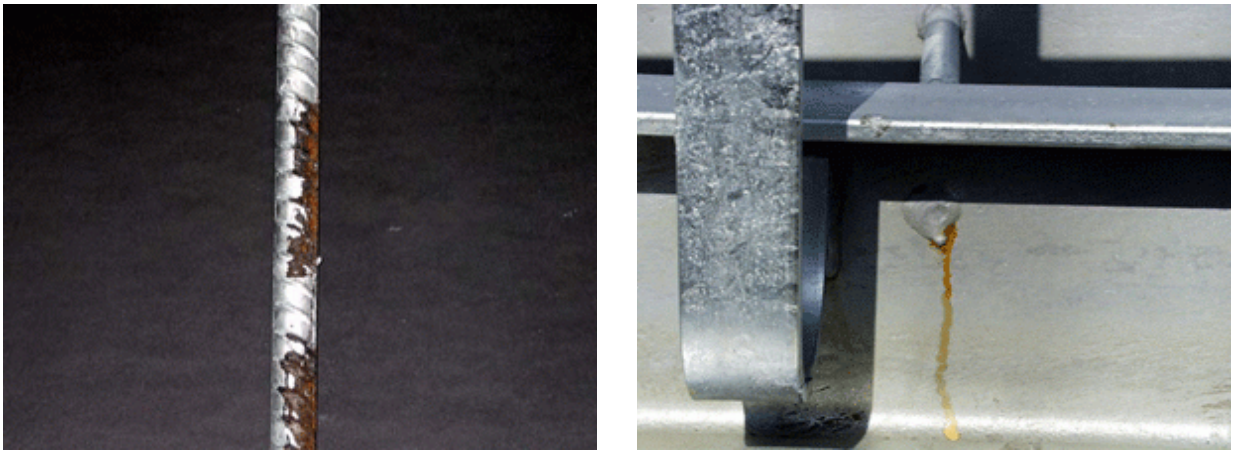

(a) (b)

Figure 1.4: Galvanizing (a) Bare Spots and (b) Weld Weeping (American Galvanizers Association, 2009)

Aside from weld preparation, certain design considerations are important when hot-dipped galvanizing is to be used. One such recommendation is to use equal or nearly equal thickness of assembly pieces. Thinner components will expand and cool more rapidly than thicker components. This differential cooling rate can produce high levels of thermal stress at the weld, and in extreme cases, cause distortion or rupture of the weld.

1.5.3 Structural Hot-Spot Stress Analysis Using Finite Element Analysis

Structural hot-spot stress (HSS) analysis is a method that can be used to evaluate fatigue performance of welded details, explicitly accounting for local geometric effects. The structural hot-spot stress is a computed stress at the location of anticipated crack initiation. The HSS includes the effect of stress concentration caused by local geometries but does not include nonlinear effects produced by the weld notch. The latter is considered implicitly in the experimentally determined fatigue resistance curve (S-N curve) used in tandem with the computed stress.

There are multiple formulations for hot-spot stress, and a wide range of specifications have developed different methodologies—although they are generally similar in approach. For example, there is a different treatment for welded plate connections than for welded tubular connections. While the AASHTO LTS Specifications govern the design of HMIP structures in the U.S., because the AASHTO LTS is a relatively "young" fatigue specification, it remains useful to also consider other well-regarded specifications, such as DNV (2011) and the IIW (Niemi et al., 2018), as appropriate.

For welded plate connections, the structural hot-spot stress can be computed via linear extrapolation back to the weld toe using stresses extracted a short distance $0.4t$ or $1.0t$ away from the weld toe, where t is the thickness of the plate (Niemi et al., 2018). In welded tubular details, although a surface extrapolation method exists (DNV, 2011), a more commonly adopted method is to identify the stress at a distance of $0.1\sqrt{rt}$ away from weld toe (AASHTO, 2013; DNV, 2011), using the pipe radius, r, and pipe thickness, t. Stress can be measured experimentally or computed from finite element models.

The AASHTO LTS Specification (AASHTO, 2013) requires the maximum (tensile) principal stress to be used as the structural hot-spot stress. The IIW specifications (Niemi et al., 2018) provide a more complicated definition, defining the hot-spot stress to be:

1. The larger principal stress if its direction is within 60° of the normal direction of the weld toe;
2. If the larger principal stress is outside this angle, the structural HSS should be the larger of the stress normal to the weld toe or the minimum principal stress.

Based on the definition provided in Niemi et al., it would be conservative to use the larger principal stress unless a more detailed analysis is necessary.

Regarding the fatigue resistance curve that the structural hot-spot stress is to be compared with, IIW-based fatigue design (Hobbacher, 2008) is used in conjunction with its FAT 90 curve, AASHTO (2013) HSS-based fatigue design is used with its Category C-curve, and DNV (2011) requires the use of its Category D-curve for HSS analysis. It is important to note that the DNV D-curve, IIW FAT 90 (for high cycle application), and AASHTO C-curve are the same curve in the

finite life region, but they have differences in the high cycle region. The three curves are plotted together in Figure 1.5.

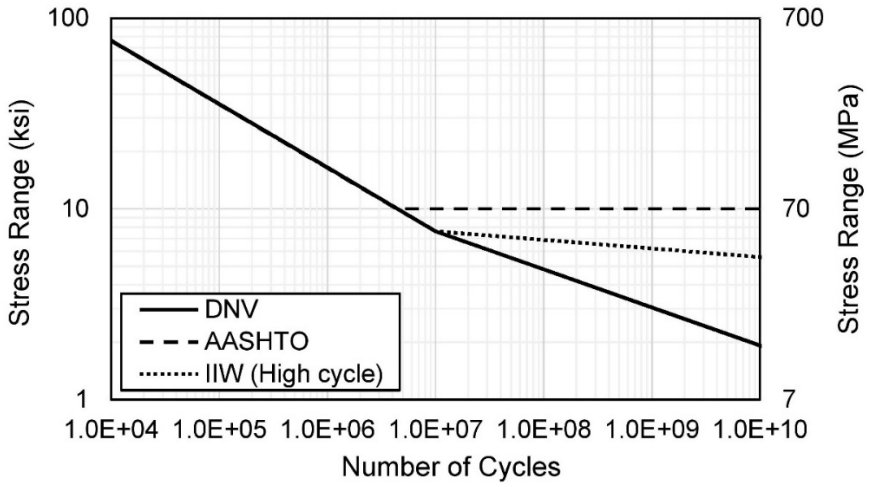

Figure 1.5: Fatigue Resistance S-N Curve of Steel Details for Structural Hot-Spot Stress Analysis

Linear-elastic material properties are usually adopted in finite element models for structural HSS analysis. Niemi et al. (2018), DNV (2011), and AASHTO (2013) all recommend use of quadratic 20-node solid elements with reduced integration. AASHTO (2013) requires a mesh size of $t \times t$ to be used for at least three rows in front of the weld toe, and at least two elements in the through-thickness direction. A maximum aspect ratio of 1:4 is prescribed, and the elements should have corner angles between 30° and 150°. As further context to the AASHTO LTS requirements, DNV (2011) indicates that the first two or three elements in front of weld toe in a tubular joint should be chosen as $t \times t$. The breadth of each element should be smaller than the thickness of the attached plate plus two times the weld leg length, and the length of the element should not exceed $2t$. DNV (2011) recommends the elements to have corner angles between 60° and 120° and aspect ratios to be less than 5.0.

It is important to note that since the structural HSS is obtained at the surface of the weld toe, the HSS technique is not applicable for analyzing weld root cracking or any cracking initiated at a weld surface (Hobbacher, 2008). Moreover, AASHTO (2013) indicates that the hot-spot stress method is only applicable in finite life analyses, but this limitation is not described in IIW (Hobbacher, 2008; Niemi et al., 2018) or DNV (2011).

Chapter 2: Methods

This chapter describes the research methodology used in this investigation. Both analytical modeling techniques and forensic investigation methods are detailed in this chapter.

2.1 Forensic Methods

The following sections detail the methods used in the forensic investigation of the cracked HMIPs provided to the research team by KDOT.

2.1.1 Crack Surface Investigation

Four HMIPs were identified by KDOT in March 2019 to have visible or potential cracking and were removed from service. They were sent to the KU research team for investigation. The four poles were 097L017 from Colby, KS, hereafter referred to as Pole A; 032L019 from Wakeeney, KS, hereafter referred to as Pole B; 097L018 from Colby, KS, hereafter referred to as Pole C; and 091L005 from Ruleton, KS, hereafter referred to as Pole D. Figures 2.1 to 2.4 show the flaws for which the HMIPs were removed from service. A description of visible or potential cracking observed for each of the poles at the time of removal from service follows:

- ***Pole A*** – Dye penetrant testing in the field identified potential surface cracks at the toe of the reinforcing fillet weld on the top right and bottom right of the handhole.
- ***Pole B*** – Displayed extensive, visible cracking at the toe of the reinforcing fillet weld around the entire top of the handhole with horizontal cracks branching into the pole base metal at the end of each radius.
- ***Pole C*** – Displayed extensive, visible cracking at the toe of the reinforcing fillet weld from the top middle of the handhole to the end of the right radius with a horizontal crack branching into the pole base metal.
- ***Pole D*** – An imperfection in the toe of the reinforcing fillet weld on the right side of the handhole and a surface scratch near the grounding lug

was identified as a potential crack and removed out of an abundance of caution.

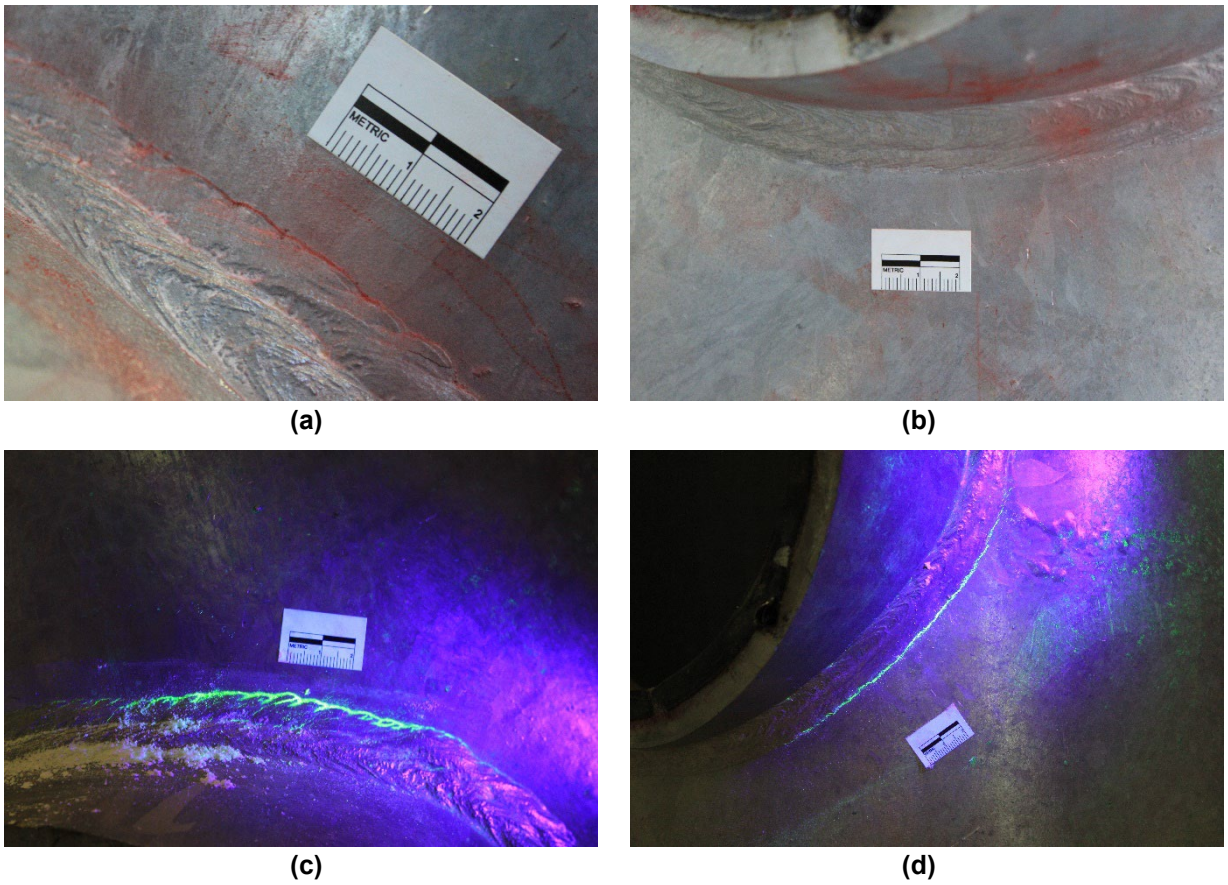

Figure 2.1: Pole A - Evidence of Surface Cracking on the (a) Top Right and (b) Bottom Right of the Handhole Before and After, (c-d) Dye Penetrant Testing

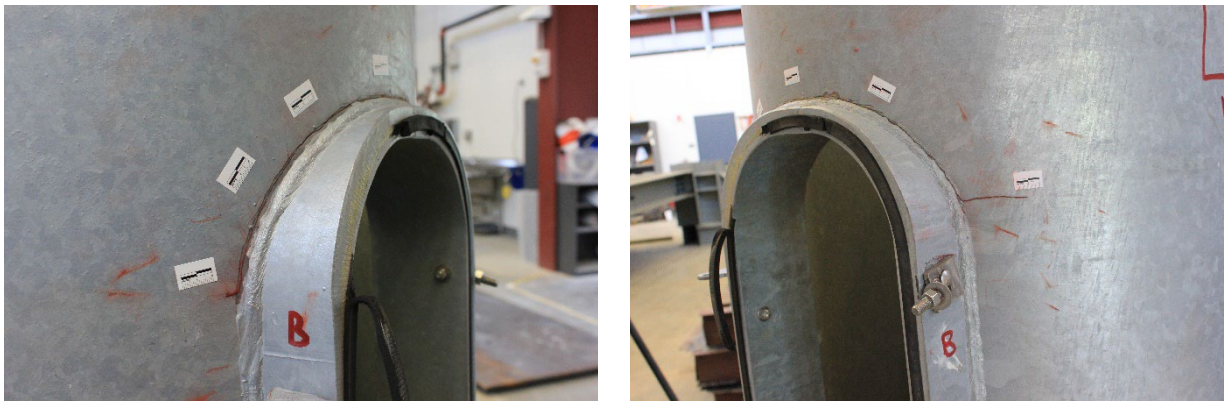

(a) (b)

Figure 2.2: Pole B - Extensive Cracking at Top of the Handhole Weld with Horizontal Cracks Growing into the Pole Base Metal on the (a) Left and (b) Right Sides

(a) (b)

Figure 2.3: Pole C - Extensive Cracking From (a) the Top Middle of the Handhole to (b) the Right Radius with a Horizontal Crack Growing into the Pole Base Metal

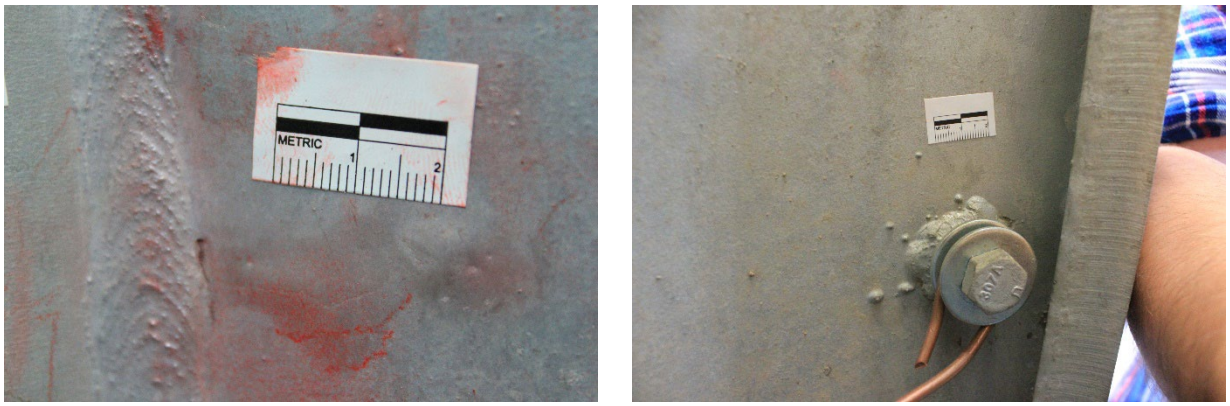

(a) (b)

Figure 2.4: Pole D - Potential Flaw (a) in the Reinforcing Fillet Weld Toe and a Surface Scratch Near (b) the Grounding Lug Welded on the Interior

To examine the crack surfaces, the handholes and surrounding areas were first plasma or flame cut out of the surrounding pole to allow for easier handling. Poles A and C were smaller in diameter and lighter, allowing them to be plasma cut while laid horizontally, shown in Figure 2.5. Poles B and D were too heavy to be laid horizontally safely so they were flame cut while standing vertically, as shown in Figure 2.6. The plasma and flame cuts were made several inches from any potential cracks to avoid damaging the crack surfaces. Extra material was also left at the top for obtaining Charpy V-Notch (CVN) specimens, which is discussed in Section 2.1.2. A vertical bandsaw was then used to isolate the cracked sections of the handhole from the rest of the uncracked handhole, as shown in Figure 2.7.

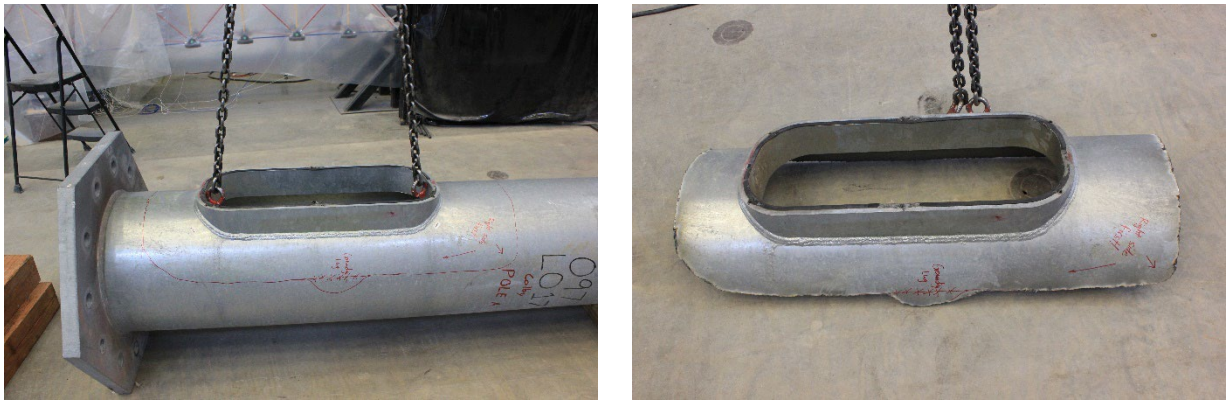

(a) (b)

Figure 2.5: The Supports Used for (a) Plasma Cutting Poles A and C and (b) the Handhole Removed from Pole A

(a) (b)

Figure 2.6: (a) Supports used for Flame Cutting Poles B and D and (b) the Handhole Removed from Pole B

Figure 2.7: Vertical Bandsaw Used to Further Process Each Handhole

Next, cuts were made to the identifiable crack tips on each handhole. For Poles B and C, once the crack tips had been reached with the saw blade, the reinforcing rim and pole broke apart

since the cracks were through-thickness. Then cuts were made below the point where the horizontal cracks began to grow to determine the extent of the weld toe cracks. For Poles A and D, there were no through-thickness cracks. Once cuts were made to the tips of the area believed to possibly be cracked, the potential cracks were cut into thin slices so that welds could be inspected in those areas. Figure 2.8 shows the cuts made to remove the cracked sections and Figure 2.9 shows the cuts made to fully examine each crack. Once the cutting was finished, the sections that contained welds were polished with 600 grit sandpaper and etched using a 5% nital etching solution to make the weld profile clearly visible. Photographs of each crack surface and of the etched weld profiles are presented in Chapter 3.

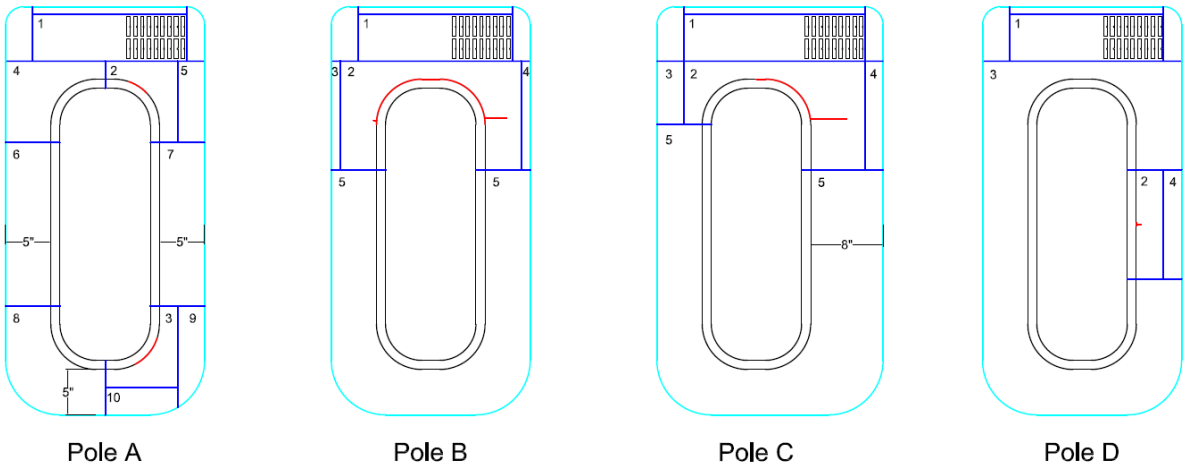

Figure 2.8: Cuts Made to Remove Each Cracked Section and CVN Specimen Material

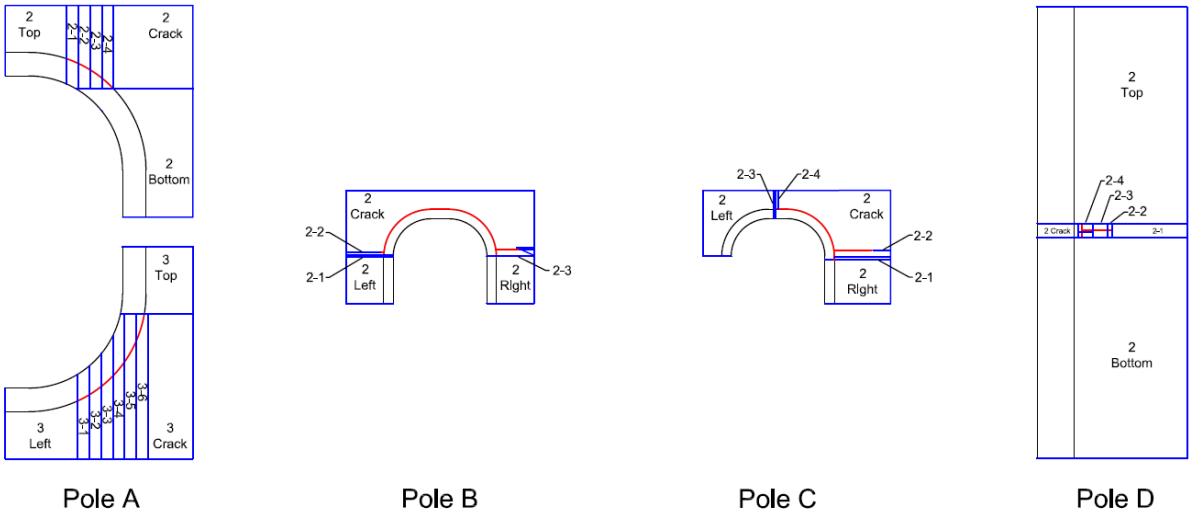

Figure 2.9: Detailed Cuts Made to Partition the Cracked Sections and Determine the Extent of Cracking

2.1.2 Pole Material Testing

The pole base metal was tested to determine its impact toughness. While impact toughness would not necessarily affect the initiation of the cracks around the handhole weld, the horizontal cracks that grew into the poles would be considered more severe from the perspective of fracture potential in the presence of a less tough material.

Eighteen sub-size CVN specimens were sampled from each pole as shown in Figure 2.8. Standard CVN specimens per ASTM E23 (2016) are 0.39 × 0.39 × 2.17 in. with a 0.08-in.-deep notch centered on one face to leave a 0.32-in. remaining ligament. However, the 0.25-in. pole thickness prevented fabrication of full-thickness specimens. As such, the specimens sampled were 0.39 × 0.20 × 2.17 in. with a 0.32-in. remaining ligament in accordance with ASTM E23 Annex A3. The CVN specimens were tested using an impact hammer with a capacity of 400 ft-lbf. To compensate for the reduced thickness, 0.10-in.-thick shims were placed under the specimen seats to keep the center of the striker in the center of the specimen as per ASTM E23 Appendix X3 (ASTM E23, 2016).

The CVN specimens were tested at a range of temperatures from -112 to 40 °F (-80 to 4.4 °C) to establish the lower shelf, upper shelf, and transition region that are characteristic of structural steel impact toughness, ascertained over a range of temperatures. Steel becomes more

brittle at lower temperatures and fractures at a lower impact energy, approaching the lower shelf. Inversely, steel is more ductile and fractures at a higher impact energy at warmer temperatures, approaching the upper shelf. Between the two shelves is the area known as the transition region. To characterize the impact energy curves for each pole, two specimens from each pole were tested at -112, -90, -60, -30, 0, 20, and 40 °F. The remaining four specimens from each pole were tested one each at -60, -30, 0, and 20 °F to increase confidence in the transition region results. The impact energy versus temperature data was then fit with a five-parameter sigmoid line given by Equation 2.1, where *a* is the asymptotic minimum, *b* is the asymptotic maximum, *c* is the location parameter, *d* is the slope parameter, *m* is the scale parameter, and *T* is the test temperature. This allowed for a simpler comparison between the CVN results for the four HMIPs.

$$a + \frac{b}{\left(1+exp^{\frac{(-T-c)}{d}}\right)^{m}}$$

Equation 2.1

Typically, sub-size CVN data are shifted positively for temperature to account for the lower ductile-to-brittle transition temperature of sub-size specimens compared to full-size specimens (Wallin et al., 2016). Additionally, the reduced CVN specimen size results in a lower impact energy and can be corrected in a number of ways (Lucon et al., 2016). However, because the results here were only intended for comparison between the four HMIPs, the temperature shifts and energy corrections were not applied in this study.

2.1.3 Metallurgical Chemistry Analysis

A 1 × 1 × 1-in. cube of steel material was extracted from each HMIP and sent to Chicago Spectro to have the chemistry of the steel analyzed. The chemistries were then compared with the chemistry requirements for A572 steel (ASTM A572, 2018) and are presented in Chapter 3. The carbon equivalent (CE) for each of the poles was also calculated using Equation 2.2 from the American Welding Society (AWS) D1.1, where *C* is carbon, *Mn* is manganese, *Si* is silicon, *Cr* is chromium, *Mo* is molybdenum, *V* is vanadium, *Ni* is nickel, and *Cu* is copper, each in terms of percent weight (AWS, 2015).

$$C + \frac{1}{6}(Mn + Si) + \frac{1}{5}(Cr + Mo + V) + \frac{1}{15}(Ni + Cu)$$

Equation 2.2

The carbon content and carbon equivalent were used to classify the steel into one of three zones that indicate weldability and likelihood of heat affected zone (HAZ) cracking:

- ***Zone 1*** – The steel is easily weldable and HAZ cracking is unlikely.
- ***Zone 2*** – The steel is moderately weldable and HAZ cracking is possible.
- ***Zone 3*** – The steel is difficult to weld and HAZ cracking is likely.

2.2 Finite Element Modeling

A series of finite element analyses were performed using Abaqus v.2016 to evaluate the fatigue performance of the handhole details and base plate details in high mast illumination poles. The first series of analyses were parametric analyses. Based on the geometry of a typical HMIP design provided by KDOT, design parameters were varied one at a time to evaluate their influence on stresses at the handhole and base plate details. These parameters included pole thickness, handhole corner radius, handhole width, handhole height, handhole position, weld geometry around the handhole, level of tension in the anchor bolts, and reinforcing rim thickness. The parametric analyses provided information for choosing optimized pole geometries. These models were created using the 8-node linear solid elements with reduced integration (C3D8R).

A second series of analyses evaluated the influence of a subset of parameters on proposed updated designs. The models in the second part were created using the 8-node linear solid elements with reduced integration (C3D8R).

A third series of models were created using the geometries of the original pole and a doubler plate detail modified from the original pole. The AASHTO fatigue loading and "bomb cyclone" loading estimated from a video taken of an HMIP undergoing large-amplitude oscillations during the 2019 winter storm event were applied. The structural hot-spot stress method was used to evaluate the susceptibility of the handhole and base plate details to fatigue damage. The goal of this part of the study was to evaluate the stress magnitude and distribution of the current design and consider the effectiveness of using a doubler plate retrofit. The models in the

third part were created using the 20-node quadratic solid elements with reduced integration (C3D20R).

The fourth series of analyses were aimed at evaluating a new design provided by KDOT under AASHTO design-level fatigue loading, proposed by KDOT for use in future HMIP construction. The models in this series were created using the 20-node quadratic solid elements with reduced integration (C3D20R).

2.2.1 Parametric Analyses and Optimizing Pole Geometries

3D models were created to resemble actual HMIP geometries based on the design drawings provided by KDOT as faithfully as possible. Linear-elastic material properties were used in all the models, with a modulus of elasticity of 29,000 ksi and Poisson's ratio of 0.3. The weight density of the steel was defined as 0.000284 kip/in^3.

The overall geometries of the structure and the cutaway of the base plate and the handhole details are presented in Figure 2.10 and Figure 2.11. The original HMIP design (pre-2019) is constructed using two shafts, both of which are tapered. Shaft A (bottom) is 50.8 ft long and 0.25 in. thick, with a 25.50-in. diameter at the base and 18.39-in. diameter at the top. Shaft B (top) is 52.68 ft long and 0.188 in. thick, with a 19.25-in. diameter at the base and 11.87-in. diameter at the top. A 41.50-in. slip-fit overlap is created between the two shafts which are then welded together. The handhole is 12 in. wide and 32 in. tall, and its corners are rounded with a radius of 5 inches. The reinforcing rim is 1 in. thick, which makes the handhole opening 30 in. tall and 10 in. wide. The handhole detail in the original design utilizes a partial penetration bevel-groove weld with a root opening of 0.06 in., a depth of 0.19 in., and a 0.25 × 0.21-in. reinforcing fillet weld. The bottom of the handhole is positioned 26.5 in. above the top of the base plate, such that the center of the handhole is 42.5 in. (1.67D) above the base plate. The base plate is a 38-in.-wide and 2.25-in.-thick hexagon, with a center hole of 17-in. diameter. The 12 anchor bolts are 90 in. long, each with a diameter of 1.5 in., spaced evenly around a 32.5-in. diameter circle. The base plate-to-pole detail utilizes a full penetration bevel-groove weld and a 0.46 × 0.13-in. reinforcing fillet weld. A 3-in.-tall and 0.25-in.-thick backing ring is welded to the inside of the pole and the base

plate using two 0.19-in. fillet welds. The luminaires and the ring on the top of the pole weigh 458 lb and have an effective projected area (EPA) of 10.82 ft^2.

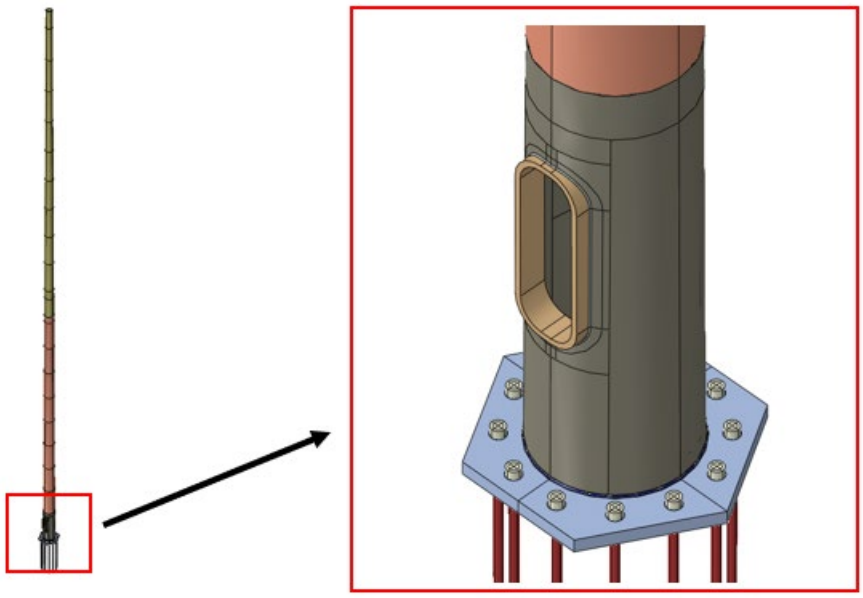

Figure 2.10: Finite Element Model of HMIP Original Design (pre-2019)

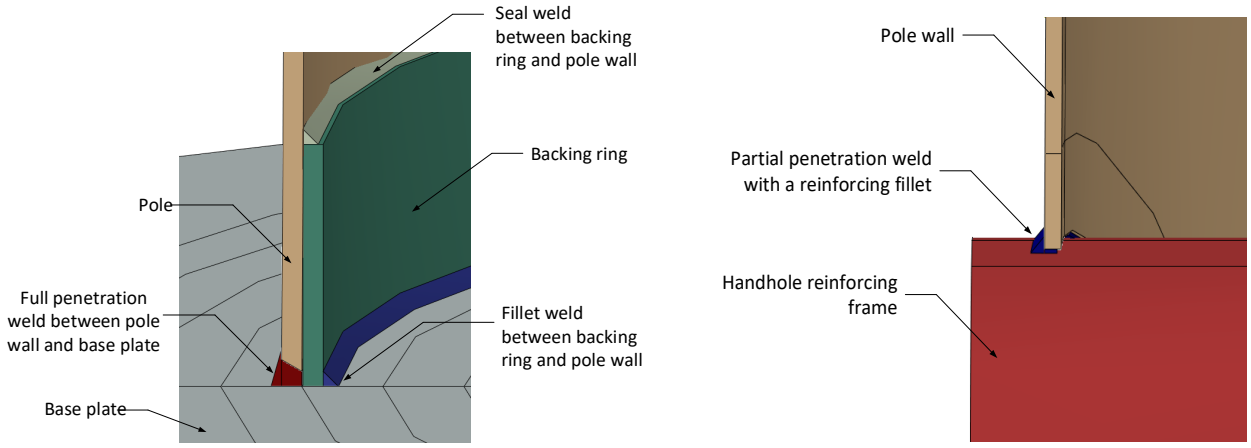

Figure 2.11: Cutaway View of Finite Element Model at the (a) Base Plate Detail and (b) Handhole Detail

3D solid elements were used throughout the HMIP models. Linear 8-node solid elements with reduced integration (C3D8R) were used throughout the model. The mesh is shown in Figure 2.12.

Shaft A was separated into two segments. The bottom segment of Shaft A where the handhole and base plate details are located was a 75.5-in.-long segment. A mesh size of 0.10 in. was assigned in the bottom segment of Shaft A. There were two elements through the thickness for poles less than 0.50 in. thick and three elements through the thickness for poles 0.50 in. thick and greater. All the elements in the bottom segment of Shaft A had corner angles between 30° and 150° and aspect ratios smaller than 4:1. The top segment of Shaft A and Shaft B were assigned a mesh size of 1.00 in. The reinforcing rim, the base plate, and the bolts were assigned a mesh size of 0.20 in. All the welds were assigned a mesh size of 0.10 in.

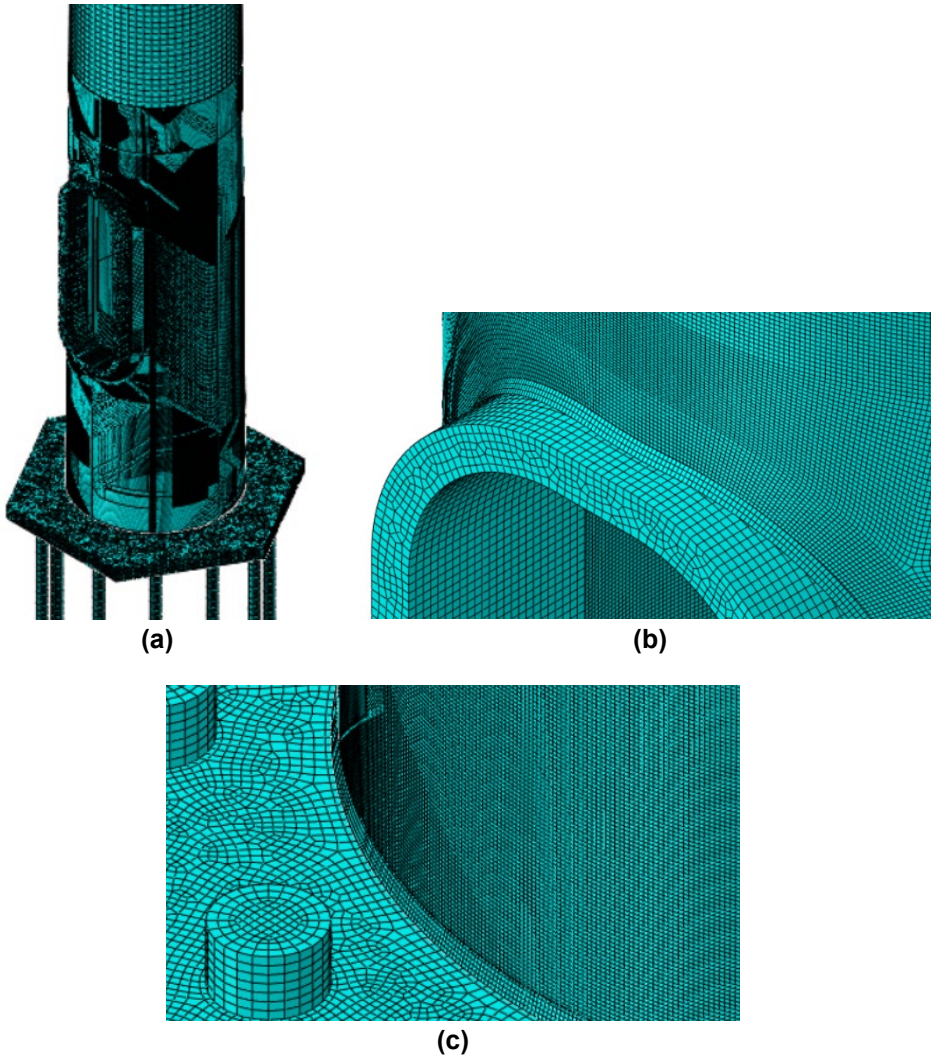

Figure 2.12: Mesh for (a) HMIP, (b) Handhole Detail, and (c) Base Plate Detail

The contact between the welds and the surfaces they connected were simulated as tie constraints, restraining all degrees-of-freedom (DOFs) between the two surfaces in contact with each other. All DOFs of the anchor bolts were restrained below the base plate, as shown in Figure 2.13(a).

Each analysis had three steps in addition to the initial step. The first was the bolt load step, in which the anchor bolts were pretensioned to 90% of the total yield strength (87.5 kip, considered here as 100% tensioned) in the original pole model. The second is the gravity step, which accounts for the weight of the pole and the luminaires. The weight of the pole was simulated by defining a downward acceleration in combination with material density for all model parts, and the weight of the luminaires was captured by applying nodal forces with a total value of 458 lb at the top of the pole.

Wind loads were applied in the third step. Design-level fatigue loads for high mast lighting towers were applied according to the AASHTO (2013) LTS Specifications, calculated using Equation 2.3 where P_{FLS} is the fatigue-limit-state static pressure and C_d is the drag coefficient. A value of 7.2 psf for P_{FLS} and a drag coefficient of 1.1 were used in the calculations. When EPA is used, $C_d = 1.0$.

$$P_{CW} = P_{FLS} C_d$$

Equation 2.3

The entire pole was separated into 21 segments. Wind loads were calculated based on the average diameter of each segment and applied as a nodal force along the centerline of the pole surface in a direction to induce maximum tensile stresses in the handhole detail. Wind load acting on the luminaires was calculated according to the EPA of 10.82 ft^2 and applied as a nodal force on the tip of the pole. The boundary conditions and the load placements are shown in Figure 2.13. Other than the first 0.5 in. below the bottom of bolt nuts, all DOFs of the nodes on the anchor bolt shank were restrained, simulating their being surrounded by a concrete foundation. The influence of geometric nonlinearity (second-order effects) was considered in the gravity and wind load steps.

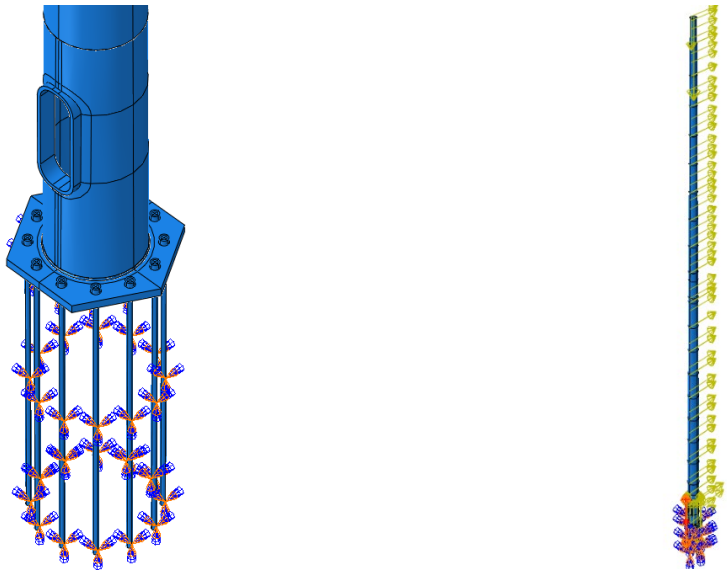

(a) (b)

Figure 2.13: (a) Boundary Conditions and (b) Load Placements of HMIP Finite Element Model

The parameters analyzed in this study are summarized in Table 2.1. The values denoted with an asterisk denote the base values of the variables, which are the geometries of the original HMIP design. Each parameter was changed one at a time while the other geometric features stayed the same as the original pole.

Table 2.1: Model Matrix for Parametric Analyses of HMIP

Parameter	Variations				
Handhole Corner Radius	0.3W	0.4W*	0.5W	-	-
Handhole Width	10”	12”*	16”	-	-
Handhole Height	16”	24”	32”*	-	-
Handhole Position	1.67D*	3D	4D	-	-
Handhole Weld Geometry	Fillet Weld	Partial Penetration and Fillet*	Full Penetration and Fillet	-	-
Anchor Bolt Tension Level	100%*	75%	50%	25%	0%
Base Plate Thickness	2.25”*	2.50”	3.00”	3.50”	-
Reinforcing Rim Thickness	1.00”*	0.75”	0.50”	0.25”	-
Pole Thickness	0.25”*	0.50”	0.625”	1.00”	-
Base Plate Hole Diameter	0”	12”	17”*	22”	-

The structural hot-spot stresses were taken as the nodal maximum (tensile) principal stress at a distance $0.1\sqrt{rt}$ away from the weld toes, which is 0.18 in. for 0.25-in.-thick pole, 0.2 in. for the 0.375-in.-thick pole, 0.25 in. for the 0.5-in.-thick pole, and 0.28 in. for the 0.625-in.-thick pole. The location of peak stress was found by extracting stresses along a predefined nodal path along the weld toe on the outer surface of the pole, as shown in Figure 2.14. After determining the hot-spot, stresses were extracted along a nodal path perpendicular to the weld at the hot-spot, as shown in Figure 2.15. Linear interpolation was performed to compute the stresses if nodal stresses were not available at the required distance.

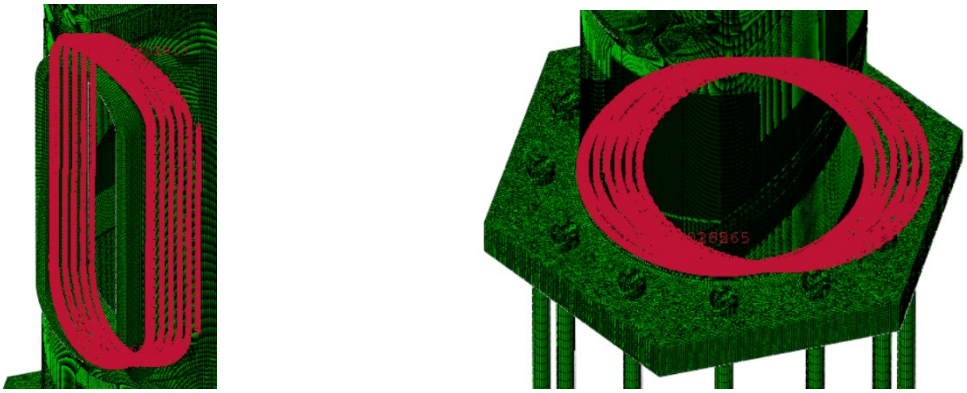

(a) (b)

Figure 2.14: Node Paths around the (a) Handhole Detail and (b) Base Plate Detail

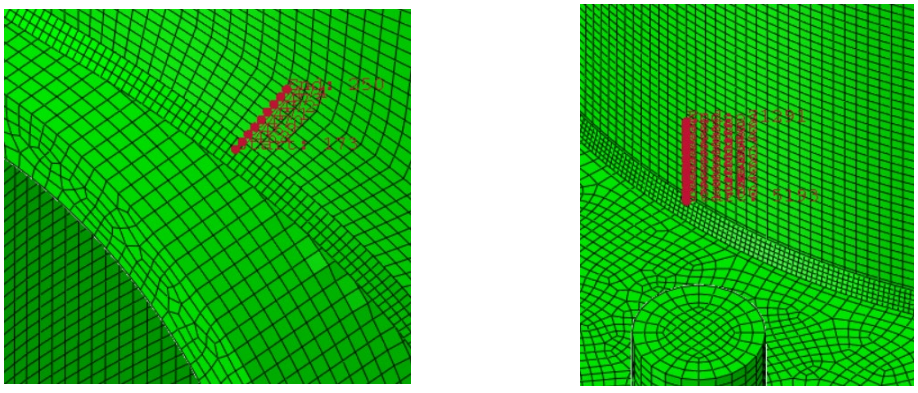

(a) (b)

Figure 2.15: Node Paths Perpendicular to the (A) Handhole Weld and (B) Base Plate Weld at Hot-Spots

2.2.2 Additional Parametric Analyses

Five parametric analyses based on different geometries were performed in addition to the analyses presented in Section 2.2.1, to evaluate the influence each parameter had on design changes under consideration. As shown in Table 2.2, the five additional analyses were,

1. varying pole thickness based on a pole without a reinforcing rim,
2. varying base plate thickness based on a 0.625-in.-thick pole,
3. varying base plate hole diameter based on a 0.625-in.-thick pole,
4. varying reinforcing rim thickness based on a 0.625-in.-thick pole, and
5. varying reinforcing rim thickness based on a 0.50-in.-thick pole with a full-penetration weld at the handhole.

Table 2.2: Additional Parametric Analyses

Parameter	Variations (in.)				
Pole Thickness 1/2-in.-thick pole with no reinforcing rim at handhole	0.25	0.375	0.50	0.625	-
Base Plate Thickness 5/8-in.-thick pole with partial penetration handhole weld	2.25	2.50	3.00	3.50	-
Base Plate Hole Diameter 5/8-in.-thick pole with partial penetration handhole weld	0	12	17	22	-
Reinforcing Rim Thickness 5/8-in.-thick pole with partial penetration handhole weld	1.00	0.75	0.50	0.25	0.00
Reinforcing Rim Thickness 1/2-in.-thick pole with full penetration handhole weld	1.00	0.75	0.50	0.25	0.00

The other details of the finite element models, including geometries, contact and interaction, mesh, element type, loading, and boundary conditions were unchanged from those described in Section 2.2.1. The structural hot-spot stresses were also extracted at the same locations as described in Section 2.2.1.

2.2.3 Analysis of Original Pole and Pole with Doubler Plate Handhole Detail Under Fatigue Loading and "Bomb Cyclone" Loading

In the model analyzed in this portion of the study, the material properties, geometries, boundary conditions, and contact and interactions of the original pole were the same as those introduced in Section 2.2.1. The doubler plate HMIP model was adapted from the model of the original pole. As shown in Figure 2.16, instead of a reinforcing rim, a 0.625-in.-thick doubler plate was welded on top of the handhole. The other features of the pole were unchanged from the original pole.

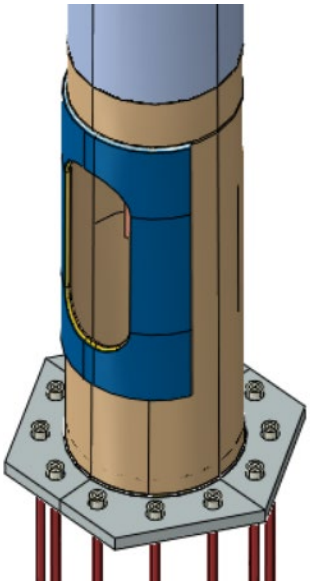

Figure 2.16: Doubler Plate Handhole Detail

For the models described in this Section, 20-node quadratic solid elements with reduced integration (C3D20R) were used in the bottom segment where the handhole and the base plate details were located. A mesh size of 0.2 in. was assigned to the entire bottom portion of the model. The elements and mesh in the other parts of the HMIP were the same as for the model described in Section 2.1.1.

For these analyses, the pole was loaded under design-level fatigue loads computed according to AASHTO (2013), and separately, under a "bomb cyclone" load for evaluating the stress of the pole under large oscillations observed during a storm event. To estimate the influence of the "bomb cyclone" load, the aforementioned fatigue loading was magnified to match the pole

tip displacement estimated from a video taken during the storm. As shown in Figure 2.17(a), the pole in the video is about 100-ft tall with reference lines drawn in red. The estimated maximum peak-to-peak deflection amplitude was approximated to be 60 in., and the estimated average peak-to-peak deflection amplitude was approximately 52 in. Therefore, the fatigue load was amplified by a factor of 5.6 to produce a 55-in. displacement at the pole tip in the finite element analysis, as shown in Figure 2.17(b).

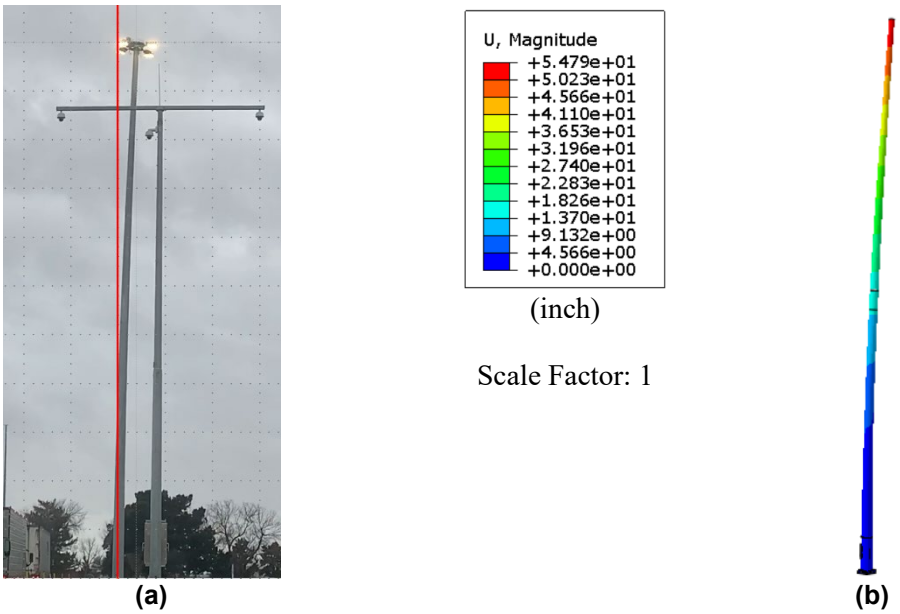

Figure 2.17: Displacement of High Hast Illumination Pole in (a) Video Taken During the 2019 Winter Weather Event and (b) Finite Element Analysis

2.2.4 Analysis of Kansas DOT New HMIP Design

This part presents analysis of a newly proposed KDOT HMIP design. The model was similar to that of the original pole presented in Section 2.2.1 but with different geometries. The new designs provided by KDOT for evaluation included three HMIP heights, including 100 ft, 110 ft, and 120 ft. To be conservative, the tallest pole was considered here. The proposed pole design consisted of three shafts: Shafts A, B, and C, labeled from the bottom to the top of the pole. Shaft A was a 28.95-ft-long and 0.50-in.-thick tapered pole with a bottom diameter of 26 in. and a top diameter of 21.95 in. Shaft B was a 48.73-ft-long and 0.2-in.-thick tapered pole with a bottom diameter of 23 in. and a top diameter of 16.18 in. Shaft C was a 49.46-ft-long and 0.1875-in.-thick

tapered pole with a bottom diameter of 17.00 in. and a top diameter of 10.08 in. The joints between Shafts A and B and Shafts B and C had minimum slip length requirements of 33.75 in. and 24.94 in., respectively. The actual slip lengths modeled were 47.16 in. and 37.92 in. between Shafts A and B and Shafts B and C, respectively.

The base plate thickness was increased to be 3 in. and the base plate center hole was increased to have a diameter of 23.5 in. The BP-Pole reinforcing fillet weld was resized to be a 0.88 × 0.25-in. fillet weld, while the backing ring geometry was unchanged.

The handhole location and size and reinforcing rim thickness were unchanged from prior models considered in this study. However, the reinforcing rim connection was modified from a partial penetration weld to a full penetration weld with a 0.38-in. root. A 0.69 × 0.38-in. fillet weld was used to reinforce the full penetration weld. This was done to address the lack of fusion at the weld root noted in Chapter 3 of this report and in prior research by Roy et al. (2011).

The BP and handhole details are shown in Figure 2.18(a). The bottom 80-in. segment of Shaft A was created as a separate part and was connected to the top part of Shaft A using tie constraints. The fillet welds were modeled explicitly and tied to the surfaces they connected. Since full penetration welds were adopted in the proposed design, the cross-sections of the pole were fully tied to the reinforcing rim and the BP to simulate the effect of the full penetration weld.

The boundary conditions and the load applications are shown in Figure 2.18(b) and (c). The bolt loads and gravity load applications were the same as those described in Section 2.1.1. The EPA and the weight of the luminaires was 12.28 ft^2 and 961 lb in the new design. The wind load was calculated using Equation 2.3 in Section 2.2.1. The pole was divided into 24 segments for the purpose of loading the model; the average diameter of each segment was used to determine the wind load. The wind load was applied the same way as in Section 2.1.1. Other than the first 0.50 in. below the bottom of bolt nuts, all DOFs of the nodes on the anchor bolt shank were restrained.

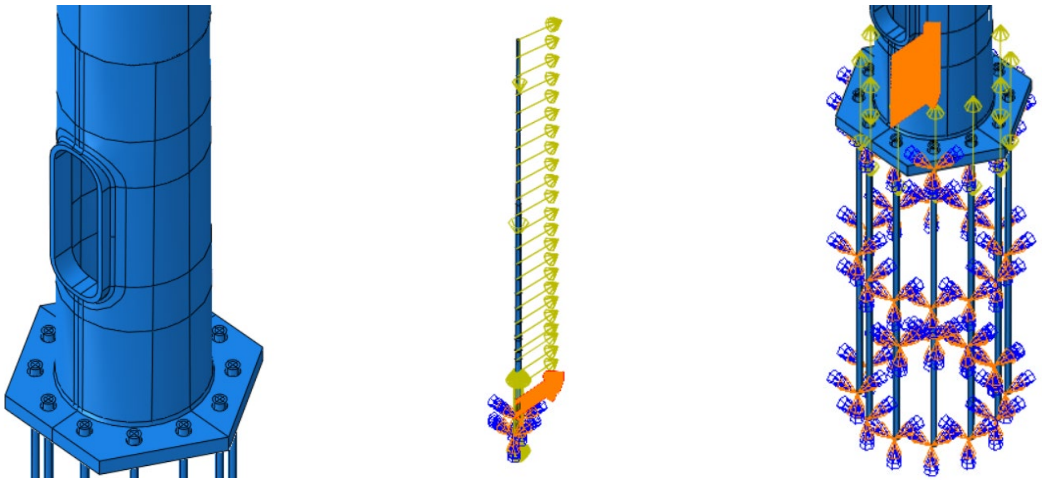

Figure 2.18: Model of New KDOT HMIP Design (a) at the Base Plate and Handhole Details, (b) Wind Load Application, and (c) Boundary Conditions

The 20-node quadratic solid elements with reduced integration (C3D20R) were used to create the bottom segment of Shaft A in the models, and a mesh size of 0.20 in. was assigned to this part. Three elements were used through the thickness of the pole. The remainder of Shaft A and Shafts B and C were created using 8-node linear elements with reduced integration (C3D8R), with meshes the same as those introduced in Section 2.2.1.

Chapter 3: Results

In this chapter, the results of both the forensic investigation of the cracked sections and the finite element modeling are summarized. The most relevant crack surface images are presented here, while Appendix A contains all crack surface images. Finite element results are presented in terms of percent change in peak stress at the weld toe as calculated using the hot-spot stress analysis method.

3.1 Forensic Results

The following sections discuss the results of the crack investigation, the pole material testing, and the metallurgical chemistry analysis performed on the cracked HMIPs removed from service.

3.1.1 Crack Surface Investigation

3.1.1.1 Pole A

The cracks that were identified from dye penetrant testing in Pole A were not through-thickness as evidenced by the lack of dye penetrant on the interior of the handhole weld. Once cuts were made to the crack tips, the potential crack was cut into 0.5-in.-wide strips to allow for inspection of the weld as shown in Figure 3.1. The top right crack was labeled Section A-2, and the bottom right crack was labeled Section A-3.

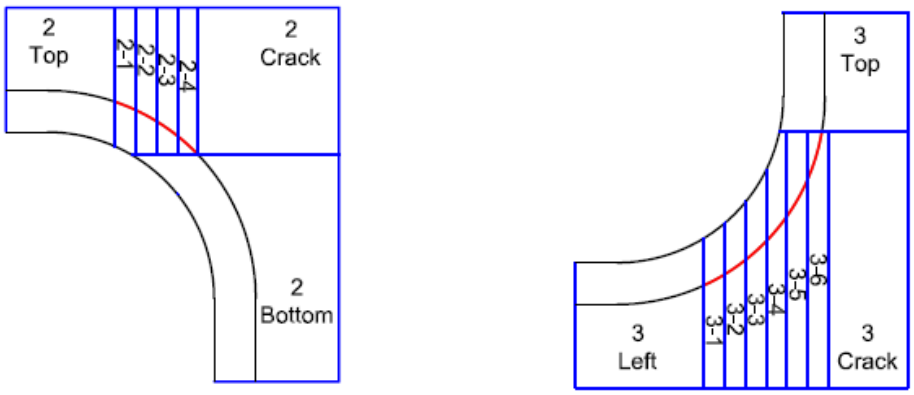

(a) (b)

Figure 3.1: Detailed Cuts for Pole A at (a) the Top Right and (b) the Bottom Right

After polishing and etching the strips from Section A-2, a number of factors that potentially contributed to the handhole cracking became apparent and are shown in Figures 3.2 and 3.3.

- ***Partial Penetration Weld*** – the partial penetration weld did not fully fuse the reinforcing rim and the pole at the weld root. This resulted in the root of the weld acting as an embedded crack, creating stress concentration, and reducing the effective throat of the weld.
- ***Incomplete Reinforcing Fillet Weld*** – the fillet welds did not cover the entire groove made in the pole in preparation for the welding. This created a sharper angle between the toe of the fillet weld and the pole, increasing the stress concentration. This sharp angle is also what was detected by the dye penetrant test as an indication of a crack.

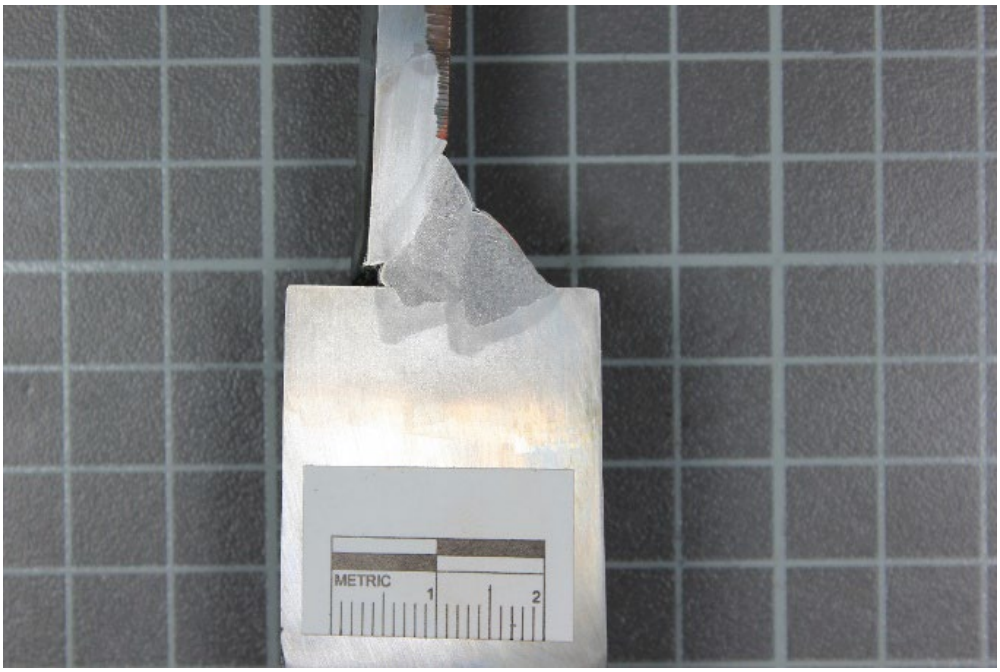

Figure 3.2: Weld Profile of the Left Side of Section A-2-1

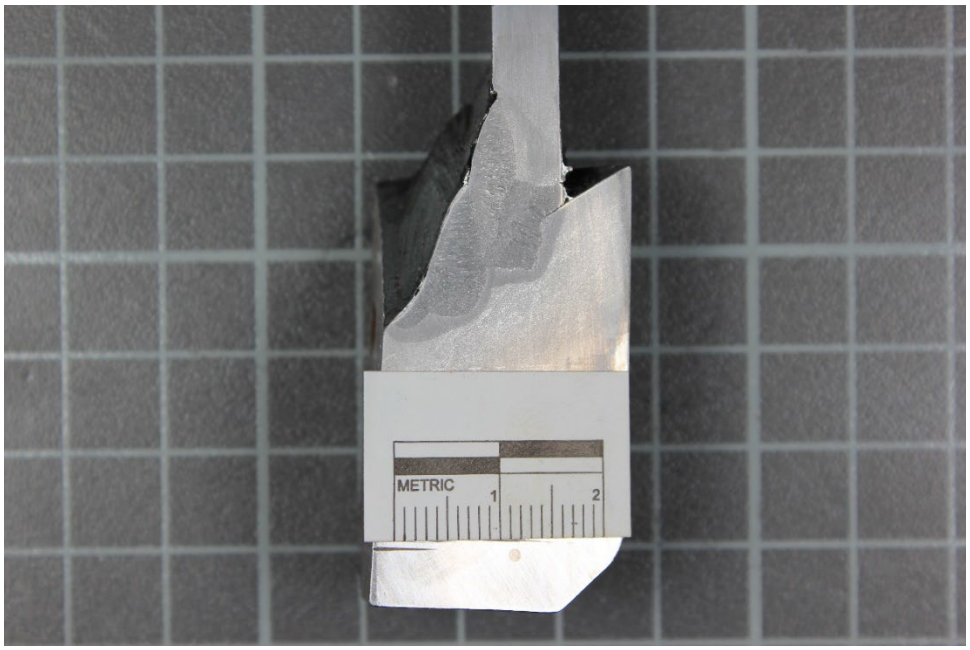

Figure 3.3: Weld Profile of the Right Side of Section A-2-1

The weld profiles for Section A-3 exhibited better fusion at the weld root and the reinforcing fillet weld provided more complete coverage of the pole. Compared to Section A-2, the weld at Section A-3 had shallower penetration into the reinforcing rim, as shown in Figure 3.4. While not an issue for this weld, any further reduction of the penetration could result in a large lack of fusion flaw similar to the weld root shown in Figure 3.3.

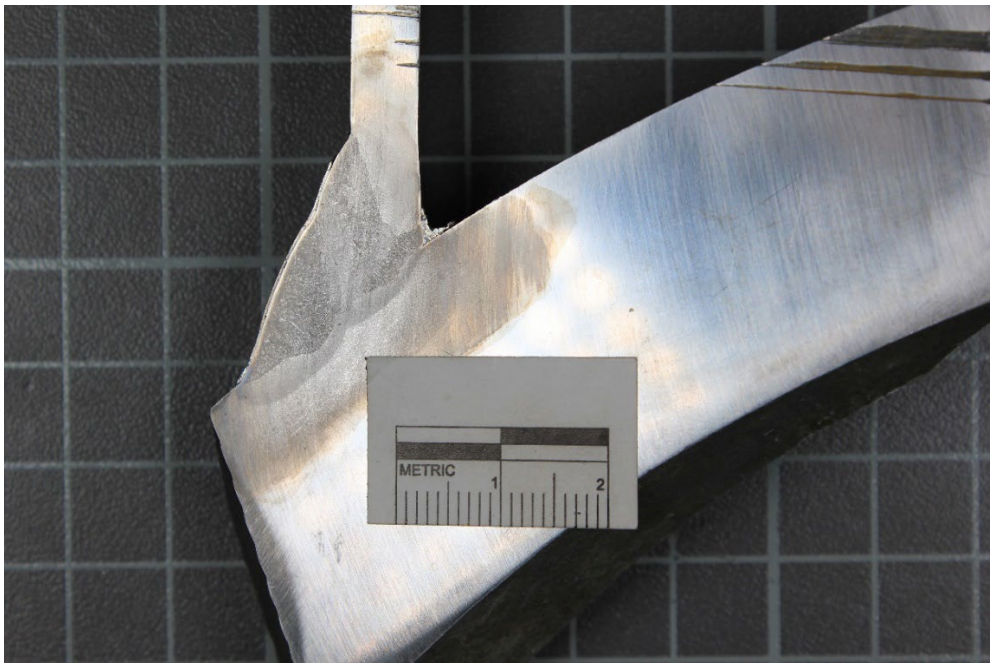

Figure 3.4: Weld Profile of the Left Side of Section A-3-3

3.1.1.2 Pole B

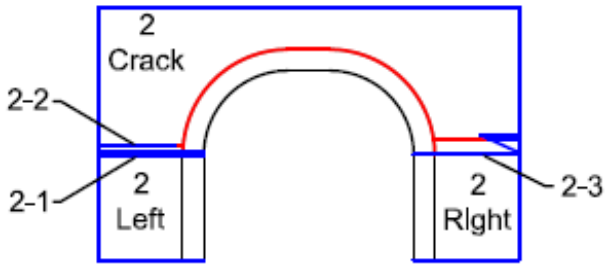

Figure 3.5: Detailed Cuts for Pole B

Pole B had the most severe cracking of the four HMIPs removed from service by KDOT. Figure 3.5 illustrates the cuts that were made to the horizontal crack tips to determine the extent of the cracking. The weld profile of the top of Section B-2-1, shown in Figure 3.6, exhibited a lack of fusion at the weld root similar to that observed for Section A-2, as well as porosity in the weld that likely further contributed to cracking. The crack can be seen growing from the interior of the pole towards the pores, resulting in a thin ligament between the crack tip and the toe of the reinforcing fillet.

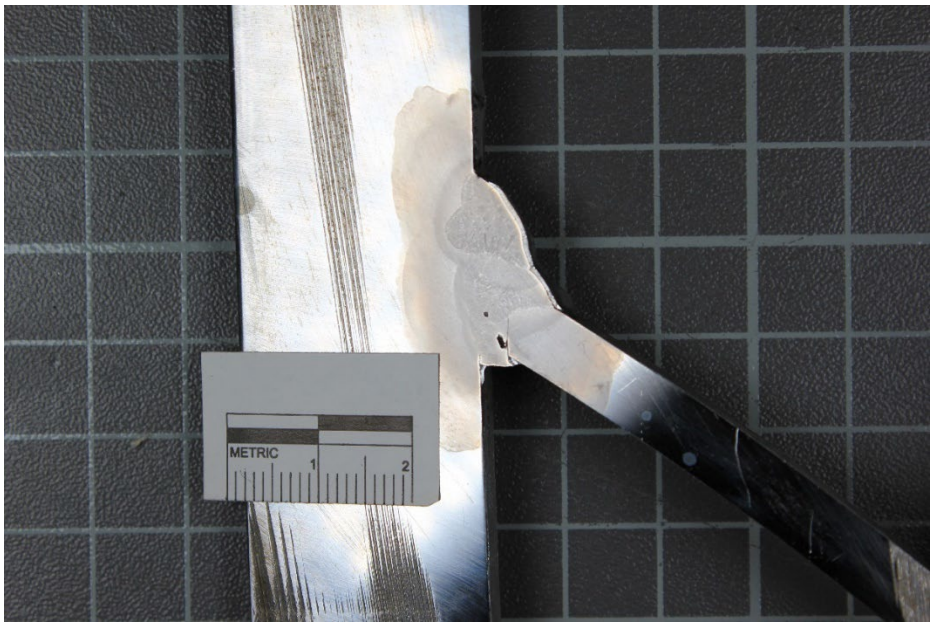

Figure 3.6: Weld Profile of the Top Side of Section B-2-1

The crack surfaces between the reinforcing rim and pole, the entirety of which are shown in Figure 3.7, display similar issues as observed in the weld profiles previously described. Figure 3.8 exhibits more porosity in the weld just to the left of center of the reinforcing rim and Figure 3.9 shows that the lack of fusion at the root of the weld resulted in a severely reduced weld throat. In this case, the gap on the interior of the weld was wide enough for the zinc to enter during galvanizing. The reddish-brown iron oxide of the crack surface shows that the crack only needed to grow approximately 0.118 in. before becoming through-thickness. Due to the combination of reduced weld throat and porosity, it was determined that the center of the reinforcing rim weld was the most likely origin of cracking.

Figure 3.10 shows the horizontal cracks that grew into the pole base metal. The striations along the right horizontal crack surface indicate that these cracks were due to fatigue and grew outwards from the handhole.

(a) (b)

Figure 3.7: Pole B (a) Reinforcing Rim and (b) Cracked Pole

Figure 3.8: Porosity in the Reinforcing Rim Crack Surface in Pole B

Figure 3.9: Lack of Fusion in the Center of the Pole B Crack Surface

(a) **(b)**

Figure 3.10: Horizontal Cracks at the (a) Left and (b) Right Sides of Pole B

3.1.1.3 Pole C

Pole C also exhibited extensive visible cracking, but to a lesser extent than Pole B. Figure 3.11 shows the detailed cuts that were made to the horizontal crack tip and to the handhole weld to assess the extent of cracking.

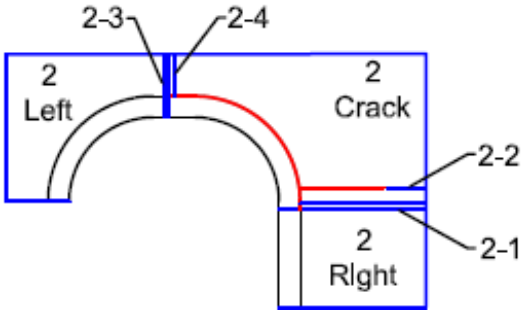

Figure 3.11: Detailed Cuts for Pole C

The weld profile on the left side of Section C-2-3, shown in Figure 3.12, exhibits similar features as the weld profiles of Pole A and B. The lack of fusion at the weld root resulted in an effectively embedded crack, noted as a potential problem from the profile of Section A-3-3. There is also an indication of an approximately 0.03-in. (0.75-mm) deep crack at the reinforcing fillet weld toe.

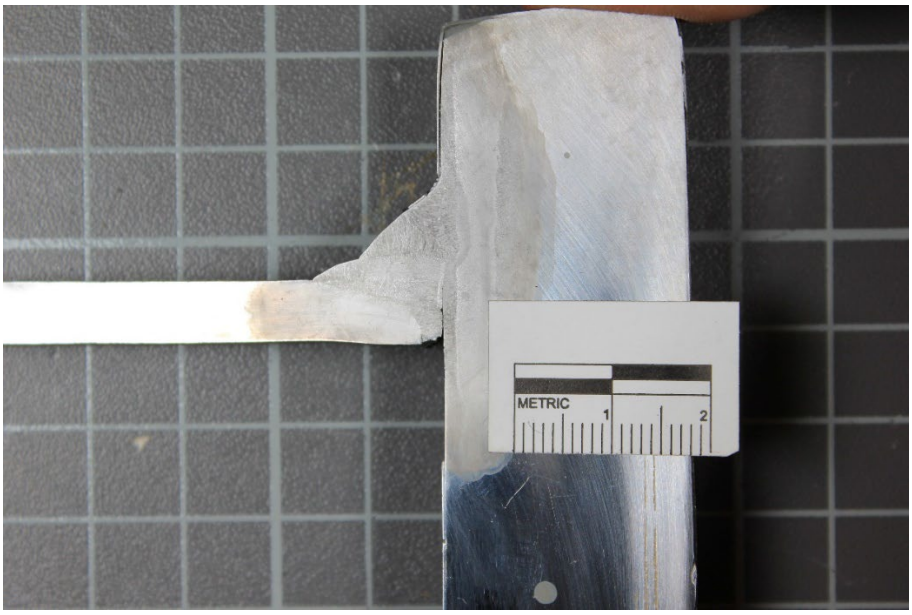

Figure 3.12: Weld Profile of the Left Side of Section C-2-3

The crack surfaces between the reinforcing rim and pole in Pole C, the entirety of which are shown in Figure 3.13, display similar issues to the crack surfaces in Pole B. Figure 3.14 shows evidence of porosity in the weld near the middle of the radius, similar to that seen in Figure 3.8. The crack surfaces from Pole C, however, are much darker than the crack surfaces of Pole B. This

is potentially due to the crack being formed before or during the galvanizing process. If the crack occurred during the cooling of the weld, it would likely be a very thin crack that would allow chemical cleaning agents to enter, but not the more viscous zinc (American Galvanizers Association, 2009). The salts left behind by the cleaning agents accelerate the formation of iron oxide and could explain the difference in crack surface coloration. The horizontal crack shown in Figure 3.15 also has clear striations, confirming that the horizontal cracks grew into the pole base metal from the handhole.

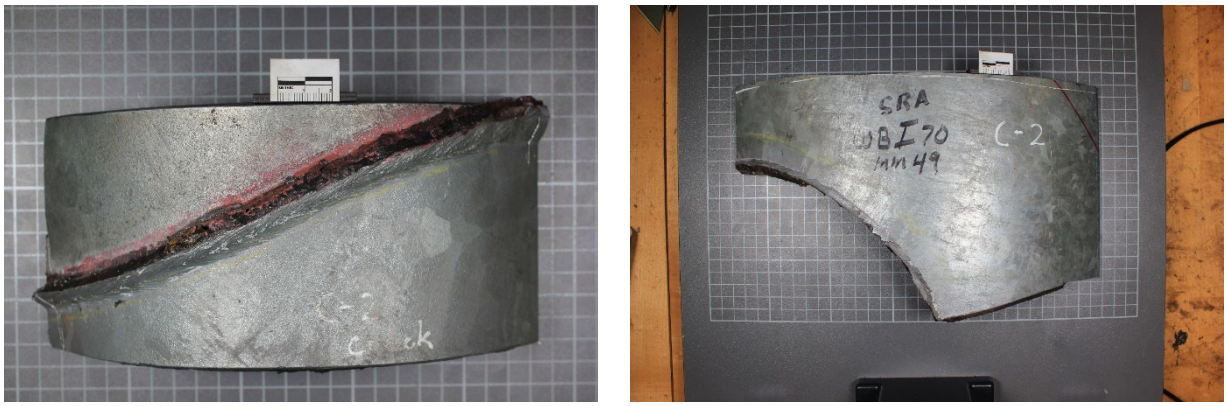

(a) (b)

Figure 3.13: Pole C (a) Reinforcing Rim and (b) Cracked Pole

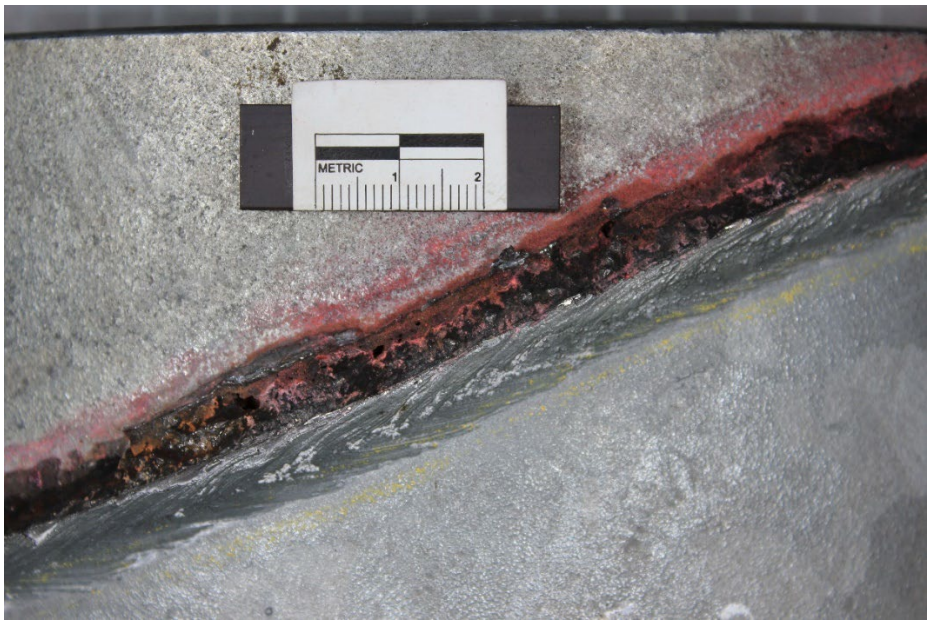

Figure 3.14: Porosity in the Reinforcing Rim Crack Surface in Pole C

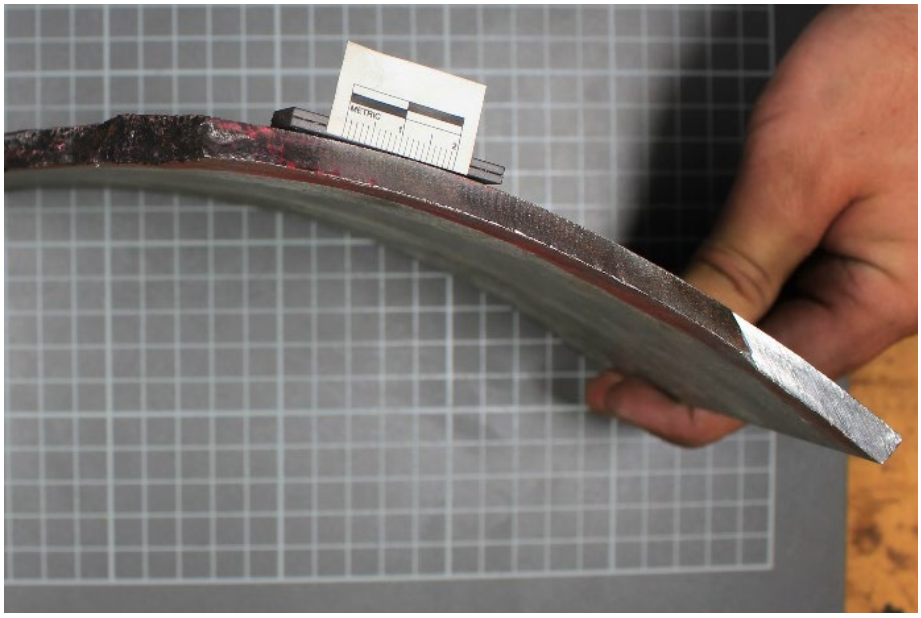

Figure 3.15: Horizontal Crack at the Right Side of Pole C

3.1.1.4 Pole D

The detailed cuts made to examine the potential flaws near the grounding lug in Pole D are shown in Figure 3.16. First, cuts were made into the tips of the potential crack at the weld toe, then the surface scratch was cut into small sections to be examined, similar to the process followed for

Sections A-2 and A-3. Lastly, the flaw at the weld toe was cut in half to allow the weld to be examined. Figure 3.17 shows the left and right sides of Section D-2-3, cut from the surface scratch, which do not show evidence of the scratch penetrating any deeper than the surface. Figure 3.18 shows the two halves of the suspected weld toe flaw, which also do not show any evidence of cracking.

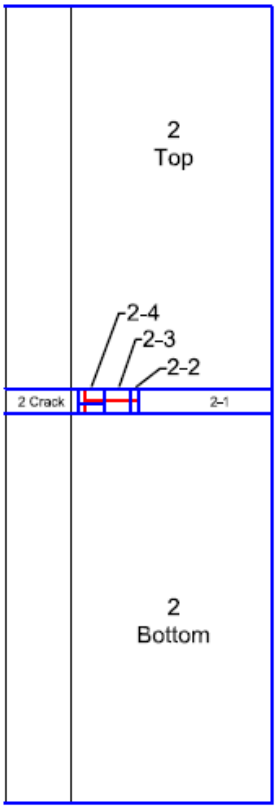

Figure 3.16: Detailed Cuts for Pole D

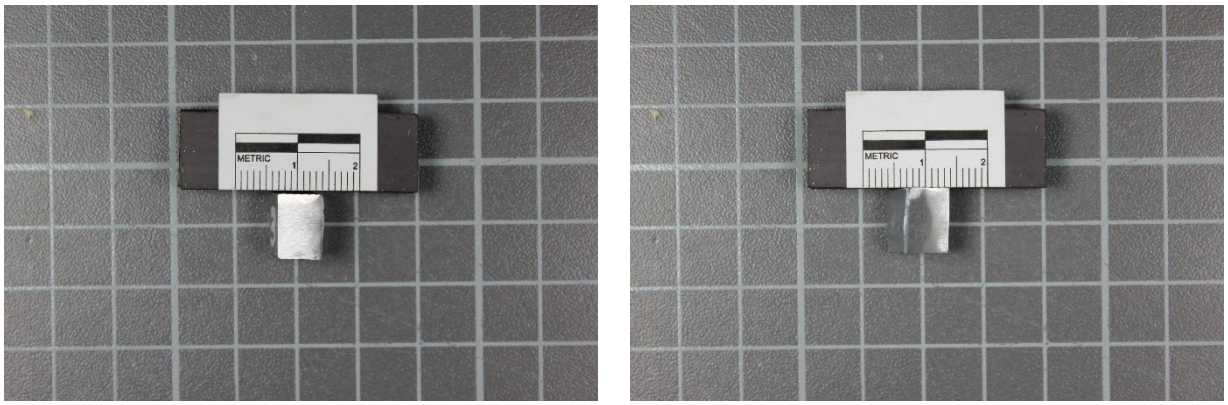

(a) (b)

Figure 3.17: Profiles of the (a) Left and (b) Right Sides of Section D-2-3

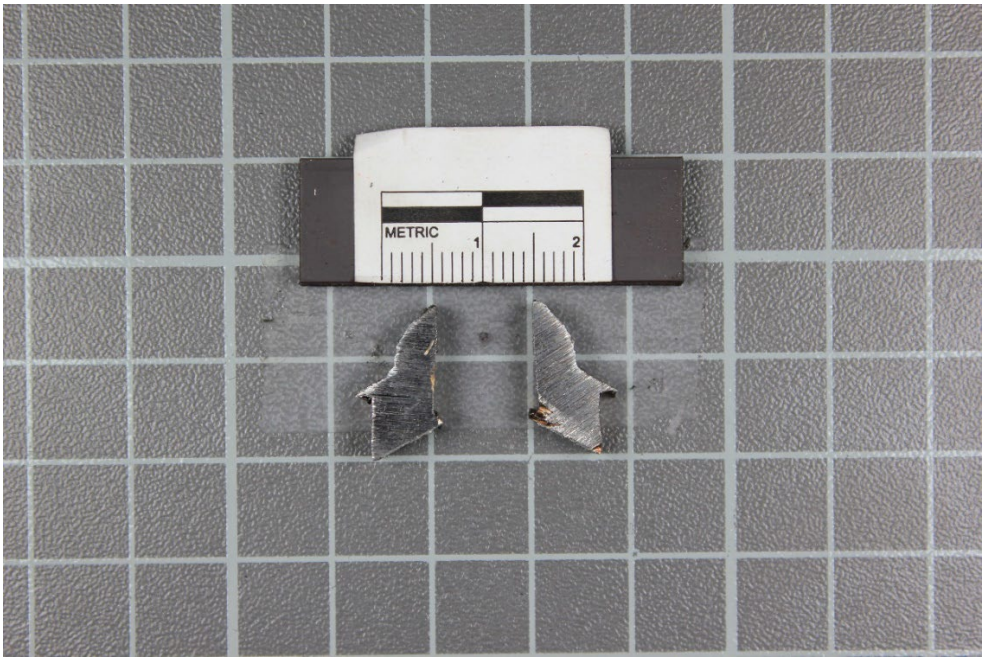

Figure 3.18: Profiles of the Weld Toe Flaw in Pole D

3.1.2 Pole Material Testing

Figure 3.19 shows the results of CVN testing for each individual HMIP, and Figure 3.20 provides a comparison of each HMIP with a solid sigmoid line fit to the data from all four HMIPs combined. The pole base metal exhibited an average lower shelf energy of 10 ft-lbf at -120 °F and an average upper shelf energy of 75 ft-lbf at 60 °F. Poles A and C closely matched the average, while Pole B was below the average and Pole D was above the average. While the impact energy

of the Pole B specimens was below the average of the four HMIPs, the impact toughness of Pole B was determined to be adequate.

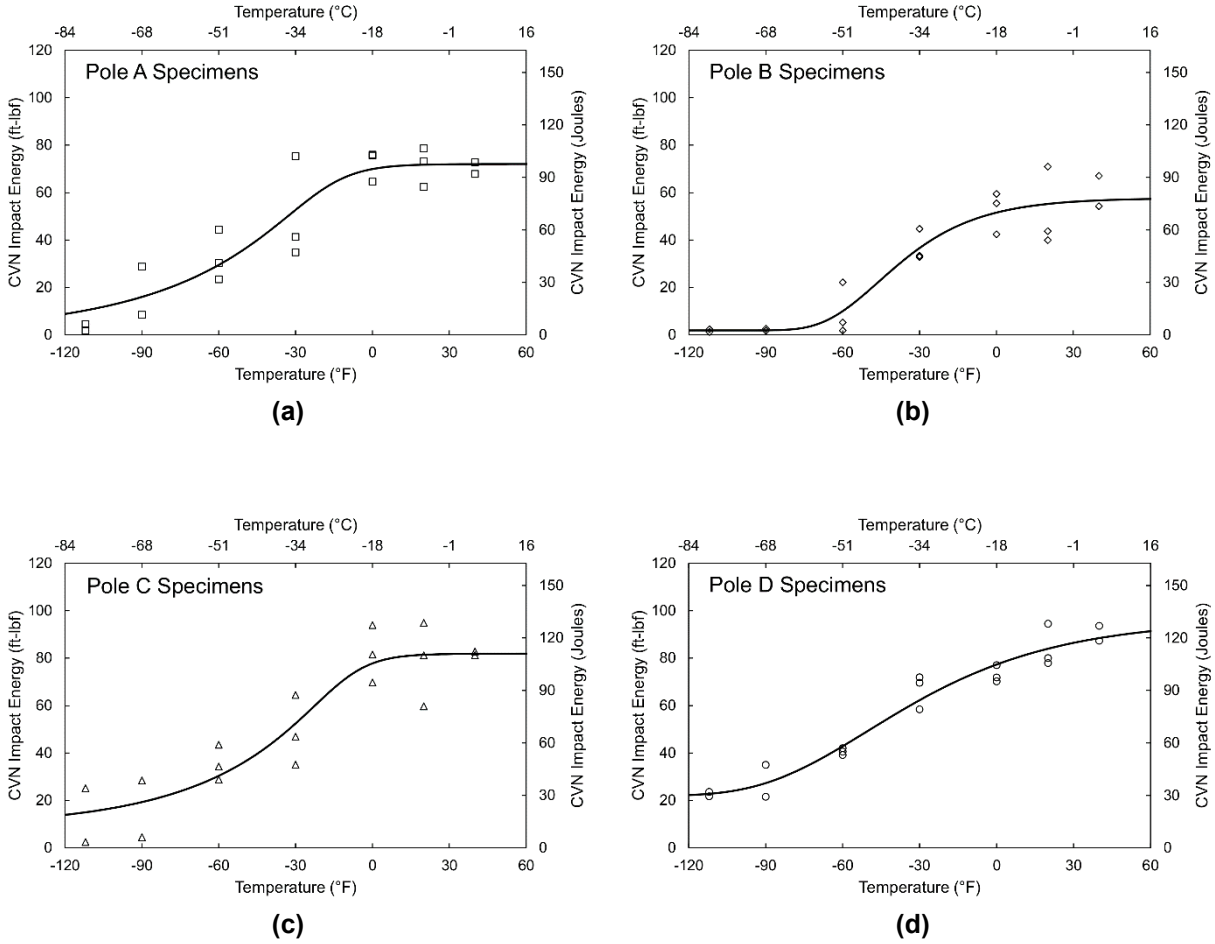

Figure 3.19: CVN Test Results for Base Metal from Each HMIP

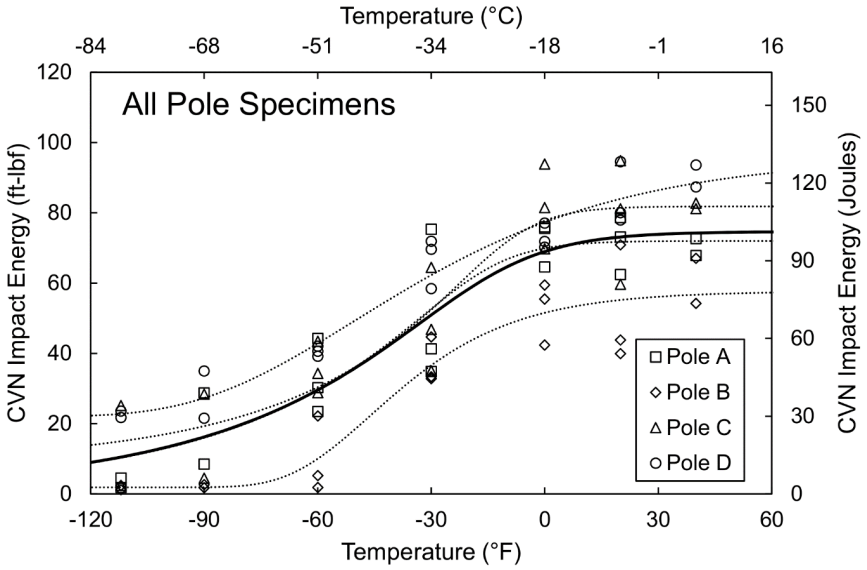

Figure 3.20: CVN Test Results for All HMIP Base Metals

3.1.3 Metallurgical Chemistry Analysis

The results of the metallurgical chemistry analysis from the base metal of each of the four HMIPs are presented in Table 3.1 along with the requirements for ASTM A572 (2018) Grade 50 steel.

Table 3.1: Metallurgical Chemistry Results

Element	Chemical Composition, %				
	Pole A	Pole B	Pole C	Pole D	A572 Gr. 50 Max
C	0.060	0.070	0.060	0.070	0.230
Mn	0.840	1.150	0.860	1.160	1.350
P	0.015	0.015	0.016	0.015	0.040
S	0.005	0.008	0.005	0.008	0.050
Si	0.030	0.040	0.030	0.040	0.400
Cu	0.110	0.170	0.100	0.170	-
Ni	0.060	0.060	0.050	0.060	-
Cr	0.080	0.050	0.080	0.060	-
Mo	0.010	0.010	0.010	0.010	-
V	0.000	0.000	0.000	0.000	-

The chemical analysis confirmed that each of the HMIP base metals conformed to the requirements of ASTM A572 Gr. 50. The carbon equivalencies of the four HMIP base metals calculated using Equation 2.2 were between 0.23 and 0.30. The carbon content and carbon equivalent of the four poles are plotted in 3.21, showing each pole classified as Zone 1.

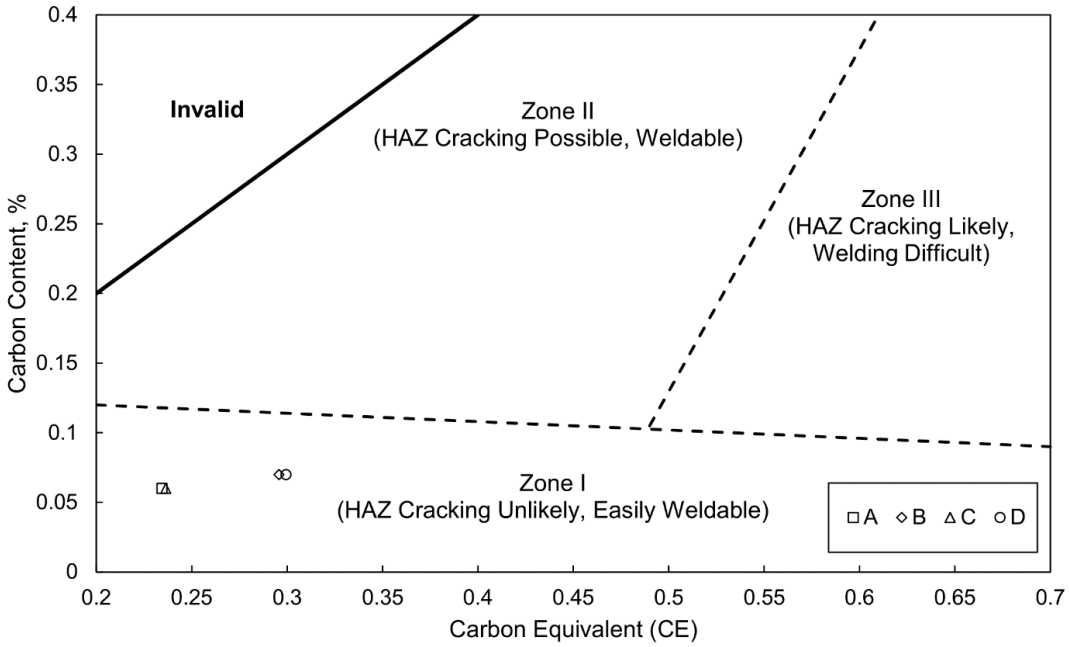

Figure 3.21: Carbon Contents and Equivalencies

3.2 Finite Element Modeling Results

The following sections detail the results of the finite element investigation. Section 3.2.1 presents the results of the parametric analysis to optimize pole geometries. Section 3.2.2 examines additional pole parameters that KDOT requested for analysis. Section 3.2.3 compares fatigue and "bomb cyclone" loads for the original HMIP design and for a pole with no reinforcing rim and a doubler plate. Lastly, Section 3.2.4 contains analysis of the newly proposed HMIP design.

3.2.1 Parametric Analyses and Optimizing Pole Geometries

3.2.1.1 Stress Contour Plots

The contour plots resulting from the parametric analyses are shown in Figure 3.22 to Figure 3.33. The stresses concentrated at the corners of the handhole, and the BP-Pole connection were the focus of these analyses. Figure 3.22 presents the analysis of handhole corner radius. Stresses around the handhole were observed to decrease as corner radius increased. There was little influence of handhole corner radius on stresses at the base plate weld.

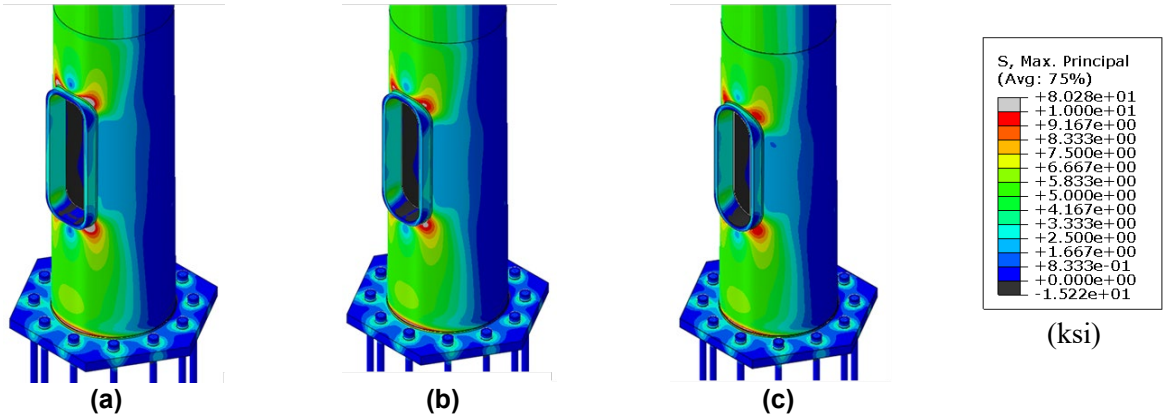

Figure 3.22: Maximum Principal Stress Contour Plots of Parametric Analysis of Handhole Corner Radius (a) 0.3W (4 in.), (b) 0.4W (5 in.), and (c) 0.5W (6 in.)

The contour plots for the analysis of the influence of handhole width are presented in Figure 3.23. Stresses at the handhole weld increased as handhole width increased, while there was little influence on stresses at the welded base plate connection.

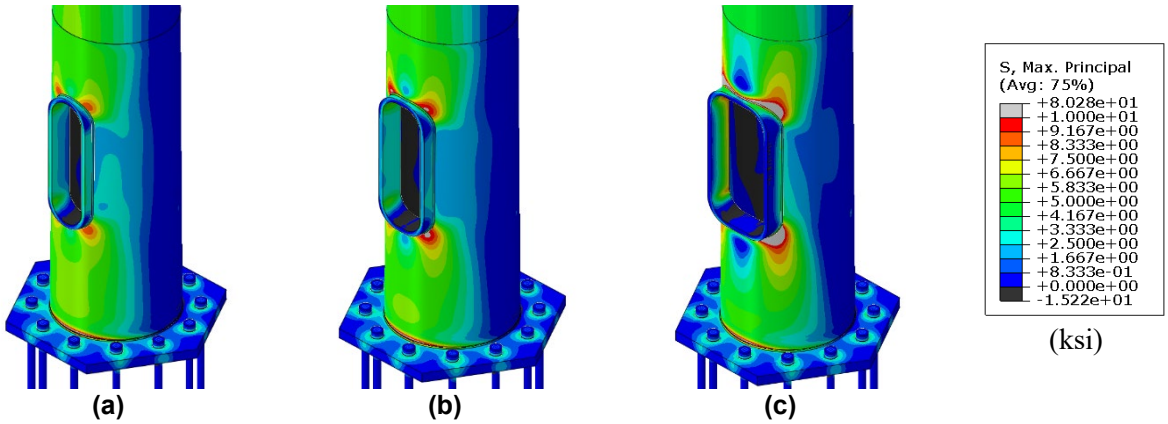

Figure 3.23: Maximum Principal Stress Contour Plots of Parametric Analysis of Handhole Width (a) 10 in., (b) 12 in., and (c) 16 in.

Contour plots showing the influence of handhole height are presented in Figure 3.24. Stresses around the handhole weld slightly increased as handhole height increased, but the change was not found to be significant. The influence of handhole height on stresses at the base plate weld was also found to be negligible.

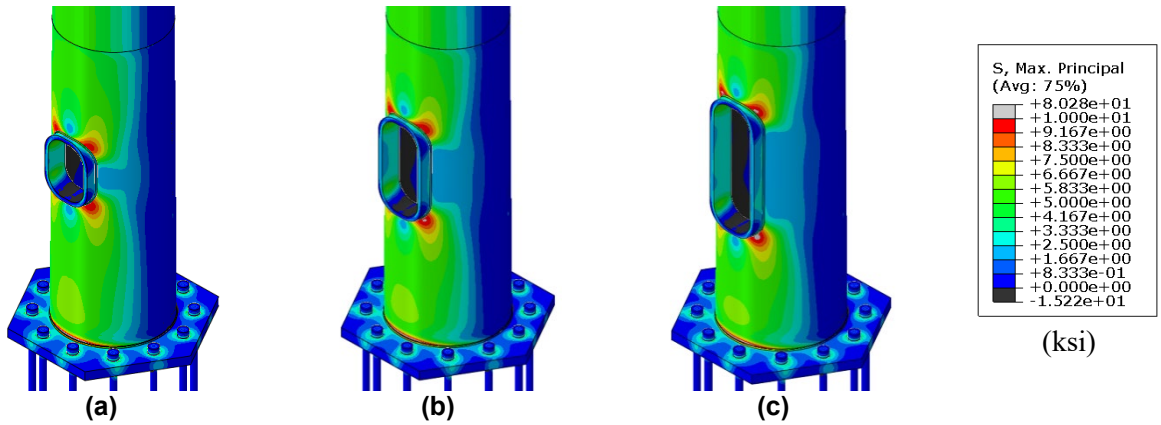

Figure 3.24: Maximum Principal Stress Contour Plots of Parametric Analysis of Handhole Height (a) 16 in., (b) 24 in., and (c) 32 in.

Figure 3.25 presents the contour plots showing the influence of handhole position relative to the bottom of the pole. Neither handhole stresses, nor base plate stresses were notably affected by the vertical position of the handhole.

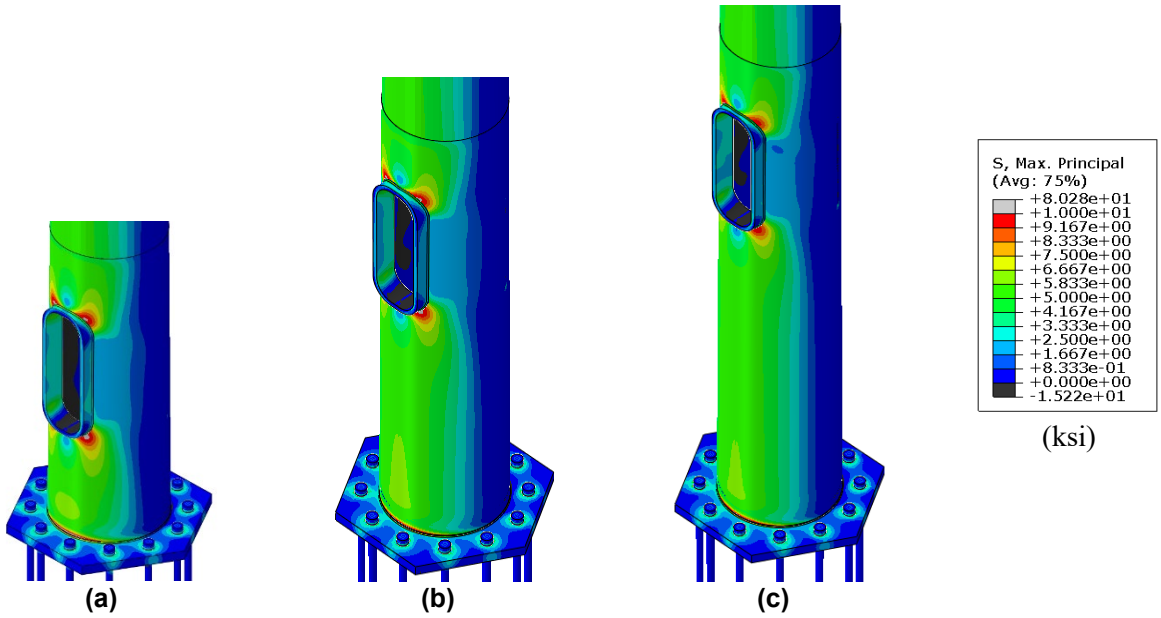

Figure 3.25: Maximum Principal Stress Contour Plots of Parametric Analysis of Handhole Position (a) 1.67D, (b) 3D, and (c) 4D away from Base Plate

Contour plots showing the influence of bolt pretension variations included in the study are presented in Figure 3.26. The influence of bolt pretension on stresses at the handhole and the base plate were not found to be significant. However, it should be noted that lack of pretension in the anchor bolts could produce other practical problems, such as fatigue failure of the anchorage, which would be expected to have a negative influence on stresses in the HMIP details.

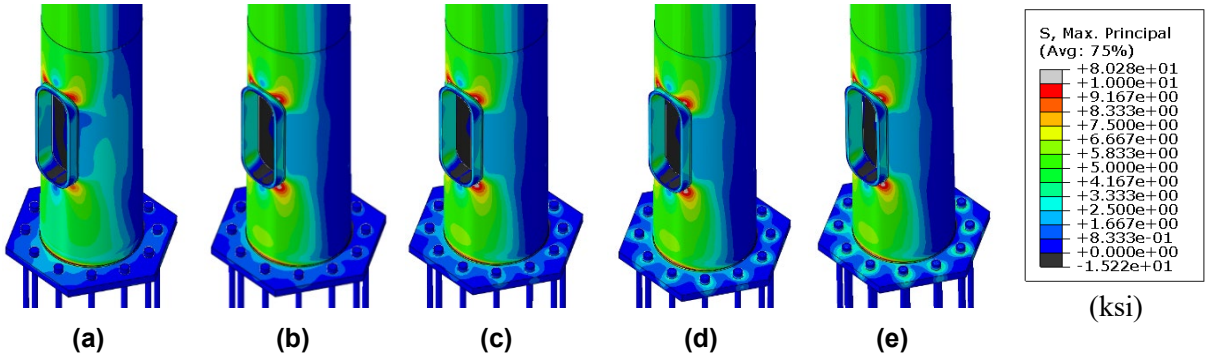

Figure 3.26: Maximum Principal Stress Contour Plots of Parametric Analysis of Bolt Pretension (a) 0%, (b) 25%, (c) 50%, (d) 75%, and (e) 100%

The contour plots for the different weld geometry variants at the handhole are presented in Figure 3.27. Stresses around the handhole were found to be greatest if only the fillet weld is used. The handhole stresses were lowest in the model that included a full penetration weld between the handhole reinforcing ring and the pole shaft.

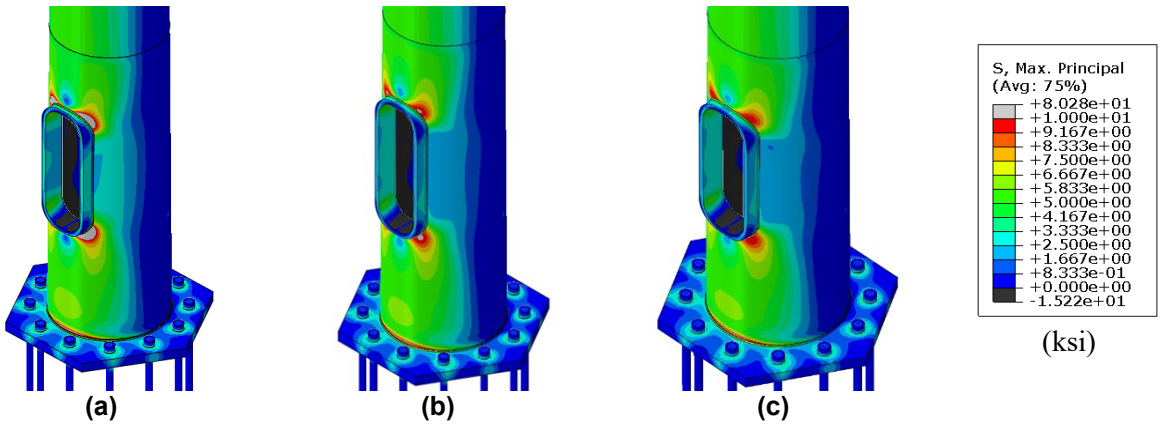

Figure 3.27: Maximum Principal Stress Contour Plots of Parametric Analysis of Weld Type Around Handhole (a) Fillet Weld, (b) Partial Penetration Weld with Fillet Weld, (c) Full Penetration Weld with Fillet Weld

The hot-spot stresses around the handhole in the partial penetration weld model and the full penetration weld model were not found to be significantly different. However, it is important to note that a hot-spot stress analysis is only able to indicate the likelihood of weld toe cracking (*not* weld root cracking). The partial penetration weld introduces a crack-like feature in the cross-section of the welded members at the root of the weld. The stress contour plots over the cross-section at the handhole details are presented in Figure 3.28. The full penetration weld corresponded with a significant stress reduction over the cross-section of the handhole detail.

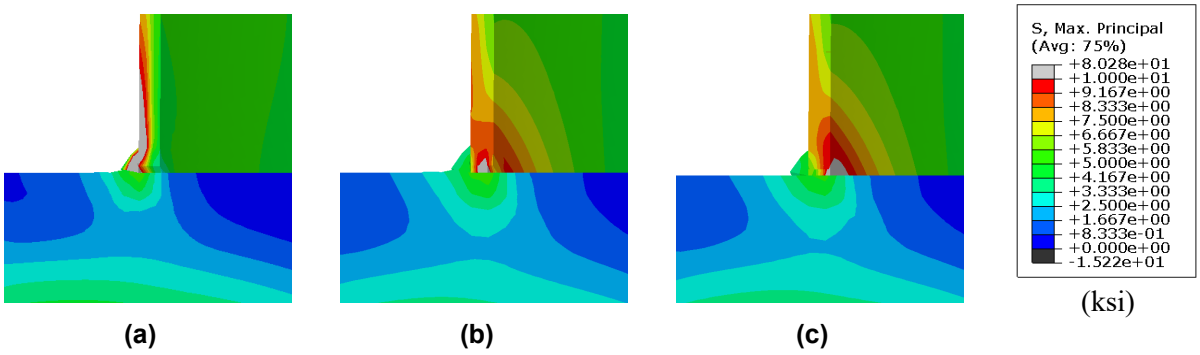

Figure 3.28: Maximum Principal Stress Contour Plots of Parametric Analysis of (a) Fillet Weld, (b) Partial Penetration Weld with Fillet Weld, (c) Full Penetration Weld with Fillet Weld Over Cross-Section of Handhole Detail

The influence of base plate thickness on stresses at the handhole was found to be negligible. Contour plots showing maximum principal stress at the base plate detail are presented in Figure 3.29. Stresses at the base plate decreased as base plate thickness increased. It should be noted that while this may seem an effective way of diminishing stresses due to fatigue loading at the base plate connection, it is not recommended to consider the influence of this variable only in these terms. Increasing base plate thickness relative to pole thickness corresponds with increased susceptibility to cracking during galvanizing, which can produce severe fatigue consequences in the field if undetected in the shop.

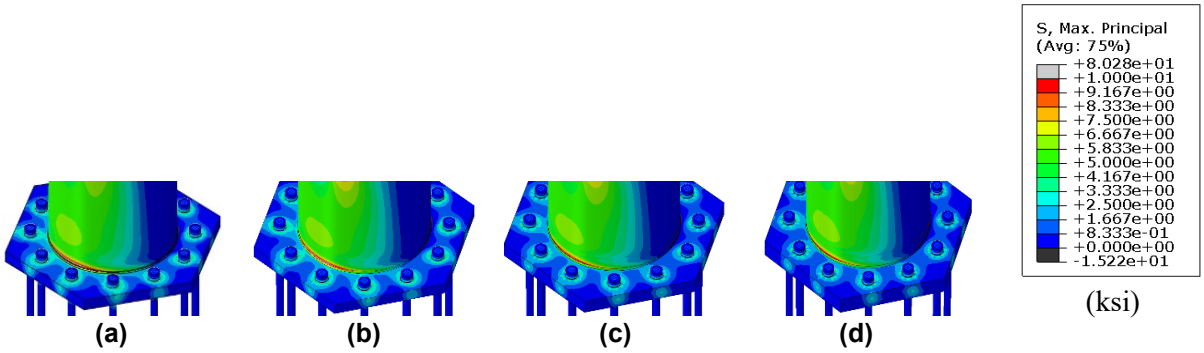

Figure 3.29: Maximum Principal Stress Contour Plots of Parametric Analysis of Base Plate Thickness (a) 2.25 in., (b) 2.5 in., (c) 3 in., and (d) 3.5 in.

Figure 3.30 presents the contour plots showing the influence of reinforcing rim thickness. Increasing thickness of the reinforcing rim tended to decrease stresses around the handhole. The

base plate stresses decreased with decreasing reinforcing rim thickness when the reinforcing rim was less than 0.50 in. thick. This phenomenon is also illustrated in Figure 3.37.

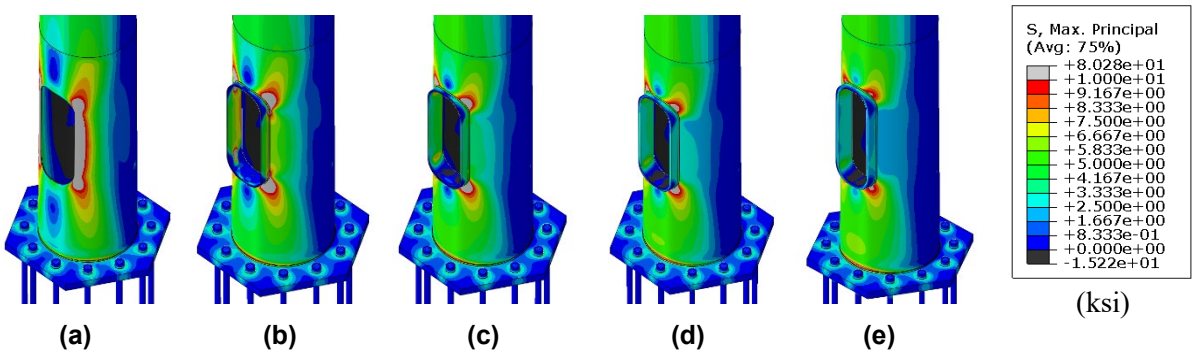

Figure 3.30: Maximum Principal Stress Contour Plots of Parametric Analysis of Reinforcing Rim Thickness (a) No Rim, (b) 0.25 in., (c) 0.5 in., (d) 0.75 in., and (e) 1 in.

Contour plots showing the influence of pole thickness are shown in Figure 3.31. Both handhole stresses and base plate stresses decreased significantly as pole thickness increased. Increasing the thickness of the pole shaft should be considered a valuable means for controlling fatigue stresses in HMIP, as it not only reduces stresses under fatigue loading, but it also can reduce the thermal mismatch between the base plate and pole during galvanizing—reducing the risk of cracking during galvanizing.

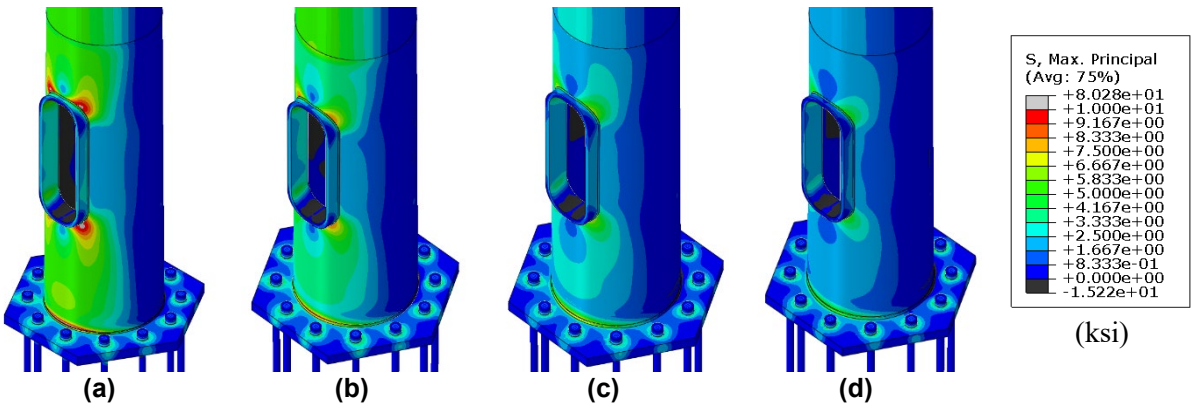

Figure 3.31: Maximum Principal Stress Contour Plots of Parametric Analysis of Pole Thickness (a) 0.25 in., (b) 0.5 in., (c) 0.625 in., and (d) 1 in.

The contour plots showing the influence of base plate hole diameter are presented in Figure 3.32. Stress at the base plate connection increased as the base plate hole size increased, but only for openings that were greater than 12 in. In other words, no noticeable change was observed between the case without an opening in the base plate and the case in which a 12-in. opening was present in the base plate.

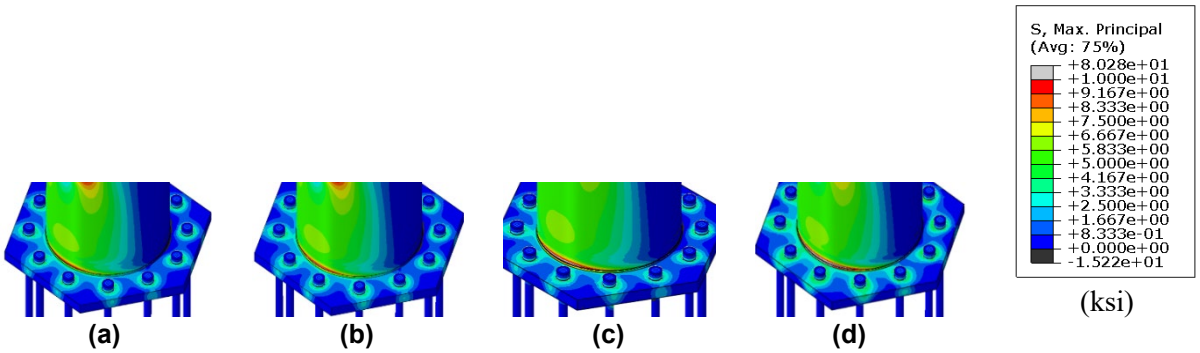

Figure 3.32: Maximum Principal Stress Contour Plots of Base Plate Hole Diameter (a) No Hole, (b) 12 in., (c) 17 in., (d) 22 in.

Based on the results of the parametric study, optimized geometries are shown in Table 3.2. The geometric parameters not listed in Table 3.2 were found to not impact hot-spot stresses at the handhole and base plate details, and thus were set to be the same as the original HMIP design in the optimized pole analysis.

Table 3.2: Optimized Pole Geometries

Parameter	Optimized Geometry
Handhole Corner Radius	5 in.
Handhole Width	10 in.
Base Plate Thickness	3.50 in.
Reinforcing Rim Thickness	1.00 in.
Pole Thickness	0.625 in.
Handhole Weld Geometry	Full Penetration with Fillet Weld
Base Plate Hole Diameter	12 in.

Figure 3.33 shows a contour plot of maximum principal stress for a pole that utilizes the optimized values listed in Table 3.2. The HMIP shown in Figure 3.33 was found to have the lowest handhole and base plate stresses among all the models analyzed in this study.

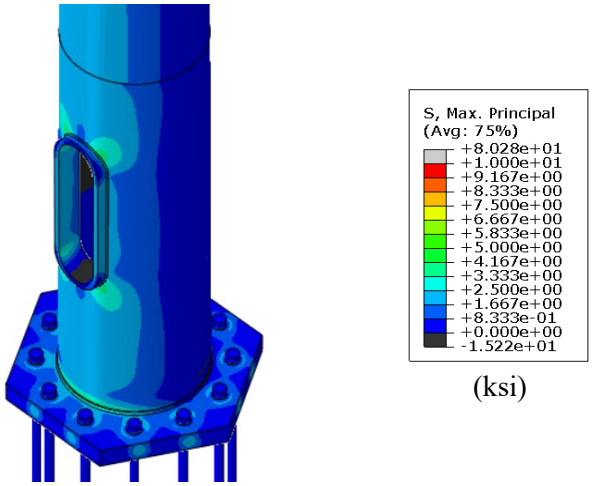

Figure 3.33: Maximum Principal Stress Contour Plots of Optimized Pole

3.2.1.2 Structural Hot-Spot Stress

The stresses along the node paths in the original pole model (Figure 2.14) are shown in Figure 3.34 as an example. After determining the location of the peak maximum principal stress (the hot-spot), stresses were extracted along the node paths shown in Figure 2.15. The structural hot-spot stress was obtained at a distance $0.1\sqrt{rt}$ away from the weld toe. In the original pole, this distance was 0.18 in. A linear interpolation was performed since a node at that distance was not available, as shown in Figure 3.35.

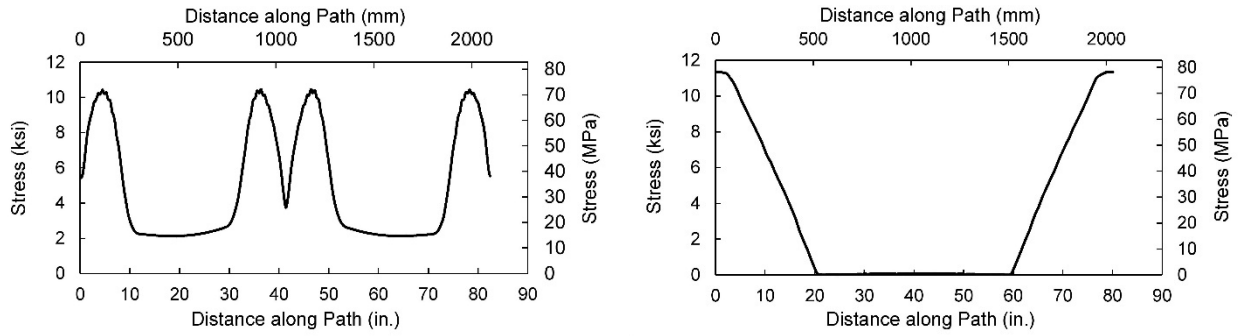

Figure 3.34: Maximum Principal Stresses Along Node Paths Around (a) Handhole and (b) Base Plate in Original Pole Model

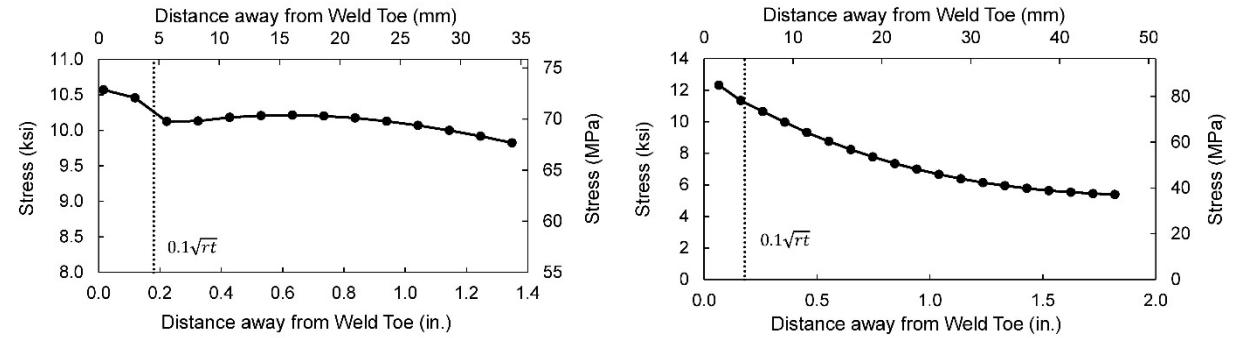

Figure 3.35: Maximum Principal Stresses Along Node Paths Perpendicular to Weld Toes at Hot-Spots of (a) Handhole and (b) Base Plate in Original Pole Model

3.2.1.3 Stress at the Handhole and Base Plate Details

The results of the parametric study and optimized pole analysis are presented in Figure 3.36 and Figure 3.37 in terms of extracted hot-spot stress. The vertical axis in the figures is the peak hot-spot stress obtained from each model and the horizontal axis represents the normalized magnitude of each parameter included in the study (the actual value of a parameter divided by the value of such parameter in the original pole). The structural hot-spot stresses determined for the handhole and the base plate details of the original pole were 10.3 ksi and 11.2 ksi, respectively.

The results of the parametric study indicate that using a thicker pole, a thicker reinforcing rim, full penetration weld, and smaller handhole width will reduce the peak hot-spot stress at the handhole detail, relative to the original baseline pole model. A thicker pole, thicker base plate, smaller reinforcing rim (thinner than 0.50 in.), and smaller base plate hole (negligible when the

hole diameter is smaller than 12 in.) tended to reduce the peak hot-spot stress at the base plate detail.

Using the overall optimized HMIP geometry described in Table 3.2, stresses at the handhole and base plate details can be further reduced an additional 33.7% and 33.2% respectively, as compared with the 0.625-in. pole in the parametric study.

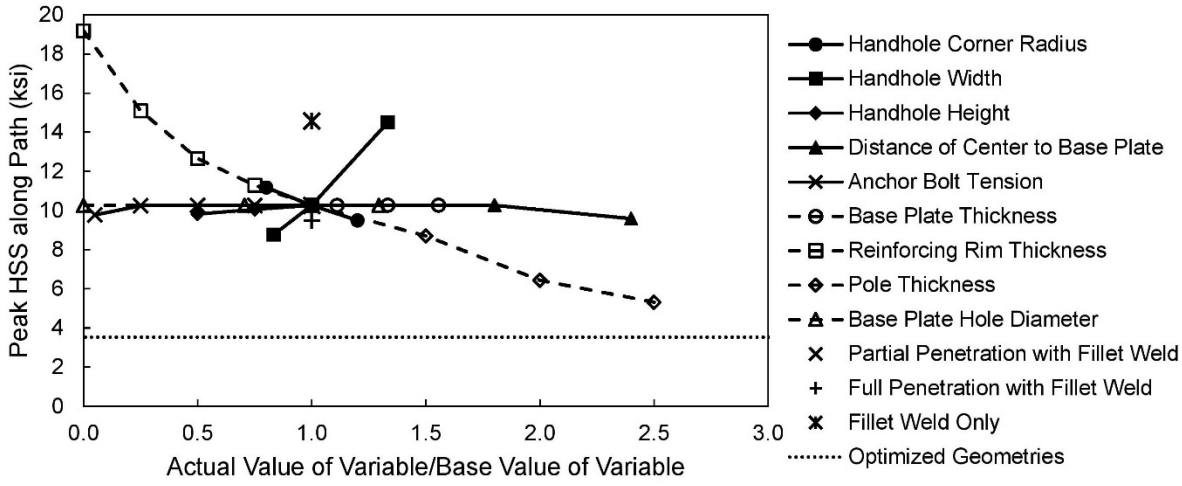

Figure 3.36: Peak Hot-Spot Stress of Handhole Detail in Parametric Study

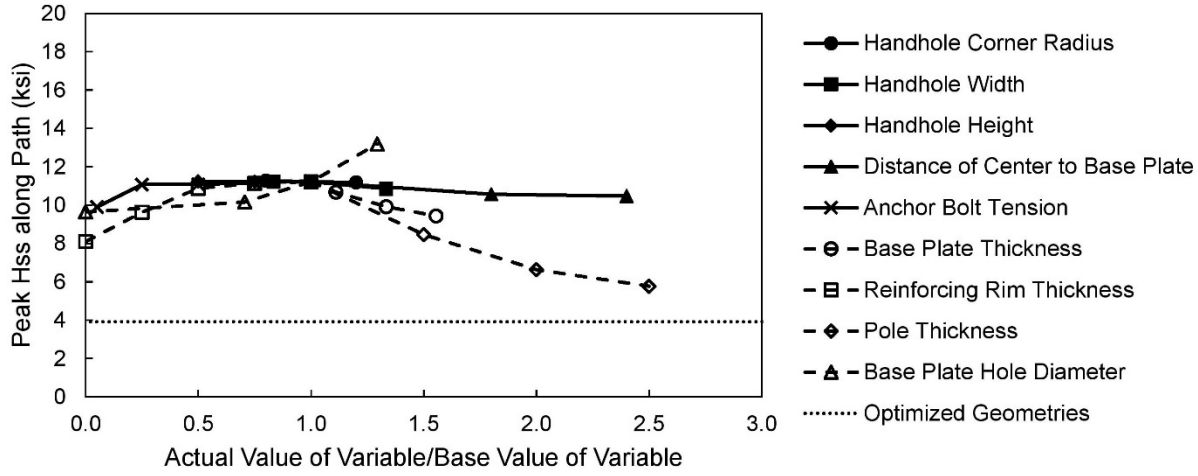

Figure 3.37: Peak Hot-Spot Stress of Base Plate Detail in Parametric Study

The optimized pole geometry is a theoretical proposal based on the findings of the parametric study, and it is recognized that the dimensions may not all be practical or economical

in practice. Although increasing pole thickness is the most effective way to reduce stresses at both details, making round poles with a thickness above 0.50 inch is not practical for many manufacturers. Multisided poles with a thickness of 0.625 in. are available, but the bends will increase the stress concentration and may make it more difficult to achieve good welding quality. The parametric study indicates that a thicker reinforcing rim can reduce the peak hot-spot stress at the handhole detail. However, from a practical perspective, it is difficult to achieve good welding quality if the difference in thickness of the reinforcing rim and the pole becomes too great. Moreover, according to the findings of the forensic study, the majority of observed cracking was found to be related to the lack of fusion at the root of the partial penetration weld. For these reasons, KDOT elected to use a 0.50-in.-thick round pole with a 1-in.-thick reinforcing rim in new HMIP designs. Additionally, they adopted a full penetration weld at the handhole reinforcing rim. The new KDOT HMIP design was also analyzed in this study and the results are presented in Section 3.2.4.

3.2.2 Additional Parameter Analysis

The analysis of pole thickness based on a pole without a reinforcing rim was performed to evaluate the possibility of eliminating the reinforcing rim altogether (and the associated need to weld around the handhole). The contour plots showing the results of these analyses are presented in Figure 3.38.

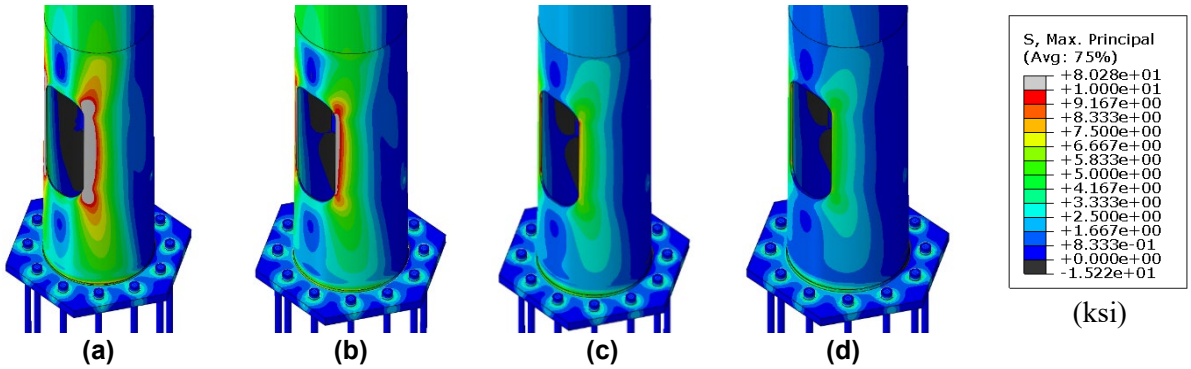

Figure 3.38: Contour Plots of Maximum Principal Stresses of Poles Without Reinforcing Rim of Pole Thickness (a) 0.25 in., (b) 0.375 in., (c) 0.5 in., and (d) 0.625 in.

Because poles without a reinforcing rim do not have welded handhole details, the peak maximum principal stresses around the handhole are presented in Figure 3.39. Stress at the handhole detail in the 0.625-in.-thick pole without a reinforcing rim was smaller than the structural hot-spot stresses of the original pole, which was a 0.25-in.-thick pole with a 1-in.-thick reinforcing rim. Moreover, removing the reinforcing rim decreased the structural hot-spot stresses at the base plate detail.

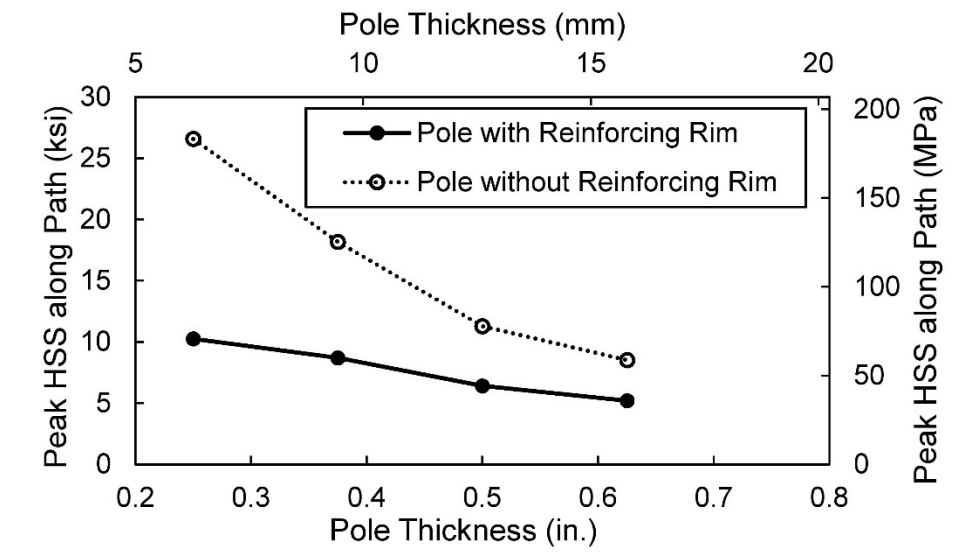

(a)

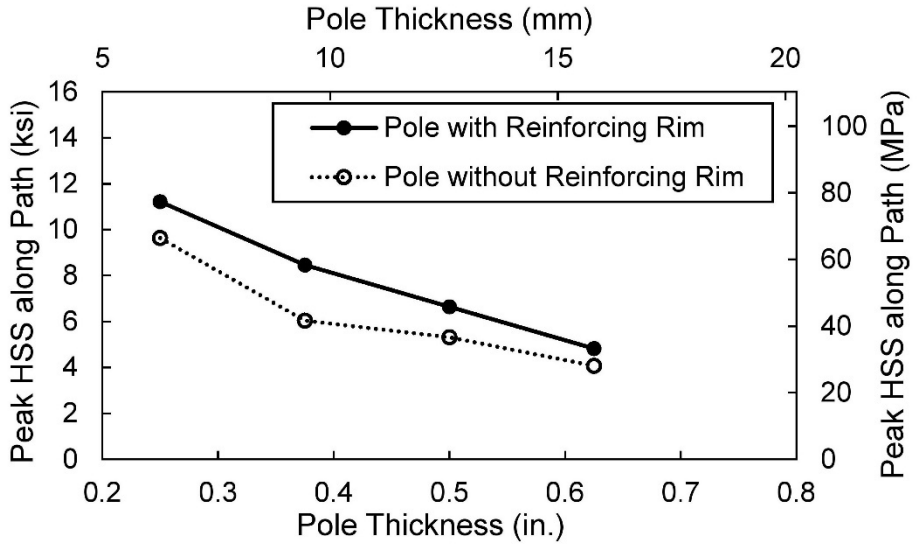

(b)

Figure 3.39: Influence of Pole Thickness on Stresses at (a) Handhole and (b) Base Plate Details

A different resistance curve should be adopted if welds are not used. AASHTO (2013) classifies unreinforced handholes to be Category A when calculated using the net section. Here the peak maximum principal stresses around the handhole in the models without the reinforcing rim are compared with the Category A S-N curve, as shown in Figure 3.40. Except for the 0.25-in.-thick pole, the other three thicker poles were all found to have stress demands below the constant amplitude fatigue threshold for AASHTO Category A (24 ksi). The analyses here indicate it is possible to have a thicker pole without a reinforcing rim such that the fatigue-prone handhole detail can be completely removed.

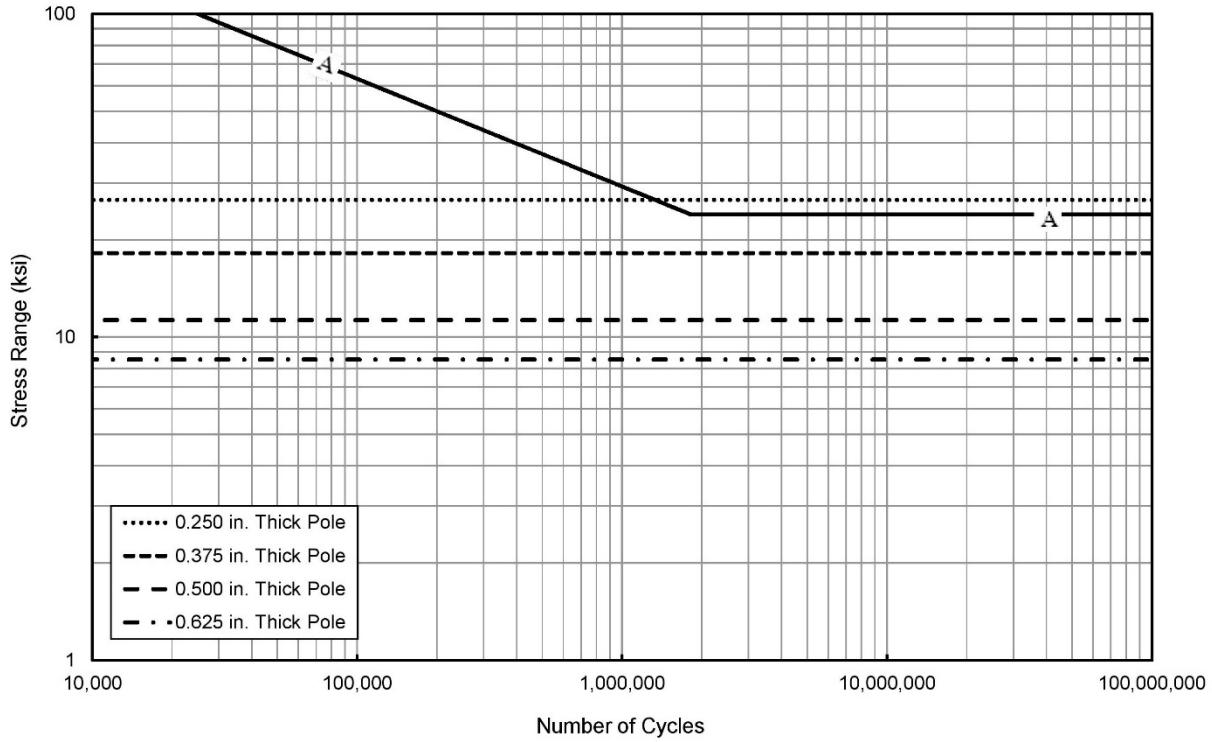

Figure 3.40: Peak Maximum Principal Stresses at Handhole Details of Models without Reinforcing Rim with AASHTO Category A Curve

The influence of base plate thickness on hot-spot stress demand at the base plate to pole connection is presented in Figure 3.41. As a reminder, a range of base plate thicknesses were considered, from 2.25 in. to 3.50 in. thick. Over this range, stresses in the 0.25-in.-thick pole and the 0.625-in.-thick pole decreased by 1.8 and 1.6 ksi, respectively, with increasing base plate

thickness. Therefore, increasing base plate thickness was similarly effective in reducing hot-spot stresses at the base plate detail in both pole thicknesses included in the study. Nonetheless, the reader is again cautioned against taking too simplistic of a view when considering increasing the base plate thickness to control fatigue stresses, as it may have unintended consequences that can increase susceptibility of the pole to cracking during galvanizing. In cases where small flaws develop during galvanizing and go undetected, premature fatigue cracking can be expected in the field.

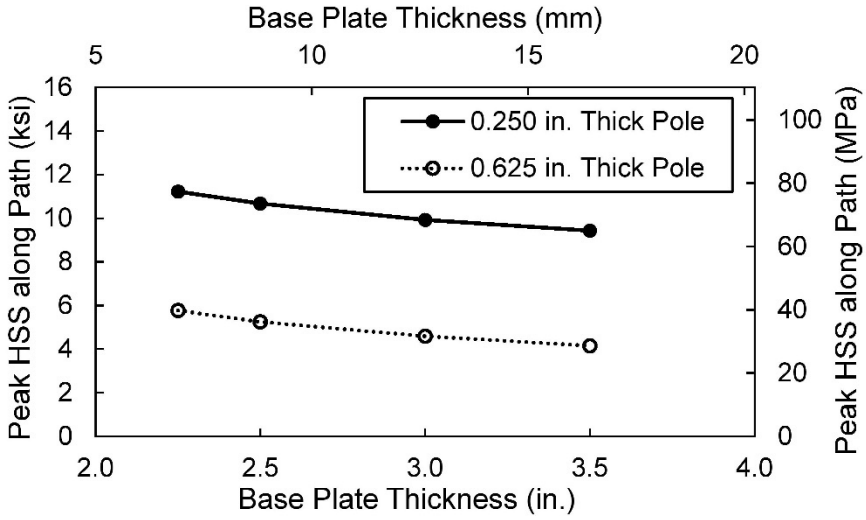

Figure 3.41: Influence of Base Plate Thickness on Structural Hot-Spot Stresses at Base Plate Detail

Figure 3.42 presents a plot showing peak structural hot-spot stress at the base plate detail as a function of the diameter of the opening in the base plate. Stresses decreased by 3.0 ksi and 2.2 ksi in the 0.25-in. and 0.625-in.-thick poles, respectively, when the hole diameter was reduced from 22 in. to 12 in. Making the base plate hole diameter smaller than 12 in. was not found to be beneficial in either of the poles studied.

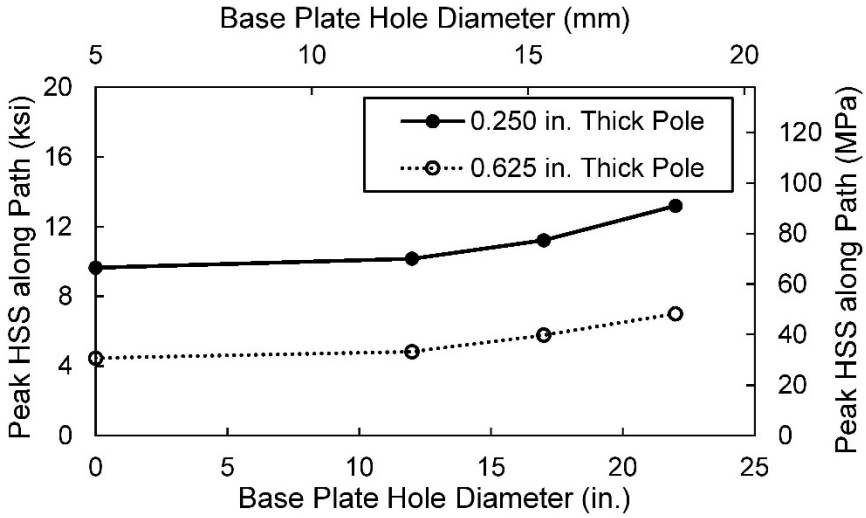

Figure 3.42: Influence of Base Plate Hole Diameter on Structural Hot-Spot Stresses at Base Plate Detail

The influence of the reinforcing rim thickness is presented in Figure 3.43, for the following cases:

1. A 0.25-in.-thick pole with a partial penetration weld at the handhole (the original baseline pole);
2. A 0.50-in.-thick pole with a full penetration weld at the handhole; and
3. A 0.625-in.-thick pole with a full penetration weld.

The stresses in the poles without reinforcing rims were obtained using the same node path as used for the poles with reinforcing rims. In the original pole, increasing the reinforcing rim thickness was found to be effective in reducing hot-spot stresses at the handhole detail. In the thicker poles with full penetration welds, the hot-spot stresses followed the same trend, but to a lesser magnitude than the original pole. This is because the change from partial to full penetration weld greatly decreased the overall hot-spot stress. When the reinforcing rim thickness decreased from 1 in. to 0.50 in., the peak hot-spot stress at the handhole detail increased by 2.4 ksi in the original pole, but only increased by 0.8 ksi and 0.5 ksi in the 0.50-in. and 0.625-in.-thick poles, respectively.

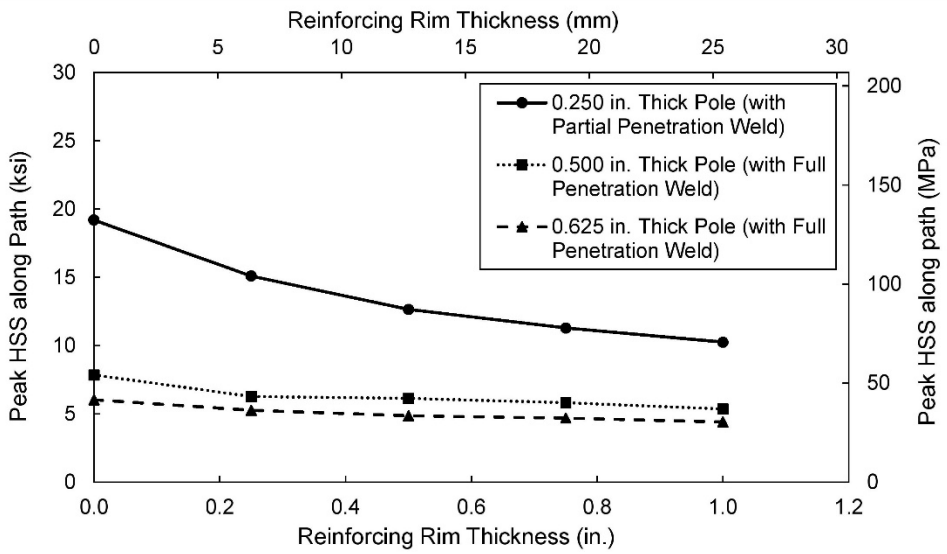

Figure 3.43: Influence of Reinforcing Rim Thickness on Structural Hot-Spot Stresses at Handhole Detail

3.2.3 Analysis of Original HMIP Design and Pole with Doubler Plate Handhole Detail under Fatigue Load and "Bomb Cyclone" Load

The hot-spot stress method was used to evaluate the susceptibility of the HMIP to fatigue damage under fatigue loading and loading that approximated the deformations observed to occur in the winter storm event ("bomb cyclone" loading). The stresses were obtained at a distance $0.1\sqrt{rt}$ away from the weld toes on the outer surface of the pole and compared with the resistance curves provided in existing literature. The stresses were extracted in the same way as introduced in Section 2.2.1. Strength-level design load was also applied and compared with the original design calculations provided by KDOT to verify the reliability of the model.

3.2.3.1 Fatigue Load

Contour plots showing stresses that developed under applied fatigue loading in the original pole and in the pole with doubler plate handhole details are presented in Figure 3.44. The peak stresses at the handhole and base plate details in the two models have similar magnitude. For the handhole details, the peak hot-spot in the original pole was found to occur at the corners of the handhole welds while the peak hot-spot stress in the doubler-plated pole occurred at the welds at the top and bottom of the doubler plate.

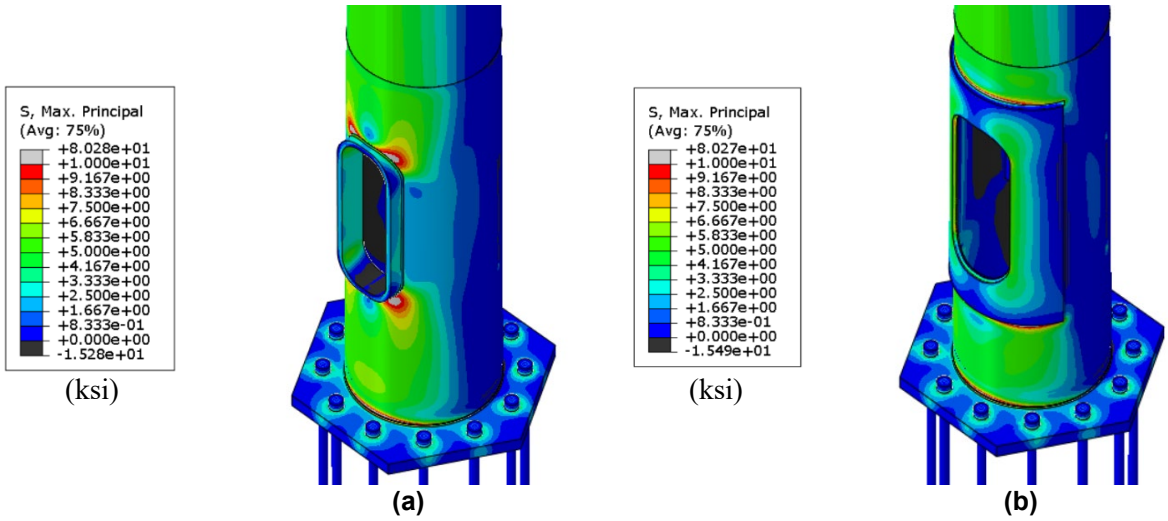

Figure 3.44: Maximum Principal Stress Contour Plots of (a) Original Pole and (b) Doubler Plate Pole under Fatigue Loading (Modeled Using C3D20R Element) (ksi)

Figure 3.45 presents the stresses along the node paths perpendicular to the welds at the hot-spots. (As a reminder, the stresses were 10.3 ksi and 12.9 ksi for handhole and base plate details in the original pole model.) Comparing with the stresses in the 8-node model, which are 10.3 ksi and 11.2 ksi for handhole detail and base plate detail, the structural hot-spot stress at the base plate in the 20-node model was 15% larger than the 8-node model but the stresses at the handhole detail did not differ. The peak structural hot-spot stresses at the handhole and base plate details in the doubler-plated pole model were found to be 13.7 ksi and 11.7 ksi.

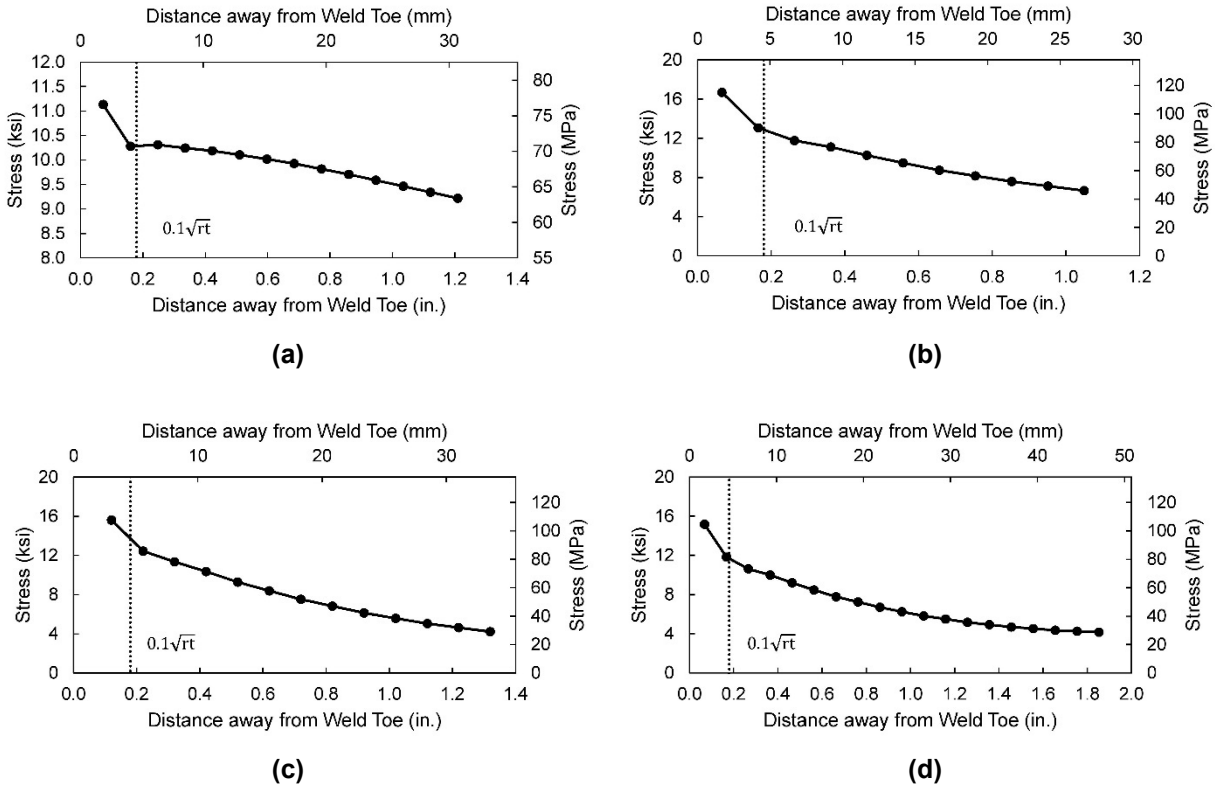

Figure 3.45: Stresses Away from Weld Toe at Hot-Spots of (a) Handhole Detail of Original Pole, (b) Base Plate Detail of Original Pole, (c) Handhole Detail of Doubler Plate Pole, and (d) Base Plate Detail of Doubler Plate Pole (Modeled Using C3D20R Element)

The peak structural hot-spot stresses are plotted with the AASHTO, DNV, and IIW resistance curves and presented in Figure 3.46. The computed stress demands were found to be slightly greater than the constant amplitude fatigue threshold of the AASHTO resistance curve. Notably, peak structural hot-spot stresses in the original pole and doubler plate pole models were found to be not much different from each other. The addition of the doubler plate to the handhole detail simply moved the location of the hot-spot to the doubler plate weld. Therefore, the welded doubler detail is not considered to be an effective method for extending the fatigue life of KDOT's existing poles.

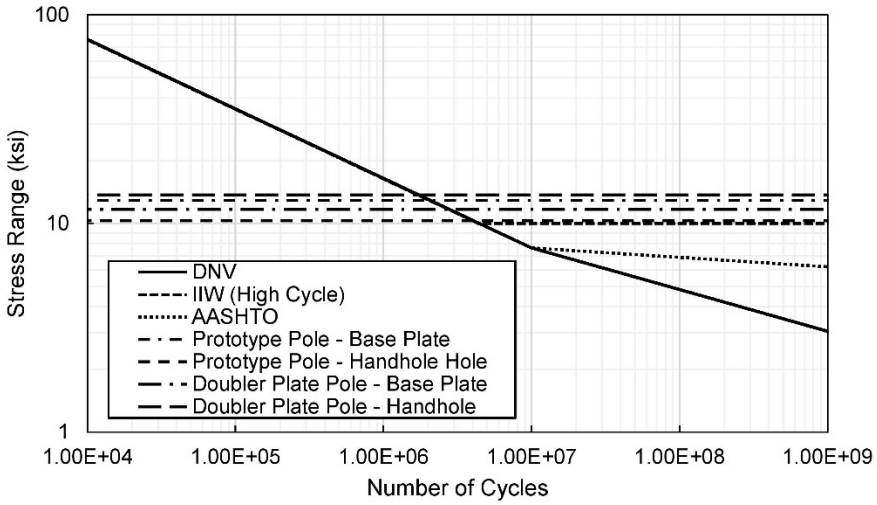

Figure 3.46: Structural Hot-Spot Stress of Original Pole and Doubler Plate Pole Under Fatigue Load (Modeled Using C3D20R Element)

3.2.3.2 “Bomb Cyclone” Load

Contour plots showing a comparison of stress demands between the original pole and the doubler plate pole under the “bomb cyclone” load are presented in Figure 3.47. Very large stresses were found to concentrate at the handhole and base plate details under this demanding loading scenario. The stresses were of similar magnitude in both cases, although the region of high stress was observed to be broader for the pole without the doubler plate retrofit.

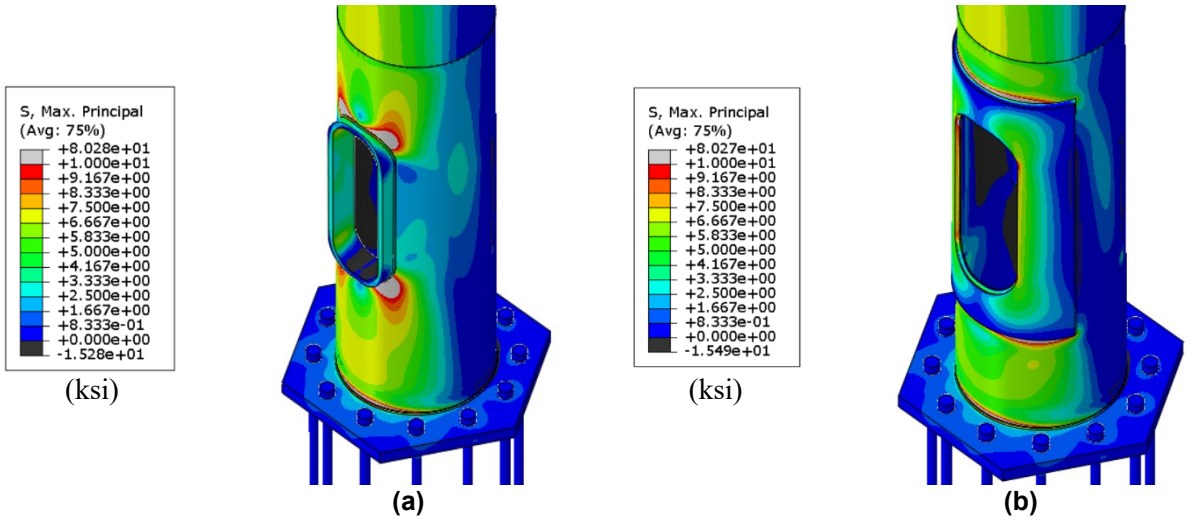

Figure 3.47: Maximum Principal Stress Contour Plots of (a) Original Pole and (b) Doubler Plate Pole Under "Bomb Cyclone" Loading (Modeled Using C3D20R Elements) (ksi)

Figure 3.48 presents the results with the S-N resistance curves. A reminder is offered that the material properties used in the models were linear-elastic, and some of the computed demands were found to be greater than the expected elastic limit of the material. For example, the computed hot-spot stresses for the handhole and base plate details in the original pole were 60.2 ksi and 66.3 ksi, respectively. For the doubler-plated pole, the stresses at the handhole and base plate details were found to be 84.5 ksi and 60.8 ksi. All these stresses are shown as 55 ksi in Figure 3.48 (yield strength of the material). The stresses computed as occurring under approximated "bomb cyclone" loading, therefore, were found to be much greater than the design fatigue strength of the pole. Cracking of the pole is inevitable if loaded under this stress level for a sustained period. The large oscillation phenomenon must be further studied to provide better information about how to prevent it.

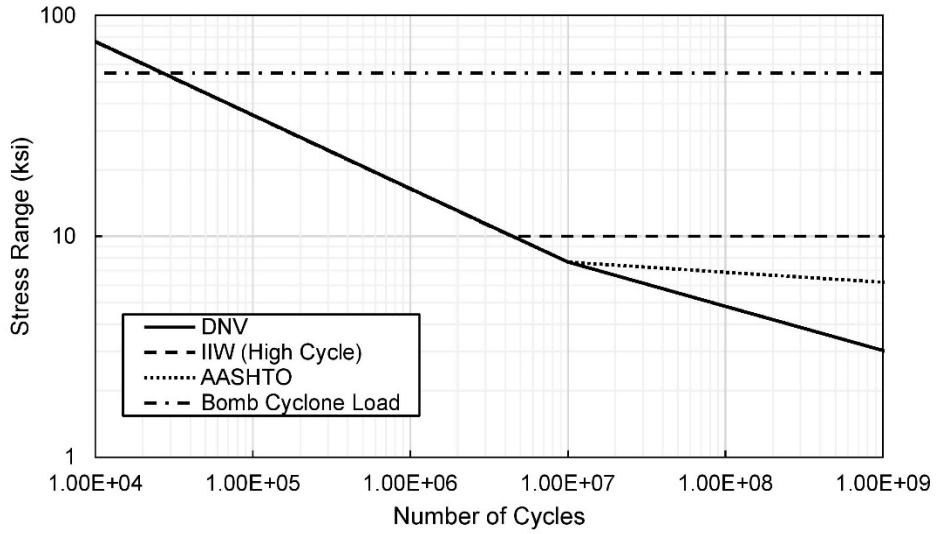

Figure 3.48: Structural Hot-Spot Stress of Original Pole and Doubler Plate Pole under "Bomb Cyclone" Load (Modeled Using C3D20R Elements)

3.2.4 Analysis of Kansas DOT New HMIP Design

Hot-spot stresses were extracted from the model of the new KDOT HMIP design, at a distance $0.1\sqrt{rt}$ from the weld toes on the outer surface of the pole, which equaled 0.25 in. for the 0.50-in.-thick pole. The stresses were obtained in the same way as introduced in Section 2.2.1. A contour plot showing the stress demands at the handhole and the base plate details is presented in Figure 3.49.

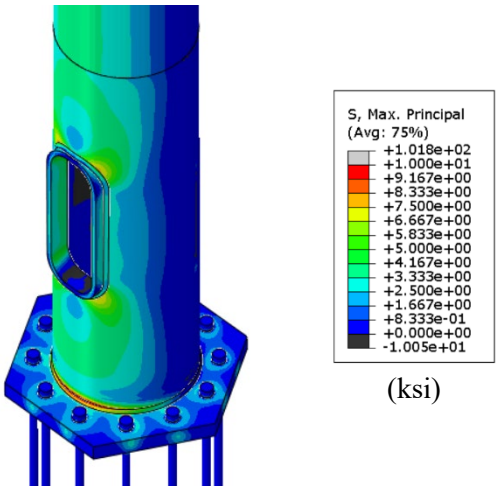

Figure 3.49: Maximum Principal Stresses Contour Plots of New KDOT HMIP Design (Modeled Using C3D20R Element)

Figure 3.50 presents the stress distribution perpendicular from the weld toes at the hot-spots of the handhole and the base plate details. The structural hot-spot stresses were 7.7 ksi at the handhole detail and 9.8 ksi at the base plate detail.

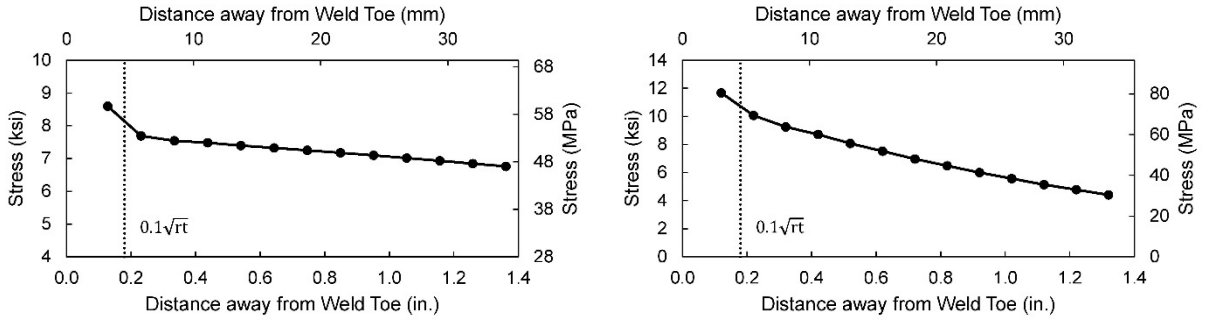

Figure 3.50: Stresses away from Weld Toes at the Hot-Spots of (a) Handhole and (b) Base Plate Details of New KDOT Design (Modeled Using C3D20R Element)

In the original pole model created using the 20-node quadratic solid elements (C3D20R) described in Section 3.2.3, the structural hot-spot stresses at the handhole and the base plate details were computed to be 10.3 ksi and 12.9 ksi, respectively. Considering that the new HMIP design is 20 ft taller than the original 100-ft-tall poles that were modeled, and has a luminaire with a larger EPA, the new KDOT HMIP design shows remarkable improvement at both the handhole and the base plate details. The structural hot-spot stresses computed for the original pole and the new KDOT pole are presented in Figure 3.51 with the three reference curves. The stress demands at the handhole and base plate details of the new pole design are below the constant amplitude fatigue threshold of the AASHTO resistance curve (10 ksi). The structural hot-spot stress of the base plate detail is only slightly smaller than the constant amplitude fatigue threshold. Reducing the base plate hole diameter may help further decrease the stress but could complicate making the full penetration weld at the reinforcing rim.

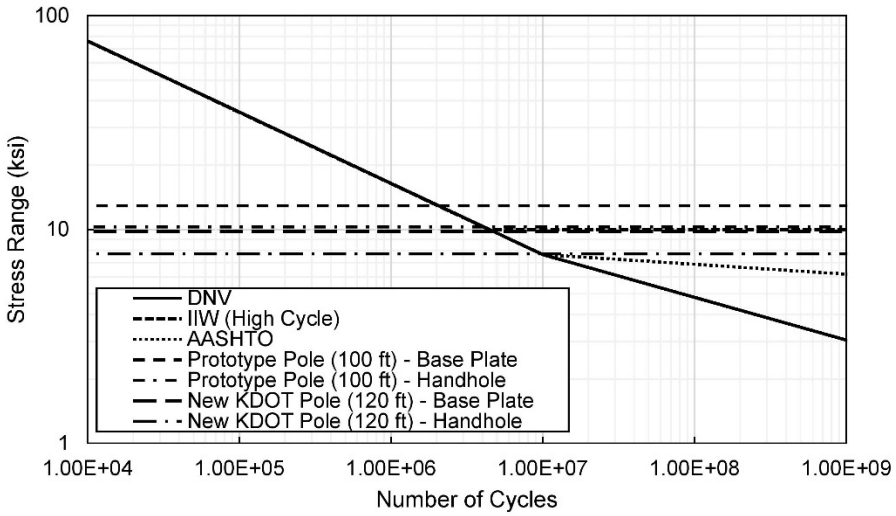

Figure 3.51: Structural Hot-Spot Stresses of Original Pole and New Kansas DOT Pole with Resistance Curves (Modeled Using C3D20R Element)

Chapter 4: Conclusions and Recommendations

This chapter summarizes conclusions made based on the results of this study, which included a physical forensics examination of four high mast illumination poles taken out-of-service, and a finite element investigation conducted to examine the influence of different geometric factors and loadings on the fatigue performance of HMIPs.

Section 4.1 focuses on conclusions drawn from the forensic investigation, Section 4.2 focuses on conclusions from the finite element modeling, and Section 4.3 provides recommendations for future work.

4.1 Conclusions Regarding the Forensic Investigation

Three of the four HMIPs received by the research team exhibited similar issues with the handhole weld that likely contributed to the cracking found after the extreme weather event in February 2019. The partial penetration welds at the handhole reinforcing rim in Poles A, B, and C all exhibited a lack of fusion on the interior of the weld that severely reduced the effective throat of the weld and embedded a flaw that increased the stress concentration. Porosity was also identified in the handhole reinforcing rim welds in Poles B and C. This can be difficult to detect in partial penetration welds, and likely contributed to a reduction of strength. Lastly, the reinforcing fillet weld at the top right side of the reinforcing rim in Pole A did not completely cover the groove of the pole, effectively increasing the sharpness of the weld toe and increasing the stress concentration.

To address these issues, it is recommended that the handhole weld be designed as a complete joint penetration weld. While more difficult to fabricate, a full penetration weld will eliminate any crack-like features from lack of fusion on the interior of the pole. The additional requirement of grinding to sound metal on the exterior of the pole before welding will help reduce the likelihood of porosity in the weld.

Regarding the impact toughness and metallurgical chemistry of the pole base metals, each of the four poles was found to have adequate toughness and to conform to ASTM A572 (2018) standards. For this reason, changing of the pole material is not recommended for future designs.

4.2 Conclusions Regarding the Finite Element Analyses

A series of finite element analyses were performed to study the fatigue performance of the handhole and base plate details in high mast illumination poles, including:

1. A parametric study in which hand hole and base plate geometries were varied;
2. Several parametric analyses for different pole geometries;
3. A comparison of the original pole design against a pole design that included a handhole detail retrofitted with a welded doubler plate, both loaded first under fatigue loading and then under a loading estimated from a video recorded during a "bomb cyclone" winter weather event, and
4. An analysis of a new HMIP design proposed by KDOT under design-level fatigue loading.

The models in (1) and (2) were created using the 3D linear 8-node solid elements with reduced integration (C3D8R), and the models in (3) and (4) were created using 3D quadratic 20-node solid elements (C3D20R) to meet the requirement of AASHTO for structural hot-spot stress analysis. The conclusions are summarized as follows:

- From the parametric analyses, the following actions can be expected to reduce structural hot-spot stresses at the handhole detail: thickening the pole, thickening the handhole reinforcing rim, utilizing full penetration welding, and utilizing smaller handhole widths.
- From the parametric analyses, the following actions can be expected to reduce structural hot-spot stresses at the base plate detail: Using a thicker pole, using a thicker base plate, using a thinner reinforcing rim (thinner than 0.50 in.), and using a smaller-diameter base plate hole (negligible when the hole diameter is smaller than 12 in.).
- Under AASHTO fatigue loads, the maximum principal stresses at the handhole details in the 0.375-in., 0.50-in., and 0.625-in.-thick poles without reinforcing rims were all below the constant amplitude fatigue

threshold for the AASHTO Category A curve. This finding suggests it is possible to use a thicker pole without a reinforcing rim to eliminate the welded connection at the handhole detail.

- Increasing base plate thickness and decreasing base plate hole diameter (when the hole diameter was larger than 12 in.) reduced stress demands at the base plate detail in both the thinner and the thicker poles.
- When the original HMIP design was subjected to AASHTO design-level fatigue loads, the structural hot-spot stresses at the handhole and base plate details were found to be slightly above the constant amplitude fatigue threshold of the AASHTO resistance curve.
- Stress demands for the welded doubler-plate handhole details had a similar magnitude as for unretrofitted HMIPs with a reinforcing rim detail. Replacing the welded handhole rim with a welded doubler plate only moved the hot-spot to the new weld location.
- The stress magnitudes that corresponded with the large-oscillation phenomenon observed in a 2019 winter storm were much larger than the design stresses for the HMIP. Cracking of an HMIP is inevitable should the pole oscillate under such a stress level for a sustained period. The large-amplitude oscillation phenomenon needs to be further studied to provide definitive information regarding how to prevent it.
- The structural hot-spot stresses computed at the handhole and the base plate details for the new KDOT HMIP design were below the constant amplitude fatigue threshold of the AASHTO fatigue resistance curve. Considering the new HMIP design is 20 ft taller than the original pole, and has luminaires with a larger EPA, the improvement of the new design is remarkable. Reducing the base plate hole diameter can help to further decrease the structural hot-spot stress at the base plate detail.

4.3 Future Work

As mentioned in previous sections, the large-amplitude oscillation effects that were present during the “bomb cyclone” event must be studied further to determine the most effective methods for mitigating such phenomena. A possible solution could be to design dampers for the HMIPs that reduce the magnitude of deflection and stresses. Another avenue for future work is to consider the fluid dynamics behavior that produces such a response in high mast illumination poles. One possible dynamic effect is known as “vortex shedding” and occurs when the air passing past a body creates oscillating low-pressure zones, causing vibrations perpendicular to the direction of airflow. If this occurs near the natural vibration frequency of the structure, the compounding vibration can result in very large deformations and stresses. Lastly, physical testing of different welding methods and material thicknesses could be performed to determine the relative ease and effectiveness of a variety of handhole details.

References

American Association of State Highway and Transportation Officials (AASHTO). (2013). *Standard specifications for structural supports for highway signs, luminaires, and traffic signals* (6th ed.).

American Association of State Highway and Transportation Officials (AASHTO). (2017). *AASHTO LRFD bridge design specifications* (8th ed.).

American Galvanizers Association (AGA). (2009). *Welding & hot-dip galvanizing*. https://galvanizeit.org/education-and-resources/publications/welding-hot-dip-galvanizing-2002

American Welding Society (AWS). (2015). *Structural welding code – Steel* (AWS Standard D1.1/D1.1M:2015).

ASTM A572/A572M-18. (2018). *Standard specification for high-strength low-alloy columbium-vanadium structural steel*. ASTM International. doi: 10.1520/A0572_A0572M-18, www.astm.org

ASTM E23-16. (2016). *Standard test methods for notched bar impact testing of metallic materials*. ASTM International. doi: 10.1520/E0023-16, www.astm.org

Bennett, C., Li, J., & Matamoros, A. (2021). *Mitigation of weldment cracking in steel highway structures due to the galvanizing process* (NCHRP Research Report 965). Transportation Research Board.

Connor, R. J., Collicott, S. H., DeSchepper, A. M., Sherman, R. J., & Ocampo, J. A. (2012). *Fatigue loading and design methodology for high-mast lighting towers* (NCHRP Report 718). Transportation Research Board.

DNV. (2011). *Fatigue design of offshore steel structures* (Recommended practice DNV-RP-C203).

Dowling, N. E. (1999). *Mechanical behavior of materials: Engineering methods for deformation, fracture, and fatigue* (2nd ed.). Prentice Hall.

Foley, C. M., Fournelle, R. A., Ginal, S. J., & Peronto, J. L. (2004). *Structural analysis of sign bridge structures and luminaire supports* (Report No. 04-03). Wisconsin Department of Transportation.

Goyal, R., Dhonde, H. B., & Dawood, M. (2012). *Fatigue failure and cracking in high mast poles* (Report No. FHWA/TX-12/0-6650-1). University of Houston.

Hobbacher, A. (2008). *Recommendations for fatigue design of welded joints and components* (IIW doc. XIII-2151r4-07/XV-1254r4-07). International Institute of Welding.

Kleineck, J. R. (2011). *Galvanizing crack formation at base plate to shaft welds of high mast illumination poles* (Master's thesis). The University of Texas at Austin.

Lucon, E., McCowan, C. N., & Santoyo, R. L. (2016). Overview of NIST activities on subsize and miniaturized Charpy specimens: Correlations with full-size specimens and verification specimens for small-scale pendulum machines. *ASME Journal of Pressure Vessel Technology, 138*(3). https://doi.org/10.1115/1.4032474

Nasouri, R., Nguyen, K., Montoya, A., Matamoros, A., Bennett, C., & Li, J. (2019a). Simulating the hot dip galvanizing process of high mast illumination poles. Part I: Finite element model development. *Journal of Constructional Steel Research, 162*, 105705.

Nasouri, R., Nguyen, K., Montoya, A., Matamoros, A., Bennett, C., & Li, J. (2019b). Simulating the hot dip galvanizing process of high mast illumination poles. Part II: Effects of geometrical properties and galvanizing practices. *Journal of Constructional Steel Research, 159*, 584–597.

Niemi, E., Fricke, W., & Maddox, S. (2018). *Structural hot-spot stress approach to fatigue analysis of welded components: Designer's guide* (2nd ed.). Springer.

Ocel, J. M. (2014). *Fatigue testing of galvanized and ungalvanized socket connections* (Report No. FHWA-HRT-14-066). Federal Highway Administration.

Pool, C. S. (2010). *Effect of galvanization on the fatigue strength of high mast illumination poles* (Master's thesis). The University of Texas at Austin.

Roy, S., Park, Y. C., Sause, R., Fisher, J. W., & Kaufmann, E. J. (2011). *Cost-effective connection details for highway sign, luminaire, and traffic signal structures* (NCHRP Web-Only Document 176). Transportation Research Board.

Wallin, K., Karjalainen-Roikonen, P., & Suikkanen, P. (2016). Sub-sized CVN specimen conversion methodology. *Procedia Structural Integrity, 2*, 3735–3742.

Appendix A

A.1 Pole A Crack Images

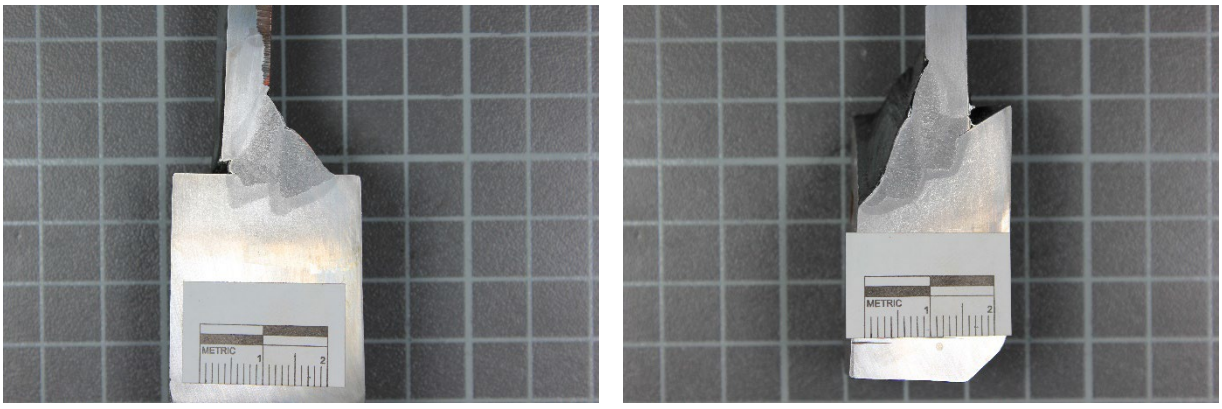

(a) (b)

Figure A.1: (a) Left Side of A-2-1, (b) Right Side of A-2-1

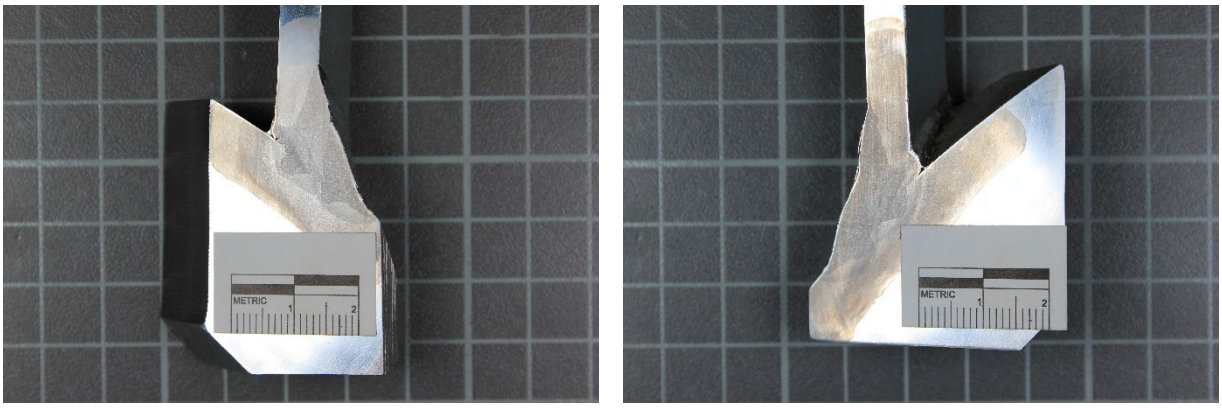

(a) (b)

Figure A.2: (a) Left Side of A-2-2, (b) Right Side of A-2-2

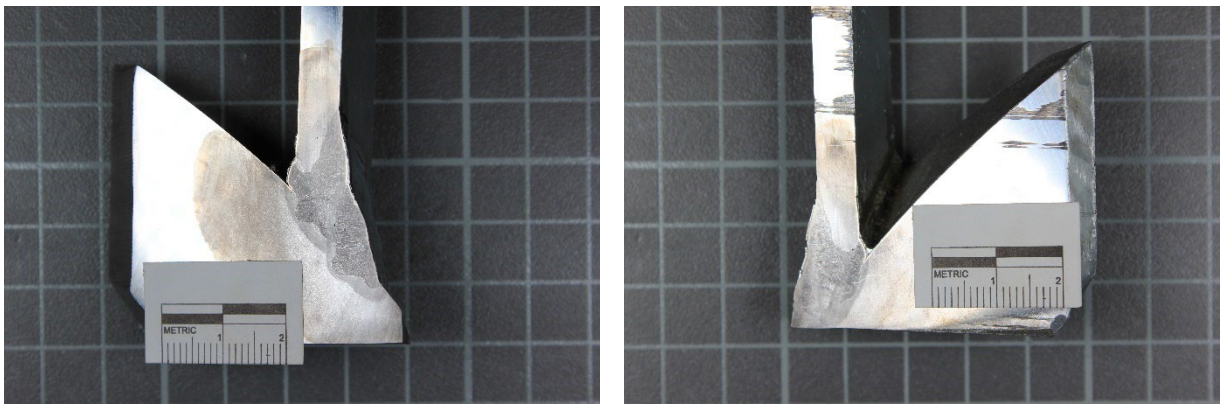

(a) (b)

Figure A.3: (a) Left Side of A-2-3, (b) Right Side of A-2-3

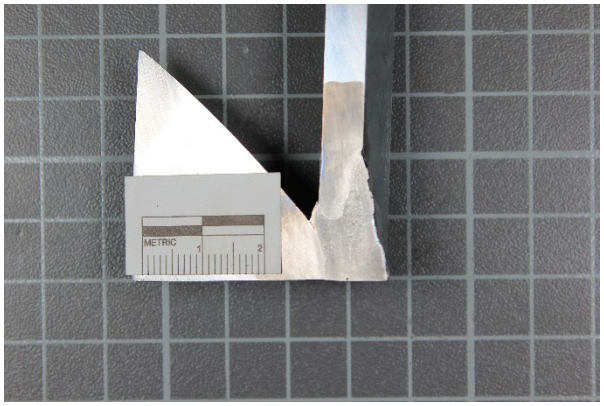

Figure A.4: Left side of A-2-4

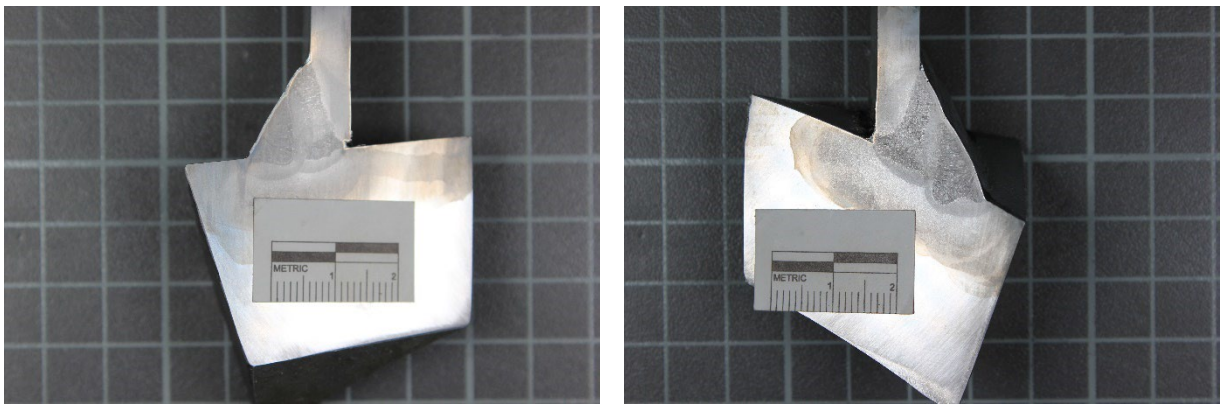

(a) (b)

Figure A.5: (a) Left Side of A-3-1, (b) Right Side of A-3-1

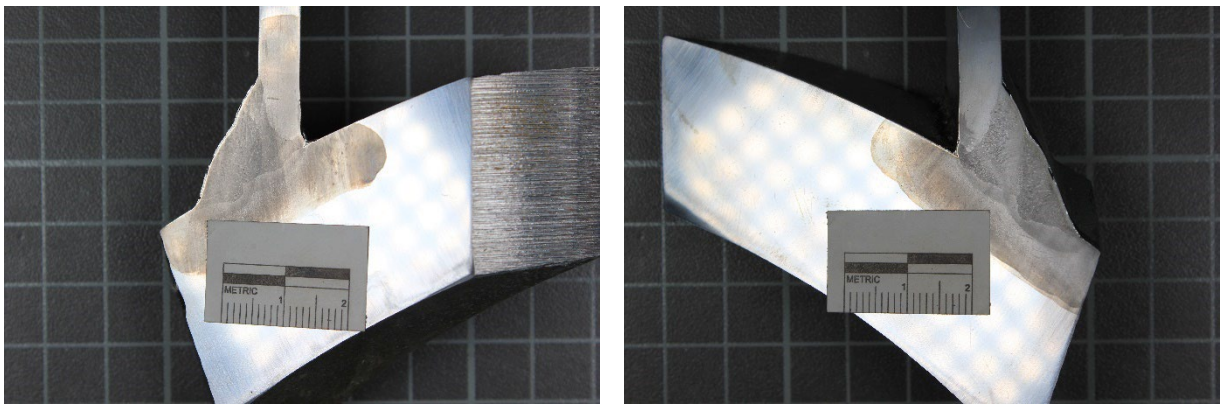

(a) (b)

Figure A.6: (a) Left Side of A-3-2, (b) Right Side of A-3-2

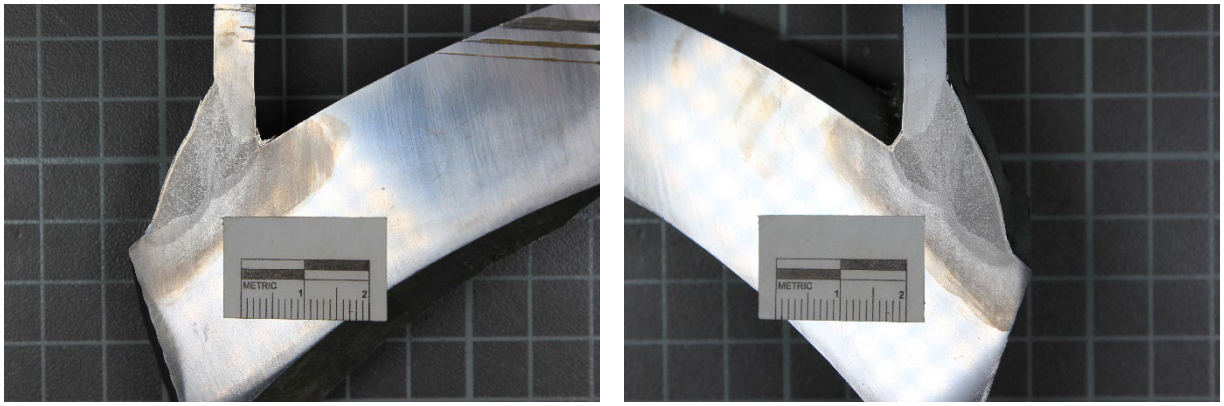

(a) (b)

Figure A.7: (a) Left Side of A-3-3, (b) Right Side of A-3-3

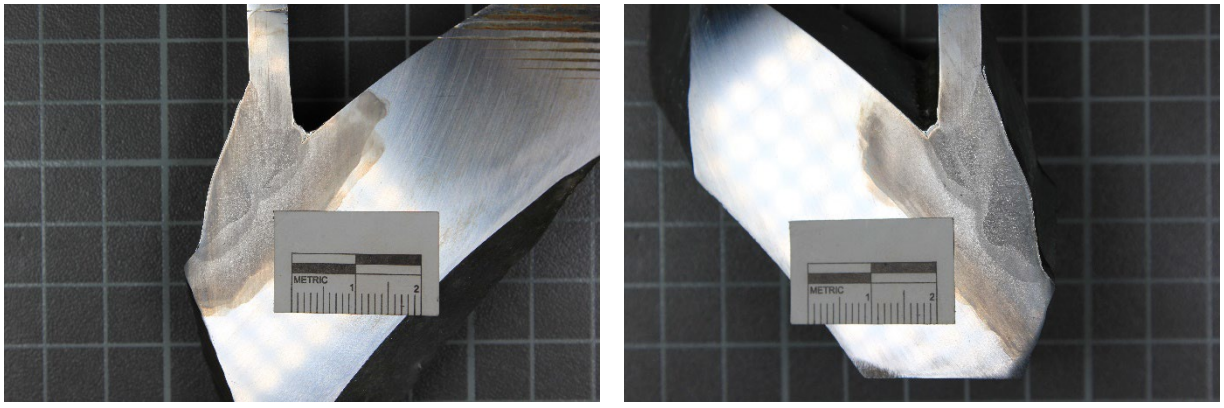

(a) (b)

Figure A.8: (a) Left Side of A-3-4, (b) Right Side of A-3-4

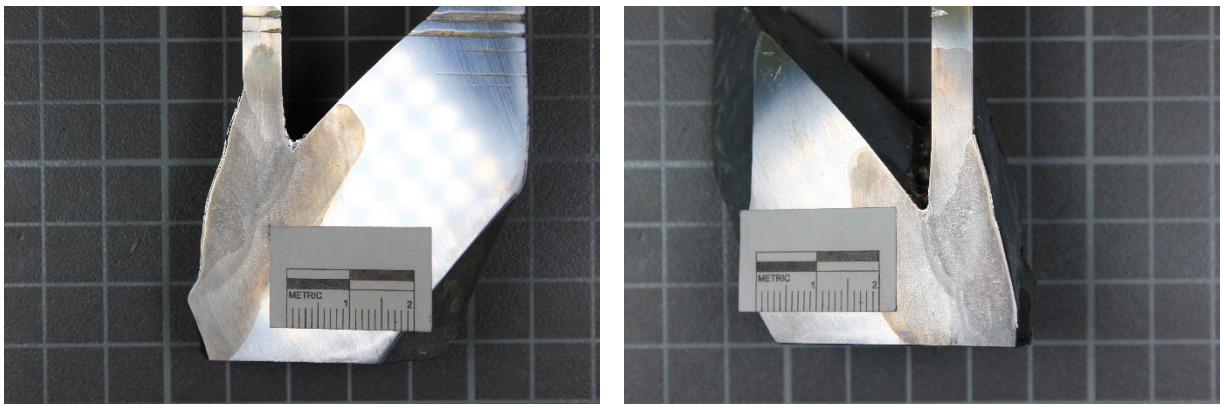

(a) (b)

Figure A.9: (a) Left Side of A-3-5, (b) Right Side of A-3-5

Figure A.10: Left Side of A-3-6

A.2 Pole B Crack Images

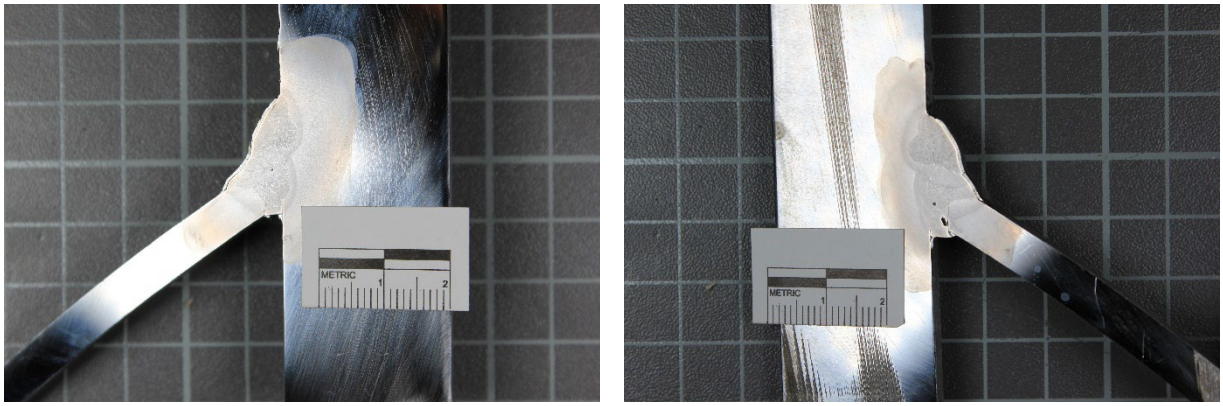

(a) (b)

Figure A.11: (a) Bottom Side of B-2-1, (b) Top Side of B-2-1

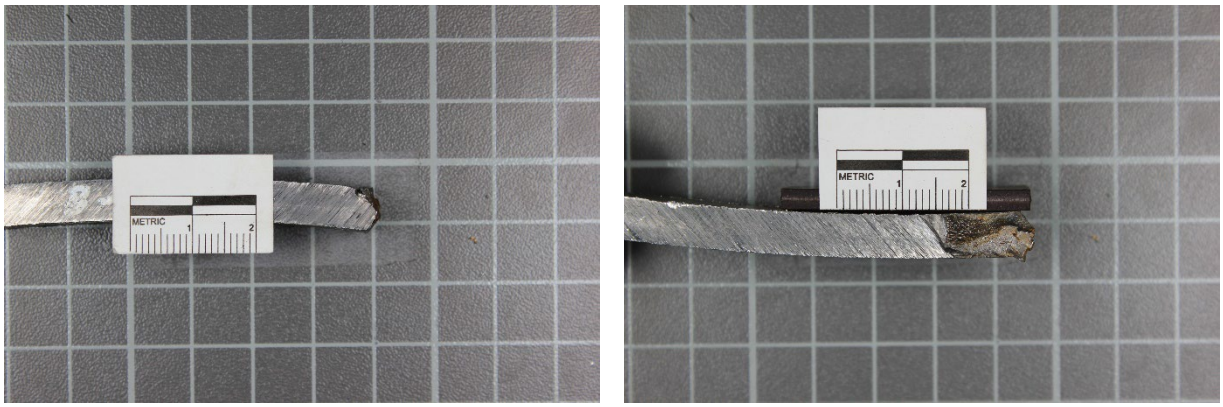

(a) (b)

Figure A.12: (a) Bottom Side of B-2-2, (b) Top Side of B-2-2

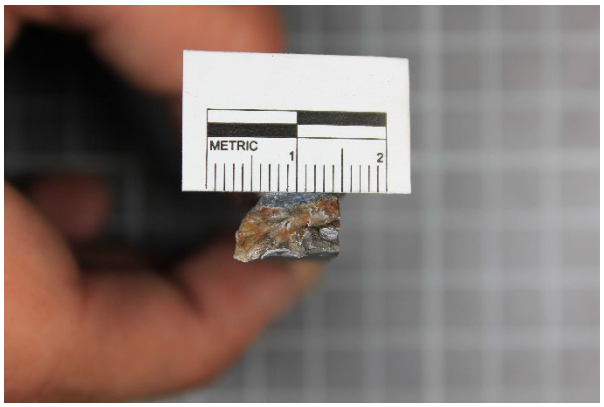

Figure A.13: End of B-2-2

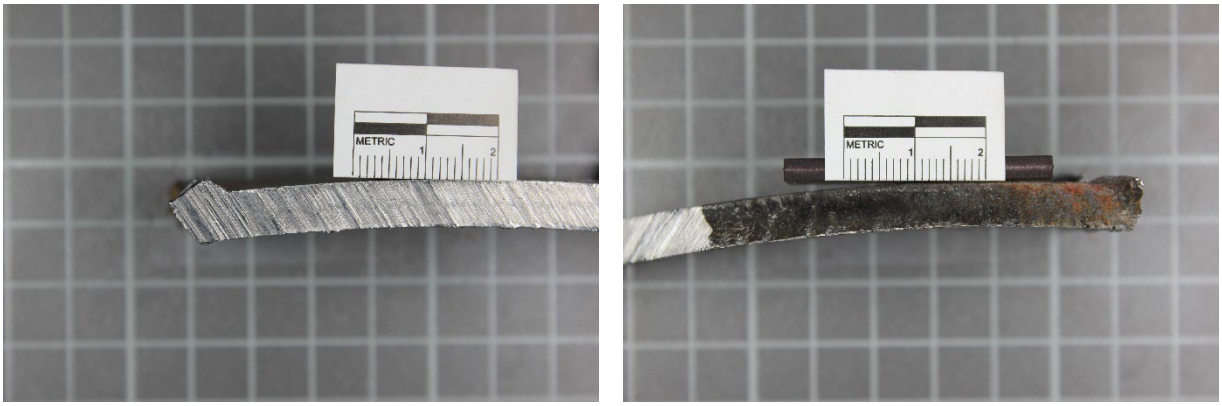

(a) (b)

Figure A.14: (a) Bottom Side of B-2-3, (b) Top Side of B-2-3

Figure A.15: End of B-2-3

Figure A.16: Reinforcing Rim B [1]

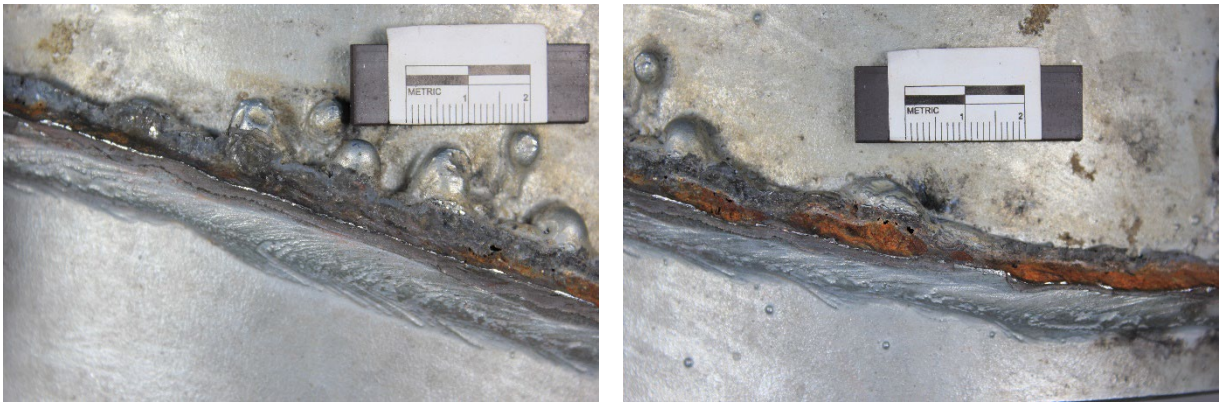

Figure A.17: (a) Reinforcing Rim B [2], (b) Reinforcing Rim B [3]

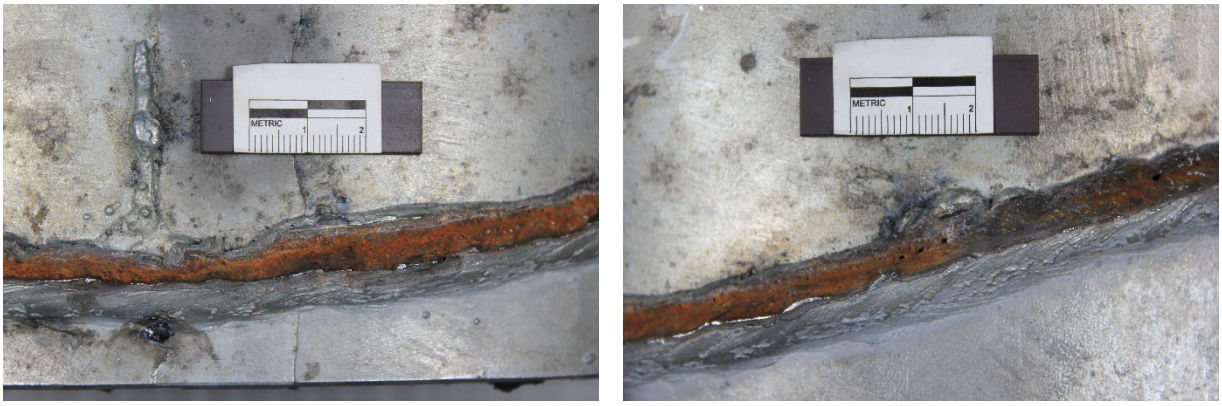

(a) **(b)**

Figure A.18: (a) Reinforcing Rim B [4], (b) Reinforcing Rim B [5]

(a) **(b)**

Figure A.19: (a) Reinforcing Rim B [6], (b), Reinforcing Rim B [7]

(a) (b)

Figure A.20: (a) Left Side of B-2 Crack, (b), Right Side of B-2 Crack

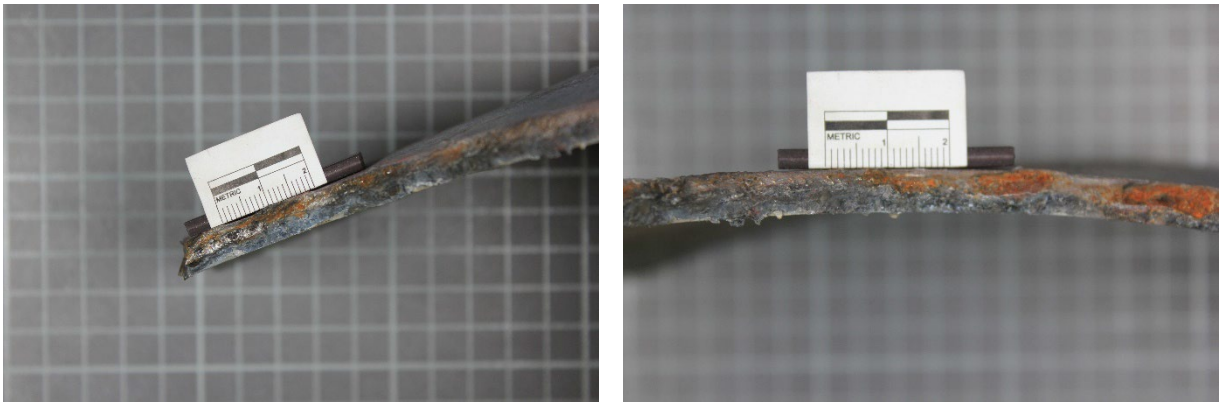

(a) (b)

Figure A.21: (a) Pole B Crack [1], (b) Pole B Crack [2]

(a) (b)

Figure A.22: (a) Pole B Crack [3], (b) Pole B Crack [4]

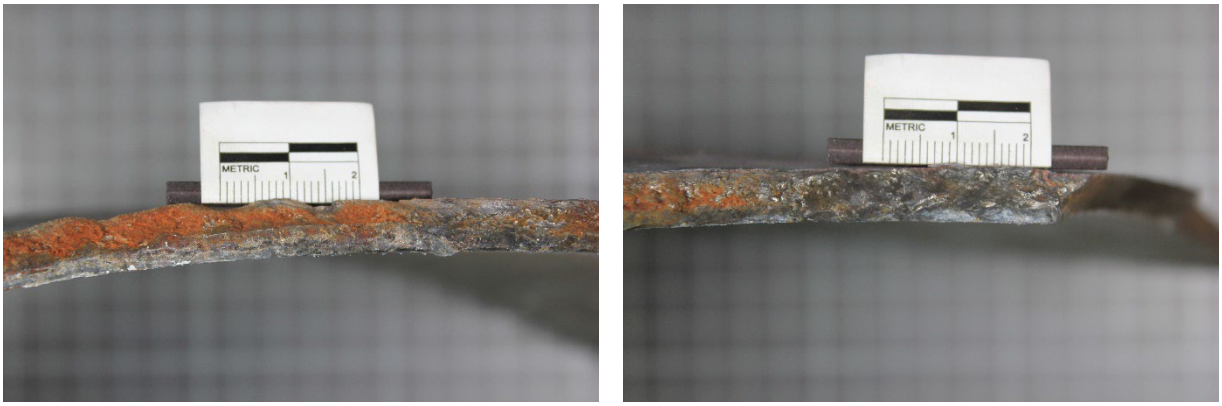

(a) (b)

Figure A.23: (a) Pole B Crack [5], (b) Pole B Crack [6]

A.3 Pole C Crack Images

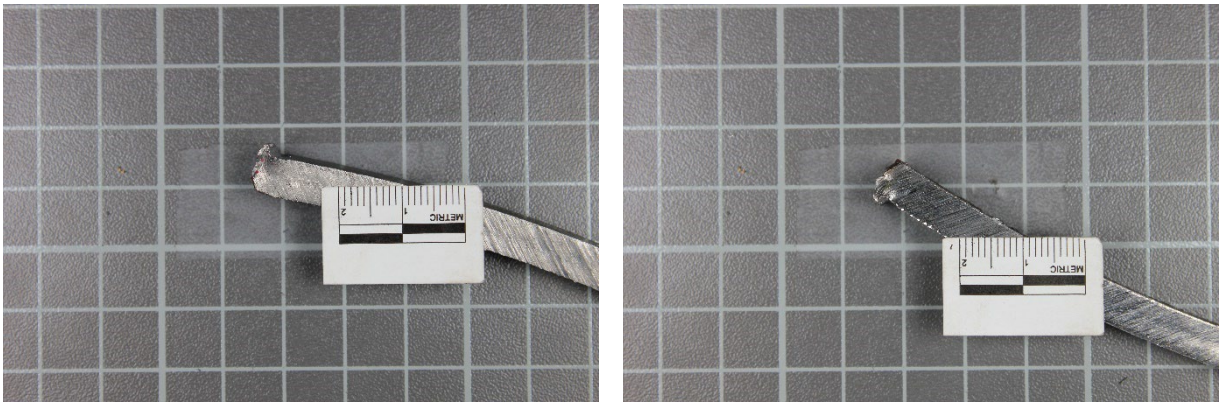

(a) (b)

Figure A.24: (a) Bottom Side of C-2-1, (b) Top Side of C-2-1

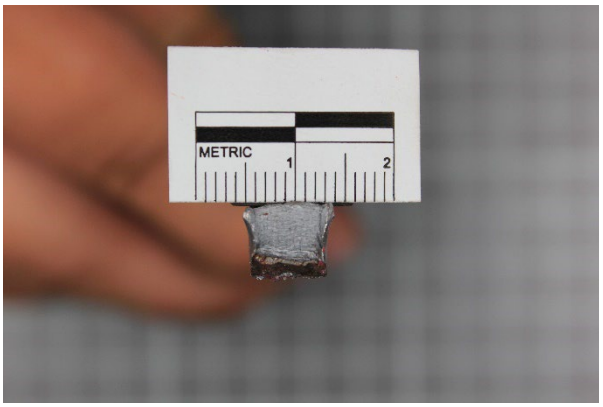

Figure A.25: End of C-2-1

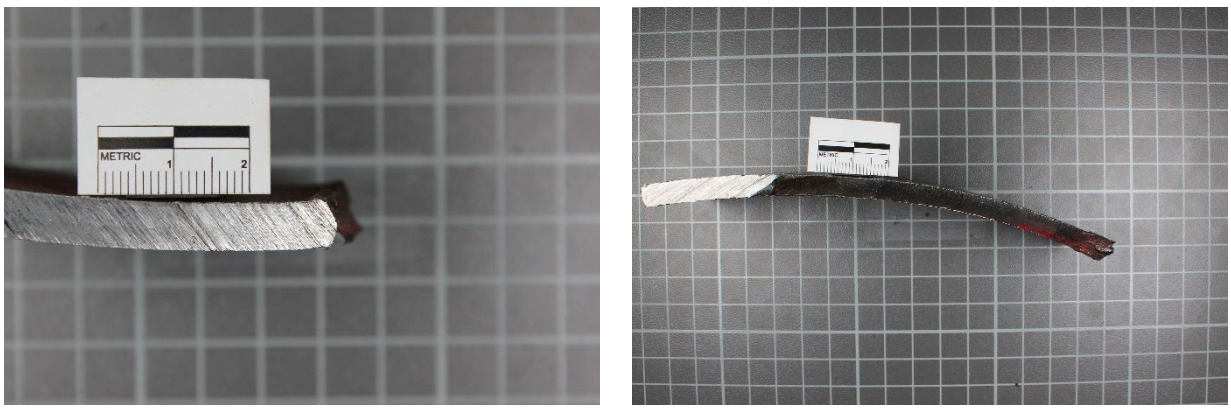

(a) (b)

Figure A.26: (a) Bottom Side of C-2-2, (b) Top Side of C-2-2

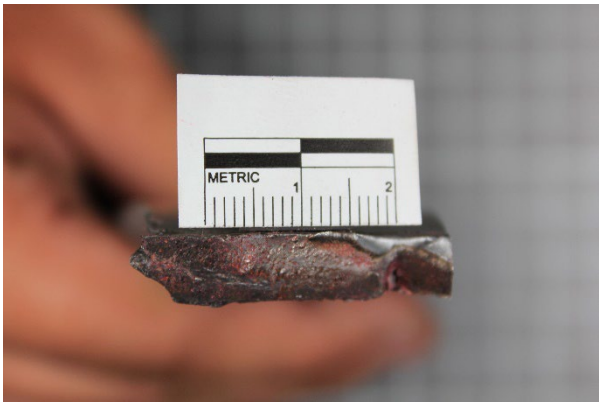

Figure A.27: End of C-2-2

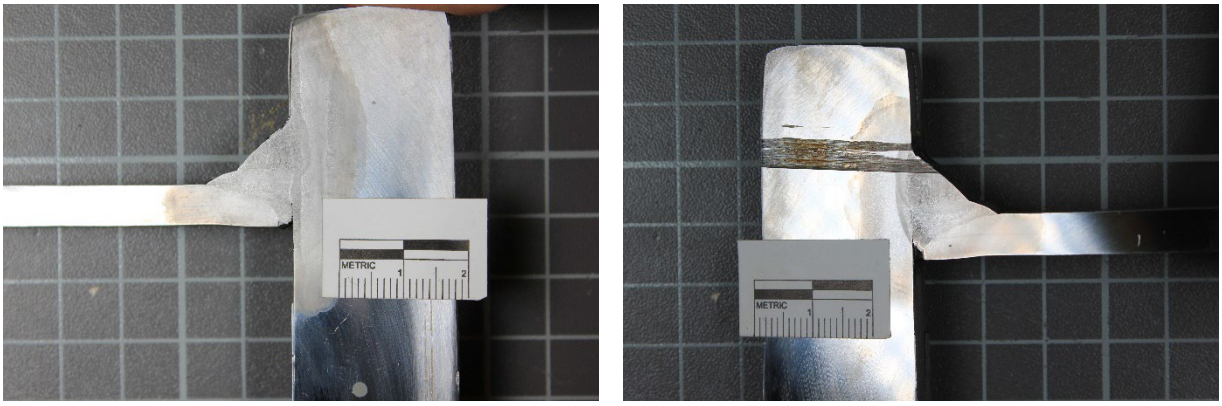

(a) **(b)**

Figure A.28: (a) Left Side of C-2-3, (b) Right Side of C-2-3

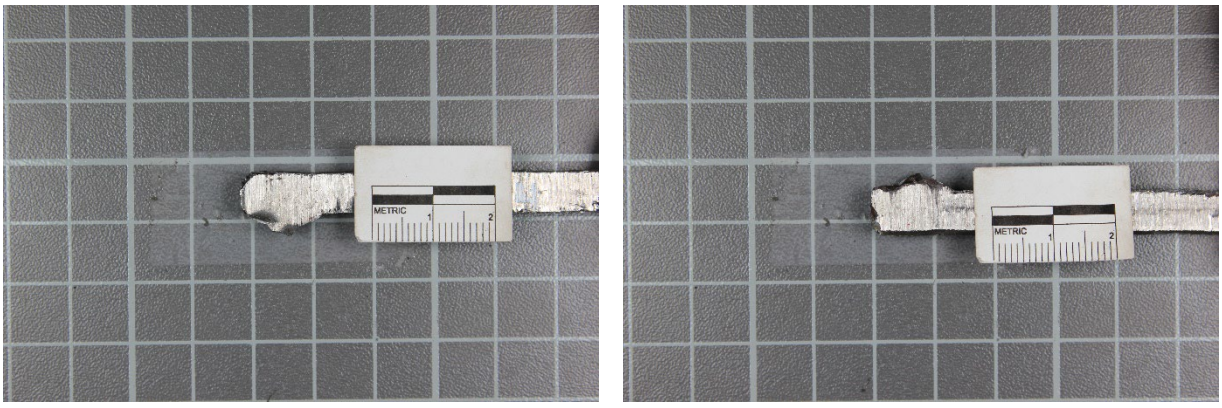

(a) **(b)**

Figure A.29: (a) Left Side of C-2-4, (b) Right Side of C-2-4

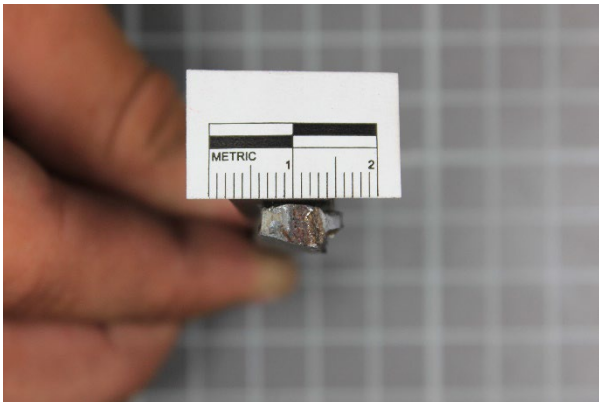

Figure A.30: End of C-2-4

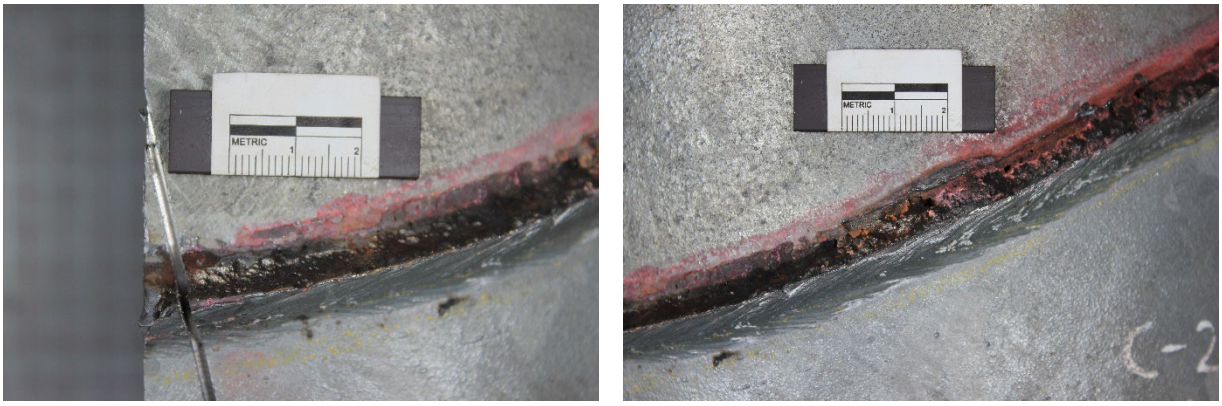

(a) **(b)**

Figure A.31: (a) Reinforcing Rim C [1], (b) Reinforcing Rim C [2]

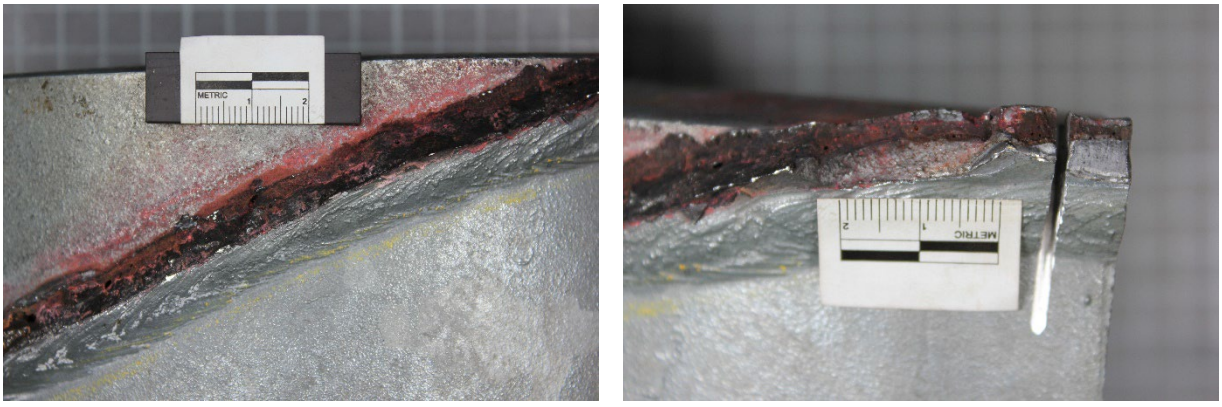

(a) **(b)**

Figure A.32: (a) Reinforcing Rim C [3], (b) Reinforcing Rim C [4]

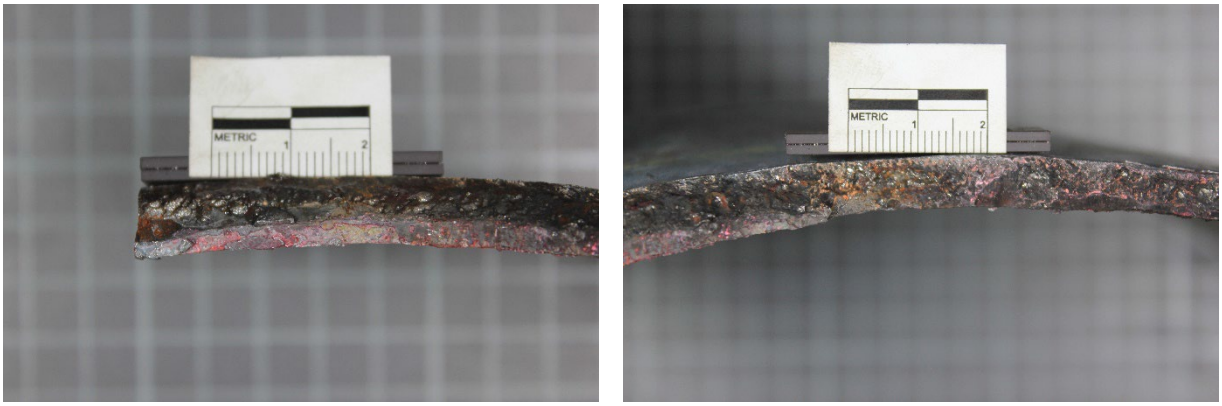

(a) (b)

Figure A.33: (a) Pole C Crack [1], (b) Pole C Crack [2]

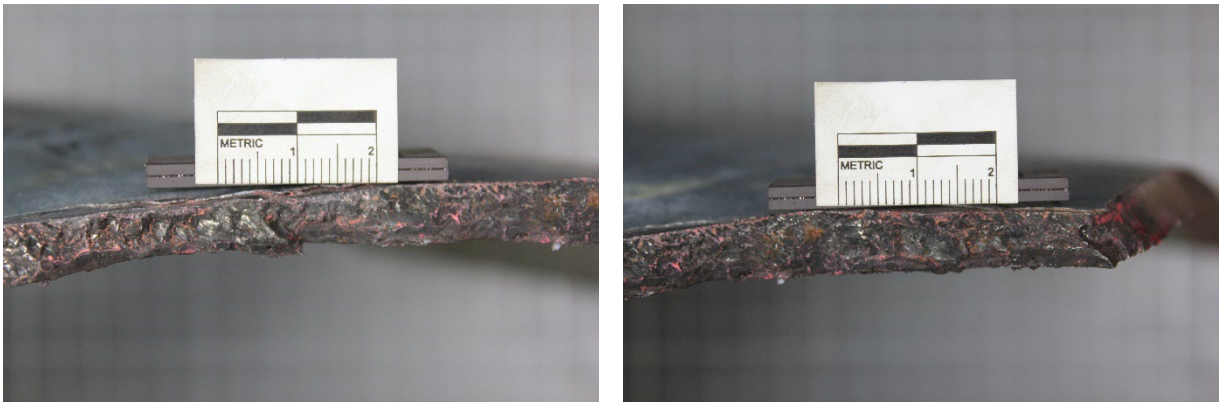

(a) (b)

Figure A.34: (a) Pole C Crack [3], (b) Pole C Crack [4]

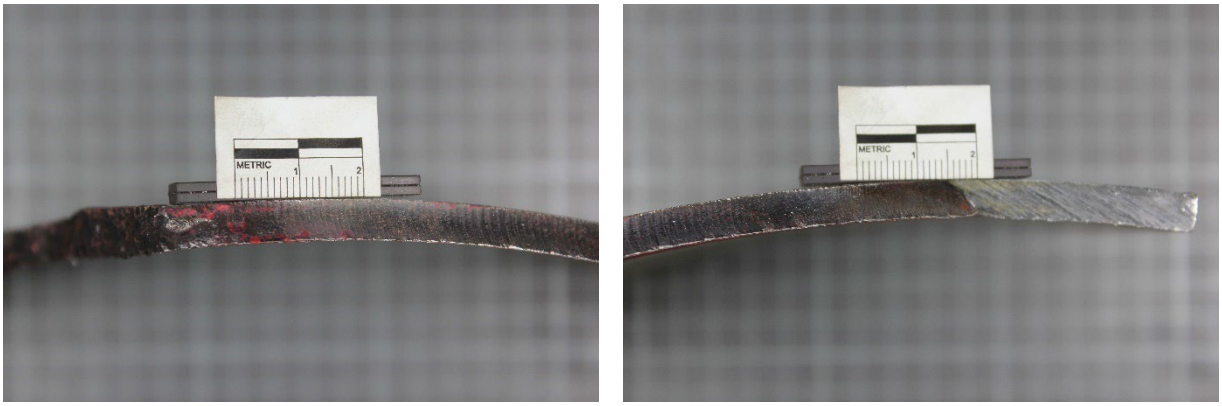

(a) (b)

Figure A.35: (a) Bottom Side of C-2 Crack [1], (b) Bottom Side of C-2 Crack [2]

A.4 Pole D Crack Images

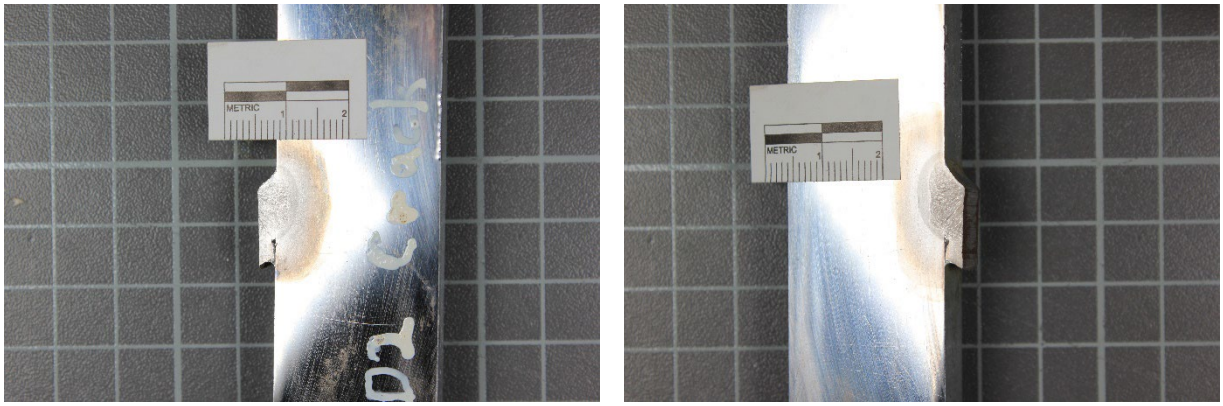

(a) (b)

Figure A.36: (a) Top Side of D-2 Crack, (b) Bottom Side of D-2 Crack

AD ASTRA PER ASPERA

Kansas

Department of Transportation